# Advanced Radiocarbon Analysis of Environmental Samples at the 6 MV AMS System of CologneAMS

**Inaugural-Dissertation**

zur

Erlangung des Doktorgrades

der Mathematisch-Naturwissenschaftlichen Fakultät

der Universität zu Köln

vorgelegt von

Martina Anna Gwozdz

April 2026

*Don't let anyone rob you of your imagination, your creativity, or your curiosity. It's your place in the world; it's your life. Go on and do all you can with it, and make it the life you want to live.*

**Dr. Mae Jemison**

Engineer, Physician and Former NASA Astronaut

# Abstract

Compared with conventional $^{14}$C AMS (Accelerator Mass Spectrometry), in which samples are converted into graphite with around 1000 $\mu$g C, direct $CO_2$ gas measurements enable the analysis of samples with less than 200 $\mu$g C. This becomes increasingly important for environmental and archaeological applications. At the 6 MV AMS system at the University of Cologne, the established EA-GIS-AMS setup and the newly developed COMORI (COmbustion and Measurement Of Radiocarbon and stable Isotopes) system are used for advanced small $^{14}CO_2$ analysis.

This thesis evaluates the performance of the COMORI setup and investigates the influence of $\delta^{13}$C corrections on conventional radiocarbon ages measuring 103 samples from three different IAEA standards. Replacing the $\delta^{13}$C value in the conventional radiocarbon age calculation with IRMS-derived values improves the average conventional radiocarbon ages of many samples, although the effect is limited by counting statistics in $CO_2$ AMS measurements. Reliable measurements are achieved for sample masses down to about 10 $\mu$g carbon, and a new cleaning routine improved the blank level from $^{14}C/^{12}C = 0.0127 \pm 0.0012$ to $0.00392 \pm 0.00215$. A constant contamination model yields $F^{14}C = 0.87 \pm 0.22$, consistent with the previous (EA-GIS) system value of $F^{14}C = 0.93 \pm 0.23$.

The first application of COMORI investigates the suitability of $CO_2$ AMS measurements for dendrochronologically dated tree rings and compares them with graphite measurements. Conventional radiocarbon age uncertainties range from 59–63 years for $CO_2$ measurements and 38–39 years for graphite targets due to improved counting statistics. After OxCal modelling, both approaches yield statistically robust calibrated ages.

Radiocarbon measurements were further applied to Late Glacial pine wood discovered at Schloss Neuhaus in Paderborn, Germany, to investigate the chronology of Allerød deposits. More than 80 pine trunks were grouped into seven dendrochronological sequences and dated using $CO_2$ and graphite AMS measurements. The modelled ages indicate that the trees span roughly 600 years from about 13 500 calBP to 13 040 calBP. Their spatial distribution and trunk orientations suggest deposition during multiple fluvial transport events, providing a rare radiocarbon archive of Late Glacial pine wood.

The second application addresses the measurement of activated graphite samples, in the context of nuclear waste management, where sample dilution prior to AMS analysis is required to avoid contamination of the system. Both mechanical dilution with dead graphite and gas dilution were investigated. Although mechanically diluted samples show lower measurement scatter ($\approx$3 %) than gas-diluted samples ($\geq$11 %), gas dilution offers a flexible and practical approach and proves suitable for the reliable measurement of activated graphite.

# Kurzzusammenfassung

Im Vergleich zur konventionellen $^{14}$C-AMS (Accelerator Mass Spectrometry), bei der Proben zu Graphit mit typischerweise etwa 1000 $\mu$g C präpariert werden, ermöglichen direkte $CO_2$-Gasmessungen die Analyse von Proben mit weniger als 200 $\mu$g C. Dies gewinnt insbesondere für umweltwissenschaftliche und archäologische Anwendungen zunehmend an Bedeutung. Am 6-MV-AMS-System der Universität zu Köln werden das etablierte EA-GIS-AMS-Setup sowie das neu entwickelte COMORI-System (COmbustion and Measurement Of Radiocarbon and stable Isotopes) für die fortgeschrittene $^{14}CO_2$ kleiner Proben eingesetzt.

Diese Dissertation evaluiert die Leistungsfähigkeit des COMORI-Setups und untersucht den Einfluss von $\delta^{13}$C-Korrekturen auf konventionelle Radiokohlenstoffalter anhand von 103 Messungen an drei verschiedenen IAEA-Standards. Der Ersatz des $\delta^{13}$C-Werts in der Berechnung des konventionellen Radiokohlenstoffalters durch mittels IRMS bestimmte Werte verbessert die mittleren konventionellen Radiokohlenstoffalter vieler Proben, wobei der Effekt bei $CO_2$-AMS-Messungen durch die Zählstatistik begrenzt ist. Zuverlässige Messungen werden für Probenmassen bis hinunter zu etwa 10 $\mu$g Kohlenstoff erreicht, und eine neue Reinigungsroutine verbesserte den Blankwert von $^{14}C/^{12}C = 0.0127 \pm 0.0012$ auf $0.00392 \pm 0.00215$. Ein Modell konstanter Kontamination ergibt $F^{14}C = 0.87 \pm 0.22$ und stimmt damit mit dem Wert des vorherigen Systems (EA-GIS) von $F^{14}C = 0.93 \pm 0.23$ überein.

Die erste Anwendung von COMORI untersucht die Eignung von $CO_2$-AMS-Messungen für dendrochronologisch datierte Baumringe und vergleicht diese mit Graphitmessungen. Die Unsicherheiten der konventionellen Radiokohlenstoffalter liegen aufgrund verbesserter Zählstatistik zwischen 59–63 Jahren für $CO_2$-Messungen und 38–39 Jahren für Graphit-Targets. Nach der Modellierung mit OxCal liefern beide Ansätze statistisch robuste kalibrierte Alter.

Radiokohlenstoffmessungen wurden außerdem auf spätglaziales Kiefernholz angewendet, das in Schloss Neuhaus in Paderborn, Deutschland, entdeckt wurde, um die Chronologie der Allerød-Ablagerungen zu untersuchen. Mehr als 80 Kiefernstämme wurden in sieben dendrochronologische Sequenzen gruppiert und mittels $CO_2$- und Graphit-AMS-Messungen datiert. Die modellierten Alter weisen darauf hin, dass die Bäume einen Zeitraum von ungefähr 600 Jahren zwischen etwa 13 500 calBP und 13 040 calBP abdecken. Ihre räumliche Verteilung und die Ausrichtung der Stämme deuten auf Ablagerungen während mehrerer fluviatiler Transportereignisse hin und liefern damit ein seltenes Radiokohlenstoffarchiv spätglazialen Kiefernholzes.

Die zweite Anwendung befasst sich mit der Messung aktivierter Graphitproben im Kontext der nuklearen Entsorgung, bei der vor der AMS-Analyse eine Verdünnung der Proben erforderlich ist, um eine Kontamination des Systems zu vermeiden. Untersucht wurden sowohl die mechanische Verdünnung mit totem Graphit als auch die Gasverdünnung. Obwohl mechanisch verdünnte Proben eine geringere Messstreuung (≈3 %) aufweisen als gasverdünnte Proben (≥11 %), bietet die Gasverdünnung einen flexiblen und praktischen Ansatz und erweist sich als geeignet für die zuverlässige Messung aktivierter Graphitproben.

# Contents

# Introduction

In general, Accelerator Mass Spectrometry (AMS) is a highly sensitive technique that has fundamentally advanced the detection of rare isotopes. Its development has been particularly important for radiocarbon analysis in scientific fields, where the extremely low natural abundance of $^{14}$C requires sensitive measurement. This thesis investigates the application of AMS to small ($<200\ \mu g$ C) $CO_2$ samples in order to accurately determine either the age of an organic sample or to determine the $^{14}$C activity of graphite.

The discovery of $^{14}$C dates back to 1933, when F. N. D. Kurie [1] observed long, thin tracks in a cloud chamber after nitrogen had been exposed to fast neutrons. In 1935 and 1936, W. Chadwick, W. E. Burcham, and M. Goldhaber [2] further investigated $^{14}$N and concluded that the nuclear reaction proceeds as

$$^{14}\mathrm{N} + \mathrm{n} \rightarrow {}^{14}\mathrm{C} + \mathrm{p}.$$

In 1940, M. D. Kamen and S. Ruben confirmed these findings experimentally by bombarding graphite with neutrons. The irradiated graphite was subsequently combusted to $CO_2$, precipitated as $CaCO_3$, and a reproducible radioactive activity attributable to $^{14}$C was measured [3].

At approximately the same time, foundational work by Korff et al. (1940) [4] and Libby et al. (1946) [5] established the atmospheric production mechanisms of $^{14}$C and provided early estimates of its production rate. Libby recognized that carbonaceous matter in the atmosphere and on the earth's surface should be in exchange equilibrium with atmospheric carbon and therefore should contain a measurable amount of $^{14}$C [5]. This insight laid the foundation for radiocarbon dating.

In the following decade, Libby developed the radiocarbon dating method, for which he was awarded the Nobel Prize in Chemistry in 1960. By counting the $\beta$-decays of carbon samples, he determined a half-life of 5 720 ± 47 years for $^{14}$C [6], which was later revised to 5 568 ± 30 years [7]. This value became known as the Libby half-life and is still used in the calculation of conventional radiocarbon ages. Although the currently accepted physical half-life of $^{14}$C is 5 730 ± 40 years (Cambridge half-life), the Libby value remains in use to ensure consistency and comparability between radiocarbon measurements obtained over different decades [8]. By measuring samples of independently known age, Libby confirmed the methodological basis of radiocarbon dating.

During the 1970s, however, the limitations of radiometric decay counting became increasingly evident. Libby measured the direct detection of radioactive decay events from samples of known mass. Because decay counting relies on radioactive decay statistics, it becomes increasingly inefficient for isotopes with low natural abundances or long half-lives. As a consequence, relatively large sample masses of several grams were required in order to obtain sufficient counting statistics, which restricted the analysis of valuable, rare, or small samples [9].

A major breakthrough was achieved with the development of AMS, which enabled the direct measurement of isotopic ratios instead of radioactive decay. One of the first, radiocarbon AMS measurements were carried out, among others, at the Nuclear Structure Research Laboratory in Rochester, where sample masses between 3.5 and 15 mg were analyzed [10]. This represented a substantial reduction compared with the several grams of carbon required for $\beta$-decay counting in Libby's original method [9].

For AMS, the sample is converted into negative ions and injected into an accelerator. The use of negative ions suppresses some interfering species, while subsequent stripping destroys molecular ions and converts the beam into positive ions. The rare radionuclides are then identified by a sequence of magnetic and electrostatic analyzers alongside with detectors, which filters them on the basis of their momentum, energy, and nuclear charge. In this way, AMS allows direct measurement of isotopic ratios between the rare and stable isotopes at abundances as low as $10^{-16}$.

Although early AMS systems focused primarily for radiocarbon dating in archaeology, continued advances in sample preparation, ion sources, accelerator technology, and detector systems progressively reduced the required sample size from the milligram to the microgram scale. This development greatly broadened the scope of AMS, which is now widely used not only in archaeology but also in environmental science, nuclear physics, geology, and other related fields [11, 12, 13].

A representative example of this technological development is the 6 MV AMS system at the CologneAMS facility. The accelerator, developed by High Voltage Engineering (HVE) Europa B.V., was initially equipped with one ion source for the measurement of solid samples. For radiocarbon measurements, these solid samples are typically prepared as graphite. In 2015, a second HVE SO-110 ion source for direct gaseous $CO_2$ measurements was installed. This upgrade enabled the analysis of microgram-sized $CO_2$ samples without the need for prior graphitization, thereby facilitating the measurement of organic samples containing less than 200 $\mu$g C [14].

In contrast to graphite, $CO_2$ samples must be oxidized shortly before measurement and then transferred directly into the AMS system. For this purpose, a $CO_2$ Gas Injection System (GIS), previously established mainly for MICADAS systems [15], was implemented. This setup enabled automated operation and direct coupling to an Elemental Analyzer (EA), where solid samples can be combusted to $CO_2$ and transferred with the GIS to the AMS for measurement.

In 2021, the setup was further upgraded by the installation of a new EA and an additional Isotope Ratio Mass Spectrometer (IRMS) [16]. This development made it possible to measure stable and radioactive carbon isotopes quasi-simultaneously from the same sample. The resulting system is now referred to as COMORI (COmbustion and Measurement Of Radiocarbon and stable Isotopes).

The direct measurement of $CO_2$ from microgram-scale samples considerably broadens the possible applications of AMS, as it enables the investigation of materials that are too small, too valuable, or too limited for conventional graphite preparation. Demonstrating this potential and its implications is a central aim of this thesis, which is therefore structured in three successive steps.

First, the methodological basis of small $CO_2$ samples in AMS is established by introducing the experimental setup and by evaluating the performance of the COMORI system, with particular focus on fractionation correction, blank levels, and sample-size effects.

Second, the applicability of this approach is investigated for tree-ring material, including both a proof-of-concept study on dendrochronologically dated oak and a measurement of Late Glacial pine trunks from Schloss Neuhaus in Paderborn.

Third, the method is extended to activated nuclear reactor graphite in the context of nuclear waste management, where direct $CO_2$ measurement and gas dilution are explored to determine the activation of the material.

# Chapter 1

# Accelerator Mass Spectrometry

Accelerator Mass Spectrometry (AMS) is a key method for radiocarbon analysis of samples containing only small amounts of carbon. In this thesis, small samples are defined as samples with less than 200 $\mu$g C. The ability to analyze such samples is essential when only limited material is available. A central aim of this work is therefore to achieve reliable and accurate radiocarbon measurements for these sample sizes.

For AMS analysis, the samples are first converted to $CO_2$ by combustion. The resulting gas is then introduced into the AMS, where the $^{14}C/^{12}C$ ratio of the sample is measured. In addition, the stable carbon isotopes $^{12}C$ and $^{13}C$ are detected for normalization and isotopic correction. The following section outlines the operating principles of AMS.

## 1.1 Working principle of AMS

AMS enables the highly sensitive detection of rare radionuclides while simultaneously separating them from their isobars. The 6 MV AMS system at CologneAMS comprises several interconnected components that allow the measurement of $CO_2$. In the following, the individual stages of the measurement process are described, including ion formation in the ion source, low-energy mass analysis, acceleration and stripping, and final detection. A simplified schematic of an AMS system is shown in Fig. 1.1.

### 1.1.1 Ion source and low energy mass spectrometer

The SO-110 B ion source at the 6 MV accelerator is a cesium sputter ion source designed for $CO_2$ measurements. In general, the produced $CO_2$ is then transferred via the GIS to the ion source, where negatively charged ions are produced. These ions are extracted from the ion source and accelerated by an applied voltage of 35 kV. A schematic setup of this ion source can be seen in Fig. 1.2.

The fundamental operating principle of a cesium sputter ion source is based on the bombardment of a cathode by energetic cesium ions. Depending on the measurement type, the cathode contains either pressed graphite, in the case of graphitized samples, or a titanium inlet for $CO_2$ measurements. Figure 1.2 shows the cathode used for $CO_2$ measurements on the left-hand side. In $CO_2$ measurements, the gas

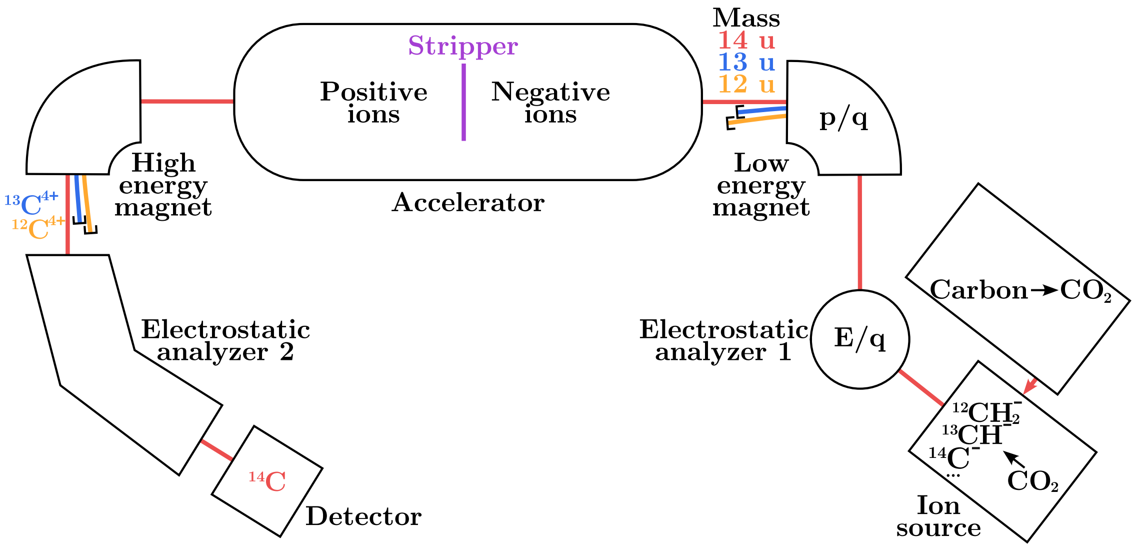

Figure 1.1: Simplified schematic of an AMS setup. Starting at the ion source, negative ions are produced from $CO_2$. A mass spectrometer separates the ions into masses 12 u, 13 u and 14 u and accelerates them towards the positively charged accelerator. Electrons are stripped from the ions and produce positively charged ions. $^{12}C$ and $^{13}C$ are measured after a second magnet while $^{14}C$ is measured at a detector after the second electrostatic analyzer.

is absorbed by the titanium inlet and reacts to form TiC and $TiO_2$, enabling the carbon to be ionized from the titanium surface [17]. Cesium bombardment then induces the sputtering of surface atoms and the formation of negative ions, which are subsequently extracted into the accelerator beamline [18].

The cesium sputter ion source consists of a cesium reservoir, an ionizer, and an extraction anode. A target with a titanium inlet, which is screwed onto a target holder, is inserted into the ion source. $CO_2$ flows over the titanium inlet and into the ion source. To enable ionization of the sample, cesium is first vaporized by heating the cesium reservoir to 110–140°C. The cesium vapor is then ionized at the ionizer, which is heated to approximately 1300°C, producing $Cs^+$ ions. Owing to the electric field between the target and the ionizer, the $Cs^+$ ions are accelerated towards the target. Their impact induces sputtering of surface atoms and molecules originating from the sample, which subsequently form negative ions.

Historically, negative ion formation in cesium sputter sources has been interpreted primarily in terms of surface ionization mechanisms. Sputtered neutral atoms interact with the cesium-covered sample surface or pass through the near-surface region, where the reduced work function facilitates electron transfer to atoms and molecules with sufficient electron affinity. If the electron affinity of the sputtered atom or molecule exceeds the local work function, electron capture becomes energetically favorable, resulting in the formation of a negative ion [19].

However, purely surface-based ionization models generally predict relatively low negative ion yields and cannot fully account for the high ionization efficiencies observed experimentally in AMS cesium sputter sources. This discrepancy has led to the development of more comprehensive descriptions that include plasma-assisted ionization processes in the sputtering region above the sample surface. Under in-

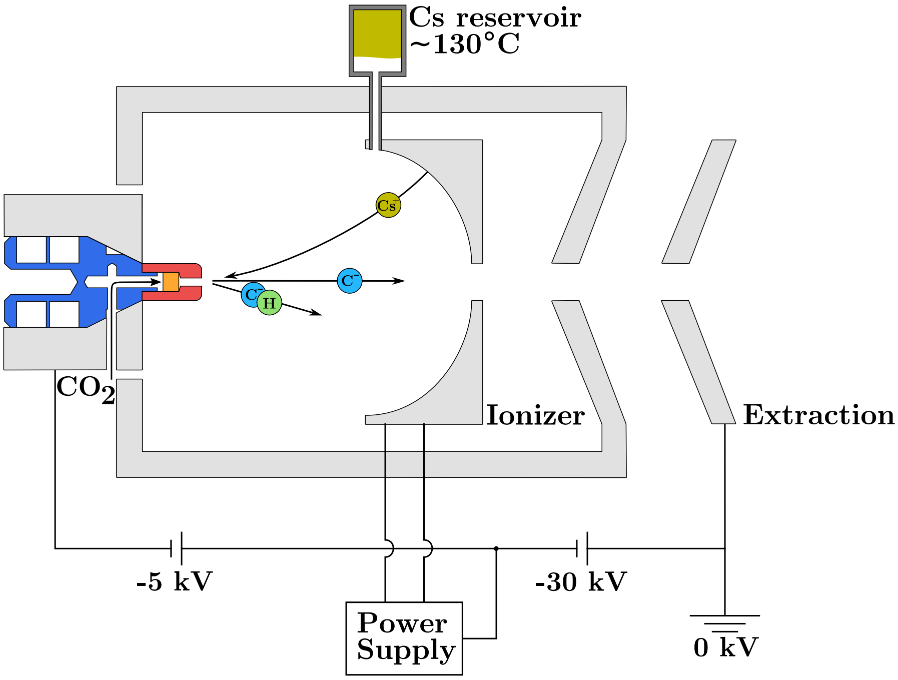

Figure 1.2: Schematic of the SO-110 B cesium sputter ion source at the Cologne 6 MV AMS system. The target holder (blue) carries a target (red) screwed onto its top, into which a titanium inlet (orange) is pressed. The assembled holder can then be inserted into the ion source for a $CO_2$ measurement.

tense $Cs^+$ bombardment, a dense cloud of cesium vapor, sputtered neutrals, secondary electrons, and excited atoms forms in the immediate vicinity of the cathode, often referred to as a sputter plasma. Within this environment, secondary electrons excite neutral cesium atoms. Approximately 71 % of $C^-$ originates from electron capture from the 5d state, while 24 % originates from the 6p state. The only visible emission lines correspond to transitions from 7p to 6s and from 8p to 6s, producing the characteristic blue glow observed in the ion source [20, 21].

The atoms and molecules extracted from the ion source are then separated according to their energy-to-charge ratio (E/q) by the electrostatic analyzer 1 (ESA), and on their momentum to charge ratio (p/q) by the low energy magnet. After these steps, only ions with masses 12 u, 13 u, and 14 u remain for carbon measurements. To allow sequential measurement of all three carbon isotopes, a bouncer system is used. Here, the vacuum chamber of the low-energy magnet is electrically isolated so that an additional electric potential can be applied. By varying this potential, the momentum of the ions is shifted accordingly, enabling the successive injection of the different isotopes into the accelerator. This allows the different carbon isotopes to be injected successively and measured quasi-simultaneously.

### 1.1.2 Acceleration and Stripping

In AMS, the accelerator is the central component that enables the subsequent separation of rare radionuclides from stable isobars and the destruction of molecular interferences. The accelerator operates as an electrostatic tandem system, in which ions are accelerated twice through the same accelerating potential.

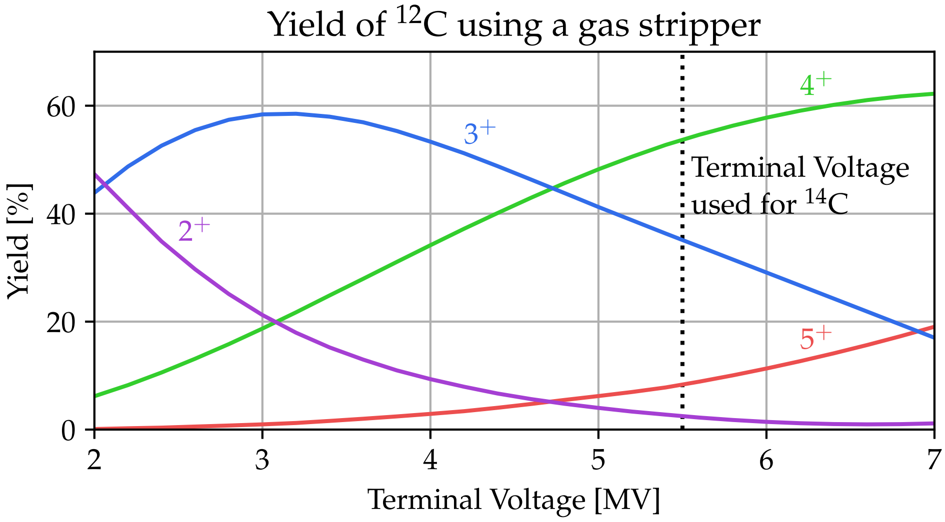

Figure 1.3: The yield of different charge states of $^{12}$C with a gas stripper, computed using the semi-empirical approach of Sayer [22]. The black dotted line indicates the 5.5 MV used for $^{14}$C measurements at the 6 MV AMS system at CologneAMS. The yield curves for $^{13}$C and $^{14}$C are very similar. With increasing isotope mass, the maxima of the yield curves shift slightly toward higher terminal voltages.

For the measurement of $^{14}$C, the molecular ions extracted from the ion source must first be dissociated. For mass 14 u, these include molecules such as $^{12}CH_2$ or $^{13}CH$.

The negatively charged ions from the ion source are accelerated toward the positively charged terminal, which lies inside the accelerator and is charged to 5.5 MV. Inside the terminal, the ions pass through a stripper filled with argon gas, where collisions remove the electrons responsible for the molecular bond. This process breaks up molecular ions and converts the resulting atoms into positively charged ions.

After stripping, the now positively charged ions are accelerated a second time as they travel away from the terminal back toward ground potential. The total kinetic energy of the ions exiting the accelerator is therefore determined by the terminal voltage and the final charge state selected after stripping. For an ion with charge state q, the final energy E is given by

$$E = (|q| + 1) \cdot e \cdot V_T + E_{inj}, \tag{1.1}$$

where $V_T$ is the terminal voltage, e is the elementary charge and $E_{inj}$ the injection energy.

The yield of the isotopes of interest varies depending on the terminal voltage and the resulting charge state. Figure 1.3 shows the theoretical yields of different charge states, which depend on the atomic number, mass, and kinetic energy of the ions, but may differ from measured yields, as shown in [23]. At the 6 MV AMS system in Cologne, the optimal yield is achieved for a momentum-to-charge ratio corresponding to $^{12}$C, $^{13}$C, and $^{14}$C in the $4^+$ charge state with a terminal voltage of 5.5 MV.

After transmission through the high-energy magnet of the accelerator system, the stable carbon isotopes $^{12}$C and $^{13}$C are present in sufficient abundance to be measured as ion currents in offset Faraday cups. The $^{13}$C/$^{12}$C ratio is obtained from these measured ion currents.

In contrast to the stable isotopes, $^{14}$C is far less abundant and therefore has to be counted individually with a detector. After the accelerator, the ions are analyzed by an achromatic high-energy mass spectrometer composed of the high-energy magnet and the high-energy ESA. By selecting an appropriate distance between these two elements, the system becomes insensitive to energy fluctuations within a certain range [24].

### 1.1.3 Detection

After acceleration and charge state selection, the rare radionuclides enter the gas ionization detector through a silicon nitride window. A picture of the detector is shown in Fig. 1.4 i). The detector counts incoming particles and is filled with approximately 40 mbar of isobutane, in which the incoming ions lose energy predominantly through ionization of the gas molecules along their trajectories. The energy loss in the gas is characteristic for each ion species and depends on the atomic number, as described by the Bethe–Bloch formula [25].

As an ion traverses the detector volume, it produces electron–ion pairs, that in turn generate an ionization cascade which is collected by an applied electric field and converted into electrical signals. The anode of the gas ionization detector is segmented along the beam direction, enabling the measurement of the energy loss in successive regions of the detector. Ions with identical mass and kinetic energy

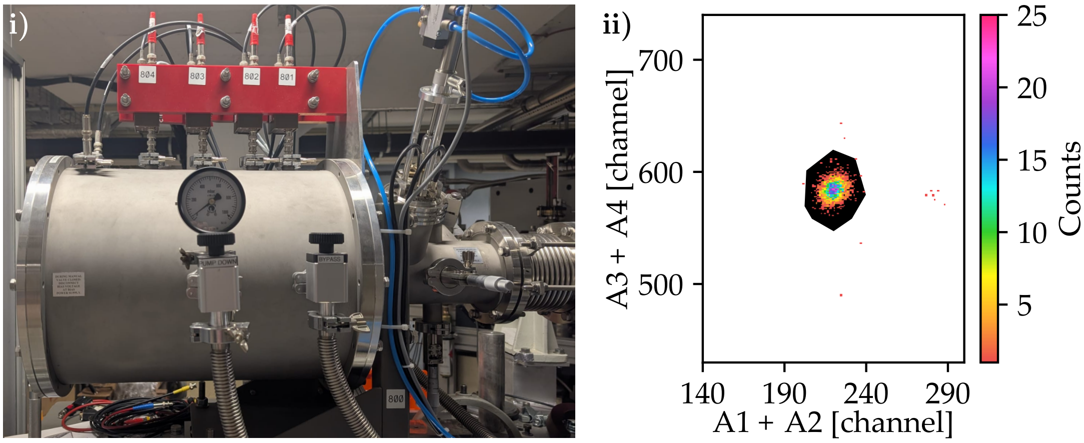

Figure 1.4: i) Gas ionization detector used for $^{14}$C measurements. The four anode connections are visible at the top of the cylindrical detector in red. The ion beam enters the detector from the beamline on the right-hand side. ii) Example of a $^{14}$C spectrum measured for a standard material with a short acquisition time, resulting in low count statistics. The black polygon indicates the ROI used for the identification and counting of $^{14}$C events, from which the $^{14}$C/$^{12}$C value is determined. In measurements of other radionuclides, additional isobaric interferences may occur close to the ROI; the ROI is therefore defined to isolate the events of interest and exclude interfering signals.

but different atomic number exhibit different stopping powers in the detector gas, resulting in characteristic energy-loss patterns.

This principle is used for isobar discrimination in AMS. In radiocarbon measurements, the stable isobar $^{14}$N is already effectively suppressed in the ion source because it does not form stable negative ions. Other interfering species, however, may still reach the detector; in $^{14}$C measurements, for example, Li$^{2+}$ can occur because it has the same mass-to-charge ratio as $^{14}$C. For heavier radionuclides, AMS can be affected by stable isobars that are not suppressed at the ion-source stage, such as $^{36}$S in measurements of $^{36}$Cl. Owing to the segmented anode structure of the gas ionization detector, such ions can be distinguished from the radionuclide of interest by their characteristic energy-loss signatures.

A representative example of the detector spectrum is shown in Fig. 1.4 ii). The black polygon marks the Region Of Interest (ROI) used for $^{14}$C counting. The x-axis shows the summed signals from anodes A1 and A2, while the y-axis shows the summed signals from anodes A3 and A4. Depending on how far the ion travels in the detector gas, the deposited energy is distributed differently among the anode segments, and the corresponding anode-pair signals are summed accordingly. As shown in Fig. 1.4 ii), the selected $^{14}$C region is free of interferences.

The $^{14}$C counted in the detector is then divided by the $^{12}$C measured after the high energy magnet to determine the $^{14}$C/$^{12}$C ratio.

# Chapter 2

# Small $CO_2$ samples with AMS

Many environmental samples for which the age is determined contain only a limited amount of carbon. For these ultra-small samples ($<$200 $\mu$g C), chemical preparation from sample material to graphite (graphitization) is often not feasible because it typically requires at least 3 mg of sample material. In such cases, oxidation to $CO_2$ enables radiocarbon analysis of valuable or limited samples.

For the interpretation of radiocarbon AMS measurements, it is essential to understand both the production of $^{14}C$ in the atmosphere and its distribution within the environment. Through the *carbon cycle*, $^{14}C$ is incorporated into organic matter, providing the basis for the age determination of organic materials. This is particularly relevant for the analysis of small samples, where precise AMS measurements enable reliable dating despite the limited amount of available carbon. The following sections therefore discuss radiocarbon production and its distribution in the environment, followed by the fundamental calculations of radiocarbon dating with AMS.

## 2.1 Radiocarbon production and its distribution in the environment

$^{14}C$ is produced predominantly in the earth's upper atmosphere [4]. Primary cosmic rays, which consist mainly of protons, alpha particles, and heavier ions, interact with atmospheric nuclei and generate cascades of secondary particles [26]. Among these, secondary neutrons are formed through spallation reactions involving light atmospheric nuclei, primarily nitrogen and oxygen [4]. The dominant production pathway of atmospheric $^{14}C$ is the reaction of these secondary neutrons with nitrogen [27]:

$$^{14}\mathrm{N} + \mathrm{n} \rightarrow {}^{14}\mathrm{C} + \mathrm{p}. \tag{2.1}$$

The produced $^{14}C$ atoms oxidize to $^{14}CO$ and are subsequently converted to $^{14}CO_2$ through reactions with atmospheric oxygen and hydroxyl radicals (OH) [28, 29].

Almost all naturally occurring $^{14}C$ originates from such atmospheric interactions of cosmic rays [30]. During the Holocene[1], the global average production rate is estimated to lie between 1.6 and 2.5 atoms/cm$^2$/s, depending on the model assumptions [27].

---

[1] The Holocene is the current geological epoch, beginning approximately 11 600 years ago [31].

Once formed, $^{14}CO_2$ enters the global carbon cycle. Atmospheric circulation leads to large-scale mixing in the atmosphere, resulting in an approximately homogeneous distribution on sufficiently long timescales. Radiocarbon is continuously exchanged between the atmosphere and other carbon reservoirs, including the oceans, soils, and biomass. Because these reservoirs interact with the atmosphere on different timescales, their $^{14}C$ concentrations may differ from that of the atmosphere. As a consequence, the differences in the $^{14}C$ concentration of reservoirs can affect radiocarbon dating of materials of different origin. This effect must be taken into account when determining ages and is discussed further in the next chapter.

In general, however, the approximately homogeneous distribution between atmosphere and biomass, alongside with the near-equilibrium between $^{14}C$ production and $\beta$-decay over long timescales, leads to an approximately constant atmospheric $^{14}R = {}^{14}C/{}^{12}C$, which forms the basis of radiocarbon dating of organic material.

## 2.2 Radiocarbon dating

Atmospheric $^{14}CO_2$ enters the global carbon cycle and is incorporated into living organisms primarily through photosynthetic carbon fixation in plants and subsequent transfer through the food web [32]. As a result of this continuous carbon exchange with the atmosphere, living organisms exhibit approximately the same $^{14}R_{atm}$ as atmospheric carbon. However, once the organism dies, this exchange ceases and the incorporated $^{14}C$ begins to decay according to

$$^{14}\mathrm{R} = {}^{14}\mathrm{R}_{atm} \cdot \exp\left(\frac{-\ln(2)}{\mathrm{T}_{1/2}} \cdot \mathrm{t}\right) \tag{2.2}$$

with $^{14}R_{atm}$ as the ratio right before the time of death and $T_{1/2}$ as the half-life of $^{14}C$.

To determine the time of death of an organism, Eq. 2.2 is rearranged to

$$\mathrm{t} = -\ln\left(\frac{^{14}\mathrm{R}}{^{14}\mathrm{R}_{atm}}\right) \cdot \frac{\mathrm{T}_{1/2}}{\ln(2)} \tag{2.3}$$

where the Cambridge half-life of $^{14}C$ with 5730 ± 40 years is used[2].

The determination of radiocarbon ages relies on several simplified assumptions: (i) a constant atmospheric $^{14}R$ ratio over time, (ii) no post-mortem alteration of the isotopic composition, and (iii) rapid and complete mixing between the carbon reservoirs. In reality, these assumptions are only approximately fulfilled.

For example, the exchange of carbon between reservoirs occurs on different timescales. Consequently, complete mixing is not achieved, and reservoirs such as the deep ocean mix much more slowly than others. These systematic offsets, known as reservoir effects, can show depleted $^{14}C$ values, in case of the oceanic carbon reservoirs, relative to the atmosphere. This and other carbon exchanges are part of the carbon cycle and are illustrated in Fig. 2.1.

Furthermore, variations in solar activity influence the cosmic-ray flux and thus the production rate of $^{14}C$, resulting in temporal fluctuations such as so-called Miyake events [33, 34]. In addition to these short-term fluctuations, long-term variations in atmospheric $^{14}C$ concentrations are also observed. For example, changes in the magnitude of the Earth's dipole moment, with a period of approximately 2 300 years (Hallstatt cycle), can modulate atmospheric $^{14}C$ production [35].

Alongside natural processes, anthropogenic influences also affect atmospheric $^{14}C$ concentrations. Two of the best-known examples are the Suess effect and the nuclear weapon testing. The Suess effect refers to the observed decrease in atmospheric $^{14}C$ concentrations since pre-industrial times. It is primarily caused by the combustion of fossil fuels such as coal and oil, which have been isolated from the atmosphere for millions of years and are therefore essentially free of $^{14}C$. The release of this $^{14}C$-depleted carbon into the atmosphere dilutes the atmospheric $^{14}R$ ratio and propagates through the global carbon cycle [36, 37].

---

[2] The original radiocarbon half-life determined by Libby et al. is 5568±30 years("Libby half-life" [7]). Later on measurements revised the physical half-life to 5730±40 years, but Libby's half-life is still used to keep historical consistency [8].

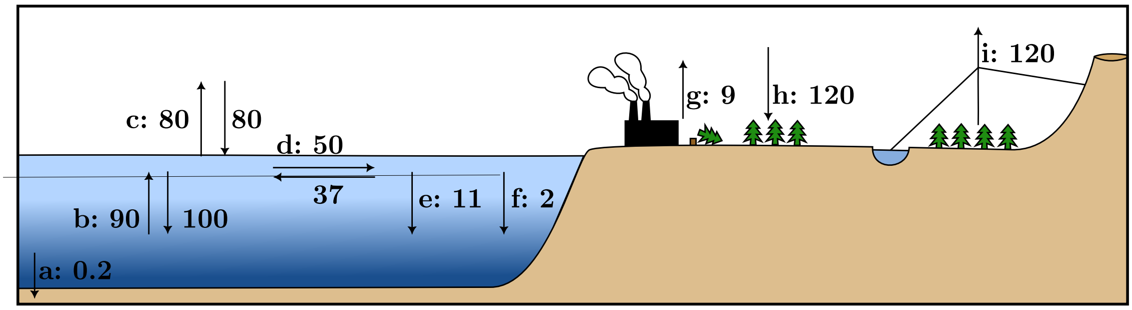

Figure 2.1: Schematic of a simplified global carbon cycle. The arrows represent carbon exchange fluxes in units of $10^{15}\,\mathrm{g\,C\,yr^{-1}}$. The labeled exchanges are between: a) intermediate ocean and ocean floor, b) intermediate ocean and surface ocean, c) surface ocean and atmosphere, d) surface ocean and marine biota, e) marine biota and intermediate ocean, f) marine biota and dissolved organic carbon, g) fossil fuels/land use and atmosphere, h) photosynthesis, and i) freshwater, respiration, volcanism, and atmosphere. The values are based on the more detailed description given in [40].

The second anthropogenic perturbation of atmospheric $^{14}C$ production occurs due to atmospheric nuclear weapons testing. As a result, atmospheric $^{14}C$ concentrations began to rise gradually in the late 1950s, followed by a sharp increase in the early 1960s [38, 39]. During atmospheric nuclear weapons testing, large numbers of neutrons were released, leading to an increased production of $^{14}C$ through their interaction with atmospheric nitrogen.

If these temporal variations are not taken into account, the calculated age corresponds to a *conventional radiocarbon age* rather than a true calendar age. Conversion to calendar years therefore requires calibration curves derived from independently dated materials.

Radiocarbon calibration curves are always region-specific, reflecting geographic differences in atmospheric and oceanic carbon reservoirs. This means that different calibration curves are required for specific time periods and geographic regions. For example, the rapid increase in atmospheric $^{14}C$ associated with mid-20th-century nuclear weapons testing (the "bomb peak") is described by the post-bomb calibration curve *Bomb 21 NH1* for the Northern Hemisphere[3]. In contrast, IntCal20 represents the Northern Hemisphere atmospheric $^{14}C$ variations prior to 1950 and is shown in Fig. 2.2. The timescale is expressed in calBP (calibrated years before present), where "present" is conventionally defined as the year 1950.

The IntCal20 is the current standard Northern Hemisphere calibration curve. It is based on absolutely dated tree-ring chronologies up to approximately 12 300 calBP [41], while wiggle-matched[4] tree-ring sequences extend the tree-ring-based portion of the curve to approximately 13 900–14 200 calBP [43]. Beyond this range,

---

[3] The calibration curves used in this thesis are obtained from the OxCal platform (https://c14.arch.ox.ac.uk/oxcal/OxCal.html), where the most recent versions of the radiocarbon calibration datasets are maintained and made publicly available.

[4] Wiggle matching is a method in which a series of radiocarbon dates with known spacing, such as tree rings, is aligned to the pattern of fluctuations in the calibration curve in order to determine the most likely calendar age of the sequence [42].

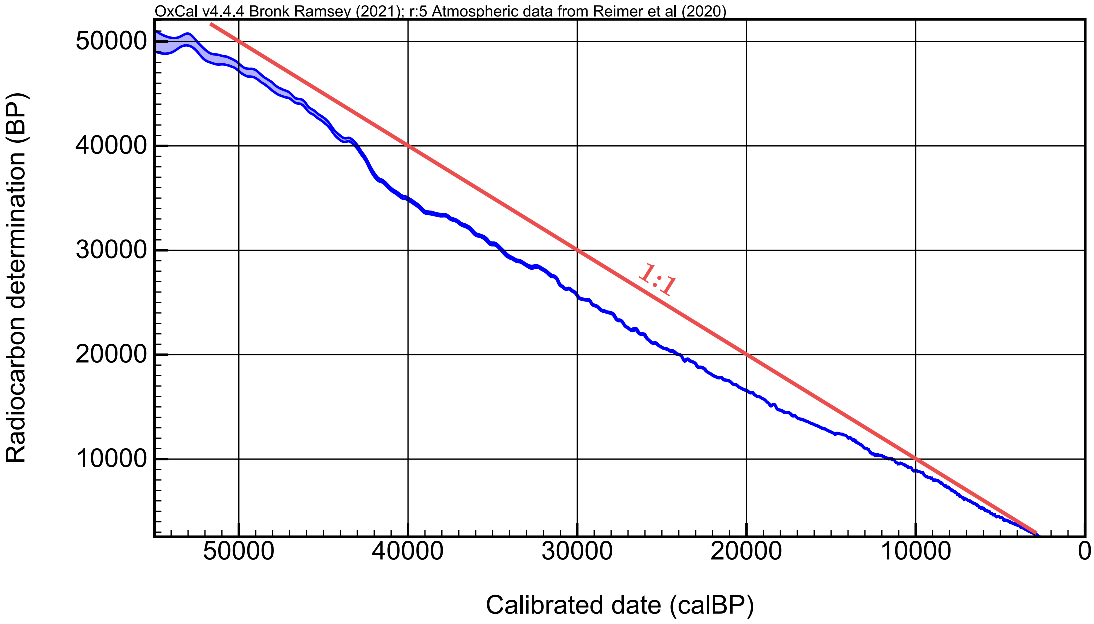

Figure 2.2: The IntCal20 Northern Hemisphere radiocarbon calibration curve is shown in blue for the interval 0–55 000 calBP. The red line represents a linear approximation relating measured radiocarbon age to calendar age. Radiocarbon determinations reflect the atmospheric $^{14}$C concentration at the time of death and therefore deviate from a linear age–calendar relationship due to natural and anthropogenic variations in atmospheric $^{14}$C. The calibration curve shown here is taken from OxCal v4.4.4 Bronk Ramsey (2021), r5 Atmospheric data from Reimer et al. (2020).

the curve is constructed from U–Th-dated speleothems, terrestrial macrofossils, corals, marine sediments, and wiggle-matched floating tree-ring records, extending the calibration curve to 55 000 calBP [44].

Having outlined the calibration curve basis, the next step is to consider how the radiocarbon content of a sample is quantified in AMS measurements. For this purpose, a normalized quantity, namely F$^{14}$C (Fraction modern), is used. In AMS, the $^{12}$C and $^{13}$C currents are measured and integrated to calculate the $^{13}\mathrm{R} = {}^{13}\mathrm{C}/{}^{12}\mathrm{C}$ , while the $^{14}$C counts and $^{12}$C ion current yield $^{14}$R. The calculations follow the conventions described in [45] and [46].

The F$^{14}$C is defined as

$$\mathrm{F}^{14}\mathrm{C} = \frac{^{14}\mathrm{R}_s}{^{14}\mathrm{R}_{std}} \tag{2.4}$$

where $^{14}\mathrm{R}_s$ is a corrected $^{14}$R ratio of the sample and $^{14}\mathrm{R}_{std}$ is the normalized reference standard.

To determine $^{14}\mathrm{R}_s$, several corrections must be applied to the measured AMS ratio. These corrections are described in detail in the following.

The first correction applied to the measured AMS ratios is the blank correction. In each AMS measurement sequence, standards and blank samples are measured alongside the unknown samples. Blank materials are radiocarbon-free and therefore represent the background level of the preparation and measurement system.

Any $^{14}$C signal detected in these blanks is attributed to contamination introduced during sample preparation or to instrumental background. To correct for this effect, the blank contribution is subtracted from the measured sample ratio. The blank-corrected ratio is defined as

$$^{14}\mathrm{R}_s = {}^{14}\mathrm{R}_m - {}^{14}\mathrm{R}_{blank} \tag{2.5}$$

with $^{14}\mathrm{R}_m$ as the measured ratio of the sample and $^{14}\mathrm{R}_{blank}$ as the blank ratio.

The second correction accounts for isotopic fractionation. Fractionation arises because isotopes of different mass participate differently in physical, chemical, and biological processes. For example, during photosynthesis, lighter isotopes are preferentially incorporated, leading to an enrichment of $^{12}$C relative to $^{13}$C and $^{14}$C in plant material [45].

Assuming that isotopic fractionation is primarily mass-dependent, the fractionation of $^{14}$C can be inferred from the measured $^{13}$R ratio. The fractionation-corrected ratio $^{14}\mathrm{R}_f$ is therefore related to the measured ratios via an empirical scaling relation. The effect on the ratio between masses 13 u and 12 u is assumed to be the same as the effect between the ratio between masses 14 u and 12 u. This means the measurement of $^{13}$R can be used for the correction where the fractionation corrected $^{14}\mathrm{R}_f$ is

$$\begin{aligned} ^{13}\mathrm{R}_f &= {}^{13}\mathrm{R} \cdot \mathrm{k} \\ ^{14}\mathrm{R}_f &\approx {}^{14}\mathrm{R} \cdot \mathrm{k}^{1.9} \end{aligned} \tag{2.6}$$

with k as the fractionation factor[5].

Instead of using $^{13}$R directly, isotopic compositions are commonly expressed in terms of $\delta^{13}$C values relative to the VPDB (Vienna Pee Dee Belemnite) standard. The $\delta^{13}$C value is defined as

$$\delta^{13}\mathrm{C} = \left( \frac{^{13}\mathrm{R}_s}{^{13}\mathrm{R}_{PDB}} - 1 \right) \cdot 1000 \text{ ‰}. \tag{2.7}$$

The isotopic composition expressed as $\delta^{13}$C, represents the relative deviation of $^{13}$R from the marine carbonate standard PDB (Pee Dee Belemnite), for which $^{13}\mathrm{R}_{PDB}$ = 0.0112372 [48]. In the 1980s VPDB was established as a replacement for the original PDB standard, which had become exhausted and was no longer available for direct measurement [49, 50].

Using $\delta^{13}$C, the fractionation correction factor $k$ can be defined as

$$\mathrm{k} = \frac{1 - 25 \text{ ‰}}{1 + \delta^{13}\mathrm{C}} \tag{2.8}$$

with a normalization to a sample of wood with $\delta^{13}$C=-25 ‰.

In addition to fractionation, transmission effects in the AMS system is the third correction that needs to be done. This is achieved by measuring a reference material

---

[5] If fractionation is treated as a purely kinematic process, an exponent of 1.9 is appropriate and is therefore used in the calculations of this thesis. Depending on the measurement technique and calculation approach, small deviations from this value are reported in the literature [47].

with known isotopic composition. The transmission-corrected ratio is given by

$$^{14}\mathrm{R}_{corr} = \frac{^{14}\mathrm{R}_{std}}{^{14}\mathrm{R}_{std,m}} \cdot {}^{14}\mathrm{R}_{m} \tag{2.9}$$

with $^{14}\mathrm{R}_{std}$ as the nominal ratio of a standard, $^{14}\mathrm{R}_{std,m}$ as the measured ratio of the standard and $^{14}\mathrm{R}_{m}$ as the measured ratio of a sample.

For historical reasons, $^{14}\mathrm{R}_{s}$ is expressed as a theoretical $^{14}\mathrm{R}$ which the sample had, if it would have been wood and calculated back to a ratio the sample would have had in year 1950:

$$\begin{aligned} ^{14}\mathrm{R}_{s} &= {}^{14}\mathrm{R}_{f} \cdot \exp\left(-\frac{\ln(2)}{5730\ \mathrm{a}} \cdot (y - 1950\ \mathrm{a})\right) \\ &= {}^{14}\mathrm{R}_{corr} \cdot \left(\frac{1 - 25\ ‰}{1 + \delta^{13}\mathrm{C}}\right)^{1.9} \cdot \exp\left(-\frac{\ln(2)}{5730\ \mathrm{a}} \cdot (\mathrm{y} - 1950\ \mathrm{a})\right) \end{aligned} \tag{2.10}$$

with y as the year of measurement and $^{14}\mathrm{R}_{corr}$ a transmission corrected ratio.

The fraction modern $\mathrm{F}^{14}\mathrm{C}$ can now be defined as

$$\mathrm{F}^{14}\mathrm{C} = \frac{^{14}\mathrm{R}_{s}}{^{14}\mathrm{R}_{Ox}} \cdot \mathrm{F}^{14}\mathrm{C}_{Ox}. \tag{2.11}$$

The value $^{14}\mathrm{R}_{std}$ in Eq. 2.4 is expressed in this thesis by a NIST standard Oxalic acid II (Ox-II, SRM 4990C) with an $\mathrm{F}^{14}\mathrm{C}_{Ox} = 1.3408$.

From $\mathrm{F}^{14}\mathrm{C}$, the conventional radiocarbon age can be calculated via

$$\begin{aligned} \mathrm{t} &= -\ln(\mathrm{F}^{14}\mathrm{C}) \cdot \frac{5568\ \mathrm{a}}{\ln(2)} \\ &= -\ln(\mathrm{F}^{14}\mathrm{C}) \cdot 8033\ \mathrm{a}. \end{aligned} \tag{2.12}$$

The conventional radiocarbon age is given in BP (Before Present) and is calculated with a carbon half-life determined by Libby. BP denotes a dating convention in which ages are expressed in years before 1950, which is the standard reference year in radiocarbon dating. The conventional radiocarbon ages continue to be calculated using the Libby value for historical consistency and are subsequently calibrated to calendar ages. Using calibration curves and programs such as OxCal, this age can then be converted to a calendar age (calBP).

## 2.3 Experimental Set-Up of COMORI

The experimental setup used for age determination of ultra-small samples (<200 $\mu$g C) consists of several interconnected instruments, each performing a specific function within the overall measurement process. The following sections provide an overview of the individual instruments and their respective functions. In this setup, solid samples are oxidized to $CO_2$, which is subsequently analyzed for its $\delta^{13}C$ value and $^{14}R$.

The oxidation of samples occurs with an Elemental Analyzer (EA) at high temperatures and the addition of oxygen. A part of the samples is transferred to an Isotope Ratio Mass Spectrometer (IRMS) for the measurement of $\delta^{13}C$. The rest of the sample is captured in the Gas Injection System (GIS) from where it is transferred to the ion source of the AMS for $^{14}R$ measurement.

The interaction between the EA, the IRMS, and the GIS is coordinated by the Gas Injection Control Software (GICS), originally developed by A. Stolz [51] and further adapted for the purposes of this work.

This system is now called COMORI (COmbustion and Measurement Of Radiocarbon and stable Isotopes) and used for measurements of small $CO_2$ with low $^{14}R$ ratios.

The COMORI system consists of:

- an EA (*vario isotope select*, Elementar, Germany)
- an IRMS (*isoprime precisION*, Elementar Analysensysteme GmbH)
- coupled to a GIS (IonPlus AG).

A picture of the COMORI setup can be seen in Fig. 2.3.

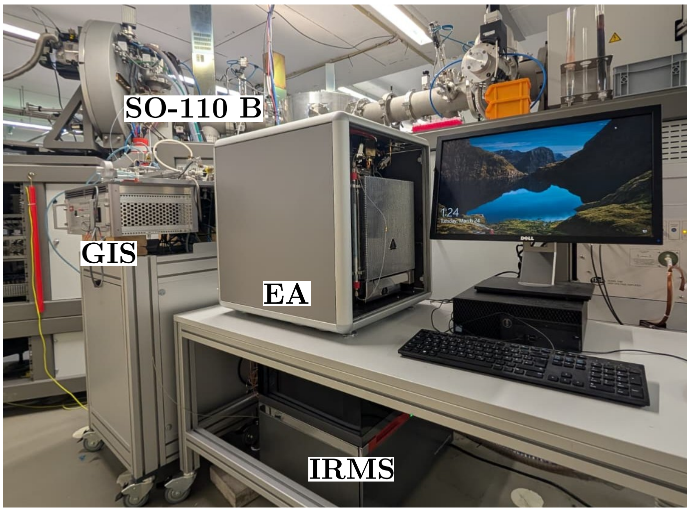

Figure 2.3: Photograph of the COMORI $CO_2$ system at the SO-110 B ion source of the 6 MV AMS system of CologneAMS, including the SO-110 B, Gas Injection System (GIS), Elemental Analyzer (EA), and Isotope Ratio Mass Spectrometer (IRMS).

Detailed descriptions of the complete setups are provided in the corresponding project manuscripts. Therefore, only the working principles of the individual components are discussed here. An overview of the full system, including the 6 MV AMS facility as well as the EA, IRMS, and GIS, is shown on the following page.

The abbreviations in the following figure are:

| | |
|---|---|
| **ACC** | Accelerator |
| **AFD** | Absorber Foil Detector |
| **ALIS** | Anion Laser Isobar Separator |
| **AP** | Aperture |
| **BI** | Bouncer Injector |
| **BIV** | Beamline Isolation Valve |
| **COMORI** | COmbustion and Measurement Of Radiocarbon and stable Isotopes |
| **DSW** | Detection Switching Magnet |
| **ESA** | ElectroStatic Analyzer |
| **FC** | Faraday Cup |
| **GIC** | Gas Ionization Detector |
| **HEE** | High Energy Electrostatic analyzer |
| **HEM** | High Energy Magnetic analyzer |
| **HES** | High Energy Steerer section |
| **OFC** | Offset Cup |
| **Q-Pole** | Quadrupole |
| **SCIV** | Sample Chamber Isolation Valve |

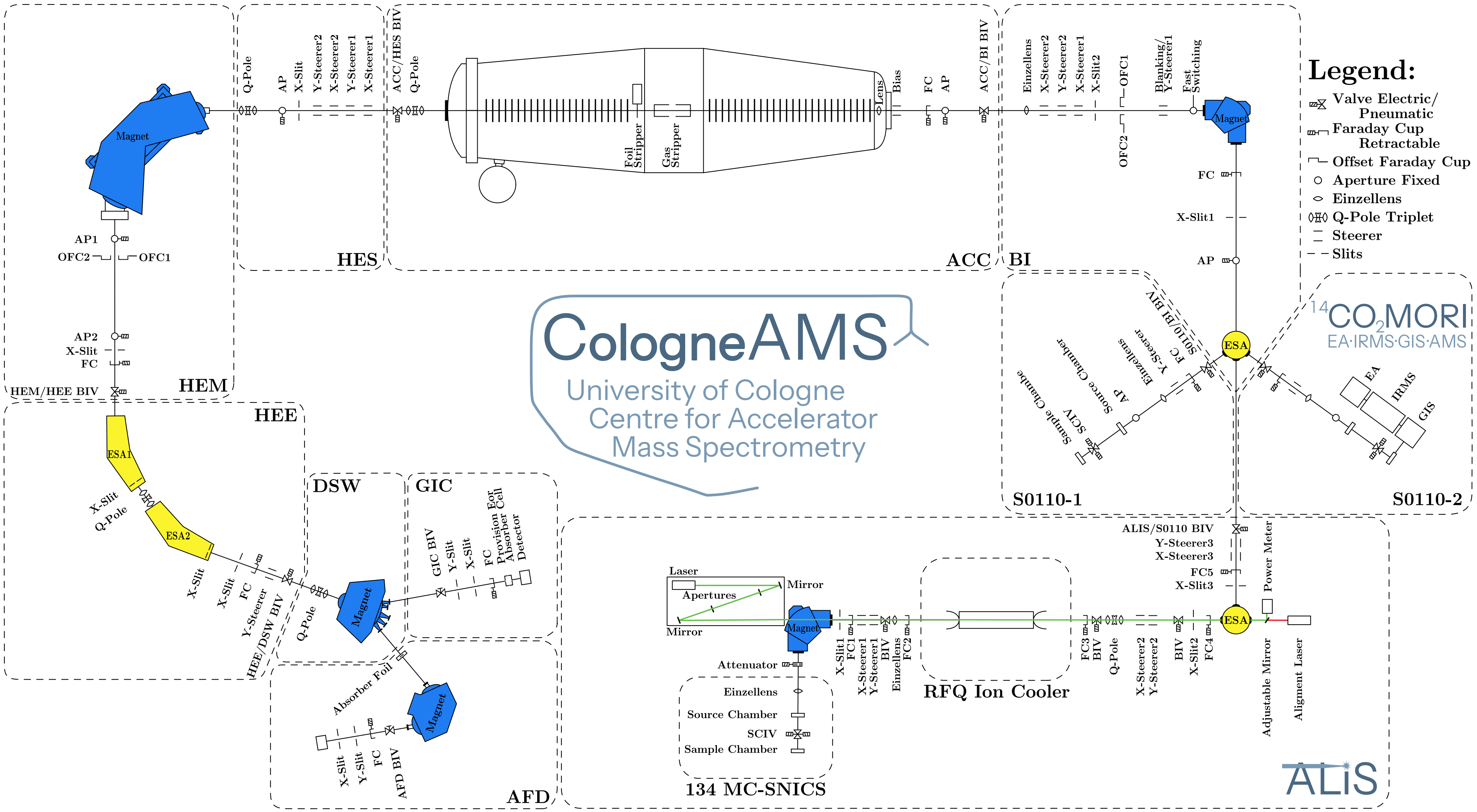
Legend:
Valve Electric/ Pneumatic
Faraday Cup Retractable
Offset Faraday Cup
Aperture Fixed
Einzellens
Q-Pole Triplet
Steerer
Slits
CologneAMS
University of Cologne
Centre for Accelerator Mass Spectrometry
14CO2MORI
EA·IRMS·GIS·AMS
ALIS
HEM
Magnet
AP1
OFC2
OFC1
AP2
X-Slit
FC
HEM/HEE BIV
HES
Q-Pole
AP
X-Slit
Y-Steerer2
X-Steerer2
Y-Steerer1
X-Steerer1
ACC/HES BIV
ACC
Q-Pole
Foil Stripper
Gas Stripper
Lens
Bias
FC
AP
ACC/BI BIV
BI
Einzellens
X-Steerer2
Y-Steerer2
X-Steerer1
X-Slit2
OFC1
OFC2
Blanking/ Y-Steerer1
Fast Switching
Magnet
FC
X-Slit1
AP
ESA
S0110-1
S0110/BI BIV
FC
Y-Steerer
Einzellens
AP
Source Chamber
SCIV
Sample Chambe
S0110-2
EA
IRMS
GIS
HEE
ESA1
X-Slit
Q-Pole
ESA2
X-Slit
X-Slit
FC
Y-Steerer
HEE/DSW BIV
DSW
Q-Pole
Magnet
GIC
GIC BIV
Y-Slit
X-Slit
FC
Provision For Absorber Cell
Detector
AFD
Absorber Foil
Magnet
AFD BIV
FC
Y-Slit
X-Slit
ALIS/S0110 BIV
Y-Steerer3
X-Steerer3
FC5
X-Slit3
Power Meter
ESA
Adjustable Mirror
Alignment Laser
Laser
Apertures
Mirror
Mirror
Magnet
Attenuator
X-Slit1
FC1
X-Steerer1
Y-Steerer1
BIV
Einzellens
FC2
RFQ Ion Cooler
FC3
BIV
Q-Pole
X-Steerer2
Y-Steerer2
BIV
X-Slit2
FC4
134 MC-SNICS
Einzellens
Source Chamber
SCIV
Sample Chamber

### 2.3.1 Elemental Analyzer

The EA enables the conversion of solid and liquid samples into gaseous compounds by high-temperature combustion in an oxygen atmosphere. In the CologneAMS setup, the EA is used to oxidize samples to $CO_2$, which is subsequently transferred to the GIS and, when required, partially (≈10 %) directed to the IRMS. When the IRMS is not used the complete sample is transferred to the GIS.

In the following, the main components and operation of the EA are described, including combustion, gas purification, separation, and detection.

The system uses helium (purity 99.999 %) as carrier gas and oxygen (purity 99.995 %) as oxidizing agent.

In the following, the EA system (Elementar Analysensysteme GmbH) used for the measurement of $CO_2$ samples with low $^{14}$R values is described.

#### Instrument setup

A schematic of the EA is shown in Fig. 2.4. The system consists of a combustion reactor, a reduction reactor, an absorption system, and a thermal conductivity detector (TCD). The combustion and the reduction reactor are filled according to

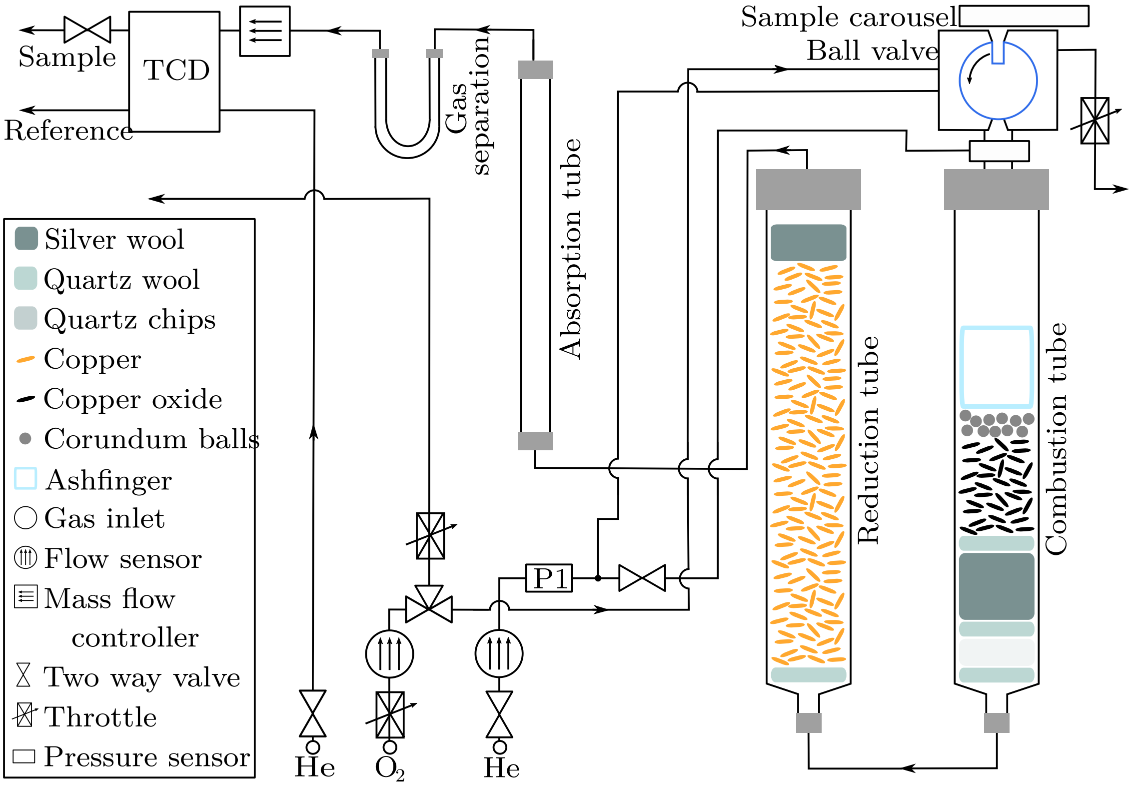

Figure 2.4: Schematic setup and reactor filling of the EA used for combustion of carbon samples. Samples are introduced individually through the ball valve into the combustion reactor, where they are oxidized, and the resulting gases are carried by helium into the reduction reactor. $CO_2$ is then separated in the gas separation column and detected by the thermal conductivity detector (TCD). Adapted from [16].

the type of samples that needs to be oxidizes. In case of carbon the filling mainly consist of silver wool, quartz wool and quartz chips, copper and copper oxide (CuO).

The combustion reactor operates at approximately 950°C. Samples are first packed into tin boats (4 × 4 × 11 mm) and are introduced into the reactor via a helium-flushed ball valve. In the presence of CuO and oxygen, the sample is oxidized, producing gases such as $CO_2$, $H_2O$, $N_2$, $NO_x$, and $SO_x$. Silver wool in the combustion reactor is used to remove sulfur compounds such as $SO_2$ and $SO_3$.

The gas mixture then passes through a heated quartz bridge, which prevents condensation, before entering the reduction reactor.

The reduction reactor is maintained at approximately 550°C and contains mainly copper, which reduces $NO_x$ to $N_2$. The resulting gas mixture is then separated in a temperature-programmed desorption column (Gas separation in Fig. 2.4). The programmed desorption column is initially kept at approximately 40°C, allowing all gases except $CO_2$ to pass through. The $CO_2$ is retained in the column. After the remaining gases have passed, the column is heated to around 210°C, at which point the retained $CO_2$ is released.

#### Detection

The gas composition is detected using the TCD. The TCD consists of two cells arranged in a Wheatstone bridge configuration to minimize signal drift. One cell is continuously flushed with helium and serves as a reference, while the sample gas flows through the second cell.

Differences in thermal conductivity between helium and the sample gas lead to a change in the resistance of a heated filament, resulting in a measurable voltage signal. This signal is digitized and recorded by the instrument software *vario ISOTOPE select*. The analyzed gas is then transferred to the IRMS for isotopic analysis.

The TCD detector of the EA can be calibrated with standards of known elemental content to determine the absolute carbon content. For $^{14}CO_2$ measurements at the AMS, however, the signal is used solely to confirm that enough $CO_2$ is present in the sample after combustion.

### 2.3.2 Isotopic Ratio Mass Spectrometer

The IRMS enables the determination of stable isotope ratios by ionizing gaseous samples and separates the resulting ions according to their mass-to-charge ratio. In this thesis the setup is used to determine the carbon isotopic composition of the sample, therefore determining $\delta^{13}C$. In the following, the ionization process, ion optics, mass separation and detection are described.

#### Instrument setup and detection

The IRMS is connected to the EA via a capillary system. A T-piece allows a small fraction of the sample gas, which is carried by helium to be directed into the IRMS. Only around 10 % of the sample gas leaving the EA enters the IRMS through the source inlet valve (SIV), while the remaining gas is transferred to the GIS.

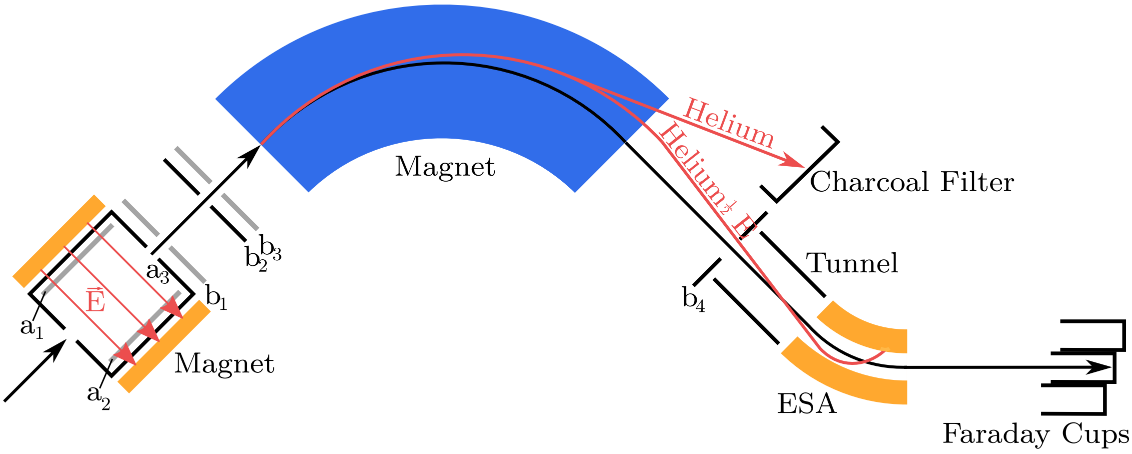

Figure 2.5: Schematic setup of the IRMS adapted from [16]. The slits $b_1$–$b_3$ are electrostatic steering elements used to direct the ion beam into the electromagnet. The collector slit $b_4$ suppresses unwanted $He^+$ ions. In addition, a charcoal trap collects neutral helium and reduces scattering within the IRMS.

The IRMS system consists of two main components: the *PrecisION* mass spectrometer and the *CentrION* interface unit. The CentrION controls gas handling, inlet and outlet flows, and pressure regulation, whereas the PrecisION performs the isotopic analysis.

The *PrecisION* IRMS determines isotope ratios of carbon, nitrogen, and sulfur, reported as $\delta^{13}C$, $\delta^{15}N$, and $\delta^{34}S$ values, which express the per mil deviation of a sample from an international standard [52, 53, 54]. The system comprises an ion source, flight tube, electromagnet, and ion collector, all powered by a 240 V/55 Hz supply, a schematic can be found in Fig. 2.5.

Inside the ion source, the molecules inside the sample gas are ionized by electron impact. The electrons are emitted from a thorium-coated filament (a1) and are accelerated towards a trap plate (a2). Thorium reduces the energy spread of the emitted electrons which improves the stability of the ion beam. An additional magnetic field between the top and bottom of the source creates a helical electron path, increasing the likelihood of ionization.

The resulting positive ions are accelerated towards the source slit (a3), then focused and steered by electrostatic plates (b1, b2) and Z-deflection plates (b3) into the flight tube.

The electromagnet bends the ions according to their mass-to-charge ratio (m/q), allowing the selection of species between 1 amu and 100 amu. In this setup, the system measures m/q 44, 45, 46 ($CO_2$) where $^{12}CO_2$ corresponds to 44, $^{13}CO_2$ corresponds to 45 and a mixture of different carbon isotopes and molecules corresponds to a mass of 46 amu. The flight tube is maintained at a vacuum of approximately $2 \cdot 10^{-8}$ mbar.

After magnetic separation, the ions pass through an electrostatic analyzer (ESA) consisting of two curved plates at different potentials, which remove low-energy $He^+$ ions created by residual collisions. Neutral helium is collected by a charcoal trap.

Ion detection occurs in three Faraday cups. The induced charge generates a voltage signal proportional to the ion intensity. The *PrecisION* system uses three

Faraday cups, allowing simultaneous detection of three masses, namely, m/q 44, 45, 46 for $CO_2$ measurements. Signals are recorded and processed using the *IonOS* software.

Finally, the measured ion beam intensities at m/q 44, 45, and 46 are converted into isotope ratios. After the necessary corrections are applied for the contributions of oxygen isotopes and instrumental background, the relevant carbon isotope ratio is derived from the signal ratios.

This ratio is then expressed in delta notation as $\delta^{13}$C, which represents the relative deviation of the isotope ratio of the sample from an international standard VPDB. The calculation of $\delta^{13}$C as explained in Chap. 2.2 is

$$\delta^{13}\mathrm{C} = \left(\frac{^{13}\mathrm{R}_s}{^{13}\mathrm{R}_{PDB}} - 1\right) \cdot 1000\ ‰. \tag{2.13}$$

### 2.3.3 Gas Injection System

The GIS from Ionplus AG enables the transfer of $CO_2$ samples from the EA to the AMS ion source. A schematic of the GIS is shown in Fig. 2.6. The GIS traps and dilutes the $CO_2$ before introducing it via a capillary into the ion source for

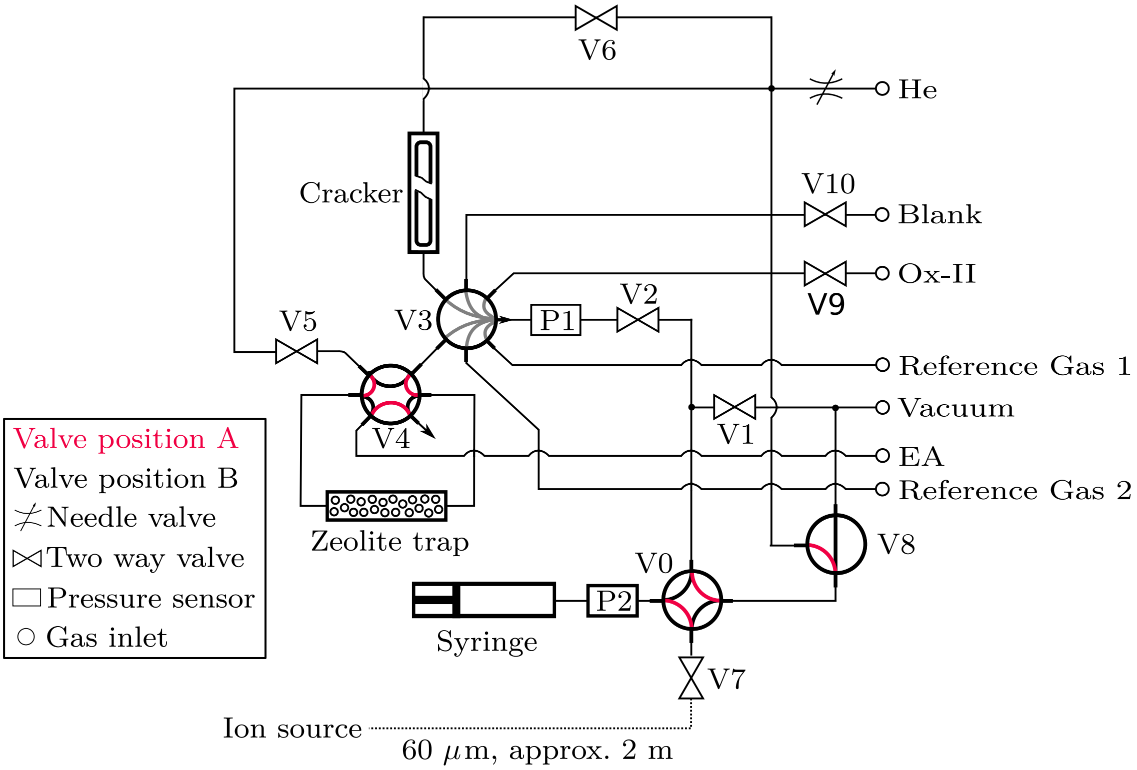

Figure 2.6: Schematic setup of the GIS adapted from [55]. The GIS has multiple inlets: the first is used for Ox-II standard gas, the second for blank gas, and the third for connection to the EA. The $CO_2$ produced in the EA is transferred to the cold zeolite trap while the valves are in position B. The zeolite trap retains the $CO_2$ while the helium carrier gas passes through. Once the complete sample has passed through the trap, the trap is heated to 450°C to release the $CO_2$ into the syringe.

radiocarbon measurement. In the following, the trapping, release, gas handling, and sample transfer processes are described.

The GIS was developed and implemented in 2020 [51]. In parallel, control software was developed to coordinate the EA, GIS, and AMS systems. This software was further extended in 2021 to integrate the EA–IRMS setup and establish the COMORI system [16].

$CO_2$ oxidized in the EA is transferred to the GIS. The gas passes through a cold (≈36°C) zeolite trap, where $CO_2$ is retained while other gases pass through. The trap is subsequently heated to approximately 450°C to release the trapped $CO_2$ into a syringe. To minimize $CO_2$ losses, helium is added to the sample such that the $CO_2$/He mixing ratio is between 2% and 5 %.

The sample gas is then transferred to the ion source of the AMS via a capillary with a diameter of 60 $\mu$m and a length of approximately 1.5 m.

## 2.4 Radiocarbon dating with microgram-scale $CO_2$ samples

The COMORI (COmbustion and Measurement Of Radiocarbon and stable Isotopes) setup allows quasi-simultaneous, high-precision determination of $\delta^{13}C$ by IRMS and $^{14}C$ by AMS from the same $CO_2$ sample. The following manuscript investigates whether the use of high-precision IRMS-derived $\delta^{13}C$ values, instead of AMS-derived values, improves the calculation of fraction modern ($F^{14}C$) and subsequently the conventional radiocarbon ages.

In addition to evaluating the influence of $\delta^{13}C$ precision on fractionation correction, the study examines the statistical behavior of $^{14}C$ counting, the effect of sample size on measurement accuracy, and the performance of an improved cleaning protocol for targets and target holders (components used in the ion source). The contamination level of the COMORI system is further quantified by means of a constant-contamination model.

### 2.4.1 I Manuscript: Toward reliable radiocarbon dating of microgram-scale $CO_2$ samples with COMORI

All AMS and IRMS measurements presented in this manuscript were performed for this work and prepared for publication. The blank-level investigations in the first half of Chap. 2.4.5 were carried out in collaboration with Tom Sittig, with the blank level study forming part of his Bachelor's thesis. The measurement concept, data evaluation, and interpretation presented in the publication were conducted for this work.

# I Manuscript:
# Toward reliable radiocarbon dating of microgram-scale $CO_2$ samples with COMORI

**Martina Gwozdz[1]**, Stefan Heinze[1], Markus Schiffer[1], Dennis Mücher[1]

[1]University of Cologne, Institute for Nuclear Physics, Zuelpicher Str. 77, Cologne, 50937, Germany

# Abstract

This study investigates whether high-precision $\delta^{13}C$ measurements obtained by Isotope Ratio Mass Spectrometry (IRMS) improve the determination of fraction modern carbon ($F^{14}C$) and conventional radiocarbon ages from AMS measurements of $^{14}CO_2$, compared with the use of $\delta^{13}C$ values derived directly from AMS. The IRMS is part of the COMORI (COmbustion and Measurement Of Radiocarbon and stable Isotopes) system at the 6MV AMS system in Cologne, which is used to oxidize, transfer, and measure carbon samples with IRMS and AMS.

Measurements of IAEA and NIST reference materials show a substantially lower standard deviation for IRMS-derived $\delta^{13}C$ values (0.26 ‰) than for AMS-derived values (2.33 ‰), while the mean values obtained by both methods agree with the information values. The differences between AMS-derived $\delta^{13}C$ values and their information values follow a Gaussian distribution. These deviations arise from a combination of instrumental effects and fractionation during measurement. Replacing AMS-derived $\delta^{13}C$ values in the fractionation correction with IRMS values leads to shifts of up to 100 years for individual samples. However, when considering the full dataset, the mean difference in conventional radiocarbon age is only about 20 years and remains statistically insignificant ($< 2\sigma$).

To better understand the large scatter of individual $F^{14}C$ values relative to their reference values, $CO_2$ measurements are presented and shown to demonstrate that $^{14}R$ ($^{14}C/^{12}C$) ratios are statistically distributed. For $CO_2$ samples, the uncertainties are dominated by $^{14}C$ counting statistics. Reliable conventional radiocarbon ages are obtained for carbon masses above approximately 10 $\mu$g, whereas smaller samples exhibit increasing deviations despite calibration with standards of similar sample size.

Overall, these results indicate that the improvement in $\delta^{13}C$ precision provided by IRMS has only a limited impact on radiocarbon age determination, as the uncertainties are dominated by $^{14}C$ counting statistics and other systematic effects, particularly for ultra-small samples. In addition, an improved cleaning protocol for targets and target holders reduced blank levels, and application of a constant-contamination model yields a COMORI system contamination of $1.05 \pm 0.26$ $\mu$g C.

## 2.4.2 Introduction

Accurate conventional radiocarbon ages depend on precise measurements of $F^{14}C$ and therefore require a reliable isotopic fractionation correction with $\delta^{13}C$. Prasad et al. (2019) [56] demonstrated that $\delta^{13}C$ values derived from AMS measurements are strongly instrument-dependent and generally less precise than IRMS values, and concluded that offline IRMS $\delta^{13}C$ remains a reliable option for fractionation correction. Building on these findings, the present study implements quasi-simultaneous IRMS $\delta^{13}C$ measurements within AMS measurements and quantitatively evaluates whether the improved $\delta^{13}C$ precision translates into measurable improvements in radiocarbon age determination, particularly for ultra-small samples.

At CologneAMS, radiocarbon measurements of $CO_2$ samples with carbon masses between 10 $\mu$g and 100 $\mu$g have been established using an Elemental Analyzer

(EA) coupled to a Gas Injection System (GIS), enabling the direct introduction of oxidized samples into the AMS ion source without graphitization [57]. This EA–GIS configuration significantly expanded AMS capabilities for samples with limited carbon availability ($<200$ $\mu$g C) and has since been routinely applied to a wide range of materials.

Now an Isotope Ratio Mass Spectrometer (IRMS; precisION, Elementar, Germany) coupled to an Elemental Analyzer (vario isotope select, Elementar, Germany) was integrated into the 6 MV AMS system at CologneAMS, replacing the previous EA setup. This development resulted in the COMORI setup, which enables automated, quasi-simultaneous measurements of high-precision $\delta^{13}$C by IRMS and $^{14}$R by AMS from the same $CO_2$ sample.

Using the COMORI setup, $CO_2$ samples are oxidized in an EA and split for quasi-simultaneous $\delta^{13}$C measurement by IRMS and $^{14}$C measurement by AMS.

The growing demand for precise $^{14}$R measurements of small samples, spanning a few $\mu$g to approximately 100 $\mu$g of carbon places stringent requirements on both radiocarbon and stable-isotope measurements. While AMS enables $^{14}$C detection with relative uncertainties below 0.6 % for $CO_2$ measurements of approximately 100 $\mu$g C, the direct determination of $\delta^{13}$C by AMS is limited in precision, with relative uncertainties of up to 40 %. Consequently, AMS-derived $\delta^{13}$C measurements frequently show increased scatter relative to information values, which compromises the accuracy of fractionation corrections.

The primary objective of this work is to evaluate whether the use of high-precision IRMS-derived $\delta^{13}$C values, replacing AMS-derived values, leads to a measurable improvement in conventional radiocarbon age determination. In addition, the influence of sample size, ion current, and counting statistics on the accuracy of conventional radiocarbon ages for ultra-small $CO_2$ samples is investigated. Finally, standardized cleaning procedures for targets and target holders, which are used to ionize the $^{14}CO_2$ in the ion source, are established and assessed in order to achieve a stable and low $^{14}$C background.

### 2.4.3 Experimental setup

The COMORI system at CologneAMS is designed for the oxidation and analysis of samples for $\delta^{13}$C and $^{14}$R measurements introduced into the AMS in gaseous form. Solid samples are weighed into pre-cleaned tin boats and combusted in an EA, where their total carbon content is determined. The EA used in this study is a *vario isotope select* (Elementar, Germany; serial no. 15191004), operated at a combustion temperature of 950°C with $O_2$ as the oxidizing agent.

Following combustion, $CO_2$ and other reaction gases are separated by Thermal Programmed Desorption (TPD). The purified $CO_2$ is then transported in a helium carrier-gas stream. At a T-piece, approximately 10 % of the $CO_2$ is diverted to the IRMS for stable-isotope analysis, while the remaining fraction is directed to the GIS, from where it can be transferred to the AMS ion source, as illustrated in Fig. 2.7.

Stable carbon isotope measurements are performed using an *isoprime precisION* IRMS (Elementar, Germany). The instrument consists of an ion source producing positive ions, a magnetic sector field for momentum separation, and an electrostatic

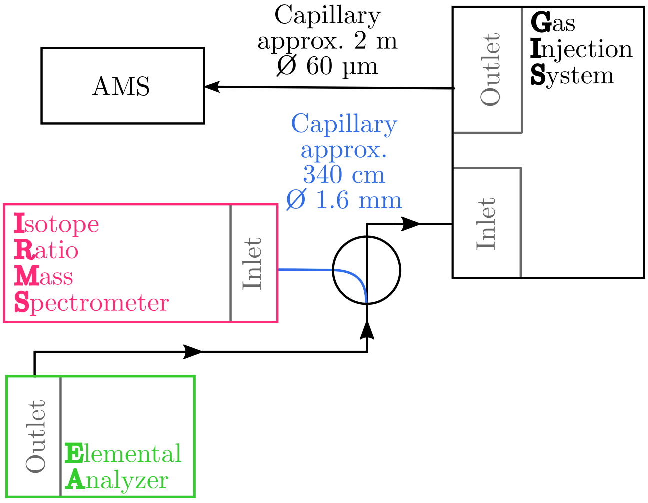

Figure 2.7: Simplified setup of COMORI for $CO_2$ measurements at the 6 MV AMS system of CologneAMS.

analyzer. The $CO_2$ ion beams corresponding to masses 44 (mainly $^{12}CO_2$) and 45 (mainly $^{13}CO_2$) are separated and simultaneously collected in Faraday cups, enabling high-precision determination of $\delta^{13}C$.

The GIS captures the $CO_2$ fraction intended for radiocarbon analysis using a zeolite trap. After trapping, the $CO_2$ is released from the zeolite trap by heating it to 360°C, collected in a syringe, mixed with helium, and transferred to the AMS ion source. Radiocarbon measurements are carried out using the HVE SO-110 B ion source, which has been in operation since 2015 [14]. Detailed descriptions of the EA–IRMS setup and the GIS are provided by Gwozdz et al. (2021) [16] and Stolz et al. (2019, 2020) [55, 51], respectively, with additional technical background by Wacker et al. (2013) [58].

### 2.4.4 Sample preparation

$CO_2$ measurements using COMORI differ from conventional graphite-based AMS analyses both in the measurement procedure and, in part, in the chemical preparation. Non-carbonate organic samples generally undergo an acid–base–acid (ABA) pretreatment to remove contaminating carbon, with the exact protocol depending on the sample matrix [59]. Up to the final preparation step, the chemical procedures are identical for samples analyzed with COMORI and for those converted to graphite. For example, tree-ring samples undergo the same chemical treatment prior to graphitization; however, for COMORI measurements the graphitization step is omitted, as the samples are directly oxidized in the EA. For different graphite samples the chemical treatment may differ depending on the sample material, the graphitization procedure itself remains the same [60, 61].

In addition to these preparation differences, the measurement procedures also differ. $CO_2$ samples are typically analyzed in their entirety in a single measurement run, whereas graphite targets are measured in repeated cycles, commonly lasting about five minutes per sample, with the sequence iterated over the full sample batch [62].

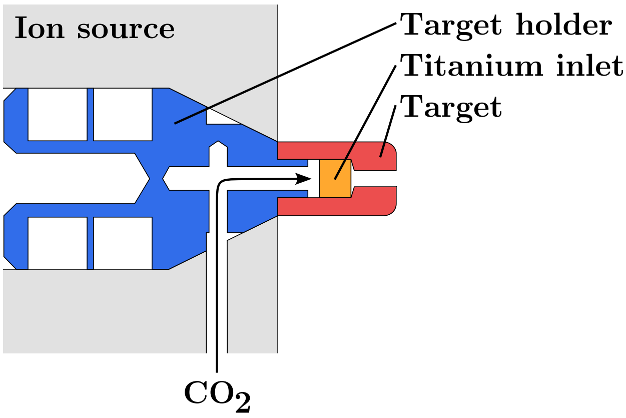

Figure 2.8: Schematic of the targets placed inside the ion source. Blue indicates the target holder, orange the titanium inlet, and red the aluminum target used for $CO_2$ measurements. The $CO_2$ enters the ion source through the target holder and flows past the titanium inlet into the source. The cubic form of the titanium inlet gives sufficient space along the sides for the gas to flow around the inlet and into the ion source. The schematic is based on the manual for the SO-110 ion source model by High Voltage Engineering.

### Preparing the targets for the blank measurements

The targets used for $CO_2$ measurements also differ from those used for graphite. Because the sample is not pressed directly into the target, a titanium inlet is used instead. A schematic of the sputter targets used at the 6 MV AMS system of CologneAMS is shown in Fig. 2.8. The targets consist of three components: an aluminum target body, a pressed titanium cube, and a target holder. $CO_2$ enters through an opening in the target holder and flows toward the titanium inlet within the target. The cubic titanium inlet is pressed into the cylindrical aluminum target, leaving gaps between the titanium and the target wall that allow the $CO_2$ to pass over the titanium inlet and into the ion source.

To identify the most effective cleaning routine for targets and target holders, blank measurements were prepared using 10 targets for a reference group (REF) and 10 targets for each additional cleaning procedure. In the reference group, only the aluminum targets were heated at 360°C for 24 hours. In the second batch, both the targets and the holders were heated at 360°C for 24 hours. In the third batch, only the targets were heated to 460°C for 24 hours. In the fourth batch, both targets and holders were heated to 460°C for 24 hours. The fifth batch was also heated to 460°C for 24 hours, and in addition the capillary leading the $CO_2$ from the GIS to the ion source was heated to 100°C during measurement. All batches were heated and then cooled under a constant argon flow. The cooling times were 3 minutes for the 360°C targets and 10 minutes for the different heating settings involving the target holders. The targets from the first batch were screwed onto unheated holders, whereas those from the second batch were attached to pre-heated holders. All batches were then placed directly into the ion source carousel. In addition, a batch of six targets and target holders heated at 360°C for 24 hours was prepared and placed directly into the ion source while still hot. An overview of the batches is given in Tab. 2.1.

Table 2.1: Overview of target and target holder cleaning procedures for blank measurements.

| **Parameter** | **REF** | **1** | **2** | **3** | **4** | **5** |
|---|---|---|---|---|---|---|
| Target Heating [°C] | 360 | 360 | 460 | 460 | 460 | 360 |
| Holder Heating [°C] | - | 360 | - | 460 | 460 | 360 |
| Capillary Heating [°C] | - | - | - | - | 100 | - |
| Cooling Time [min] | 3 | 10 | 10 | 10 | 10 | - |

**Preparing the samples for the standard measurements**

The sample preparation for the blank and $\delta^{13}$C measurements is identical.

NIST-Ox-II, IAEA-c6, IAEA-c8, IAEA-c1 standards, and blank material were weighed into cleaned tin boats. The tin boats used had dimensions of $4\times4\times11$ mm ($H\times W\times L$) and were manufactured by Elementar (Germany). The tin boats were cleaned with organic solvents, including two rinses with acetone (≥99.9 %, supra trace), followed by three rinses with dichloromethane (HPLC grade; Rethemeyer et al. 2013 [63]). The carbon masses used ranged from 5 to 230 $\mu$g.

### 2.4.5 Results - $\delta^{13}$C from AMS and IRMS and its impact on the conventional radiocarbon age

In general, fractionation effects can occur during sample preparation, during measurement, or may already be inherent to the sample itself prior to handling [65, 66, 67, 68, 69]. For example, during carbon fixation in plants, $^{12}$C is incorporated preferentially relative to $^{13}$C, and $^{13}$C relative to $^{14}$C. This fractionation occurs because heavier isotopes tend to react slower during photosynthetic carbon fixation[6] [45, 71]. Hence, $\delta^{13}$C is an important indicator of sample origin: marine samples generally show relatively high $\delta^{13}$C values, whereas many forms of vegetation show lower $\delta^{13}$C values [72, 73, 45].

According to current scientific practice, $\delta^{13}$C is determined either simultaneously with $^{14}$C by AMS or separately by IRMS. Because AMS-derived $\delta^{13}$C values often scatter by several permil, additional IRMS measurements, with a much better precision well below one permil, are used in AMS laboratories, for example, at the ETH Zürich [74].

With COMORI, $\delta^{13}$C can be measured online and quasi-simultaneously by IRMS and AMS from the same sample. Two measurement series using two IAEA standards are shown in Fig. 2.9. These measurements were performed on samples oxidized in the EA and then split for analysis by IRMS and AMS, with masses typically above 100 $\mu$g.

The overall scatter of $\delta^{13}$C values measured with the 6 MV AMS system at CologneAMS is 2.33 ‰, compared with 0.26 ‰ for the IRMS values. For IAEA-c6, the AMS data yield an average of -9.31 ‰ and a standard deviation of 3.10 ‰. For IAEA-c8, the average is -18.56 ‰ with a standard deviation of 1.67 ‰. The information value of IAEA-c6 is -10.8 ‰. On average, the AMS-derived $\delta^{13}$C values

---

[6] Carbon fixation is the conversion of inorganic carbon from $CO_2$ into organic compounds during photosynthesis [70].

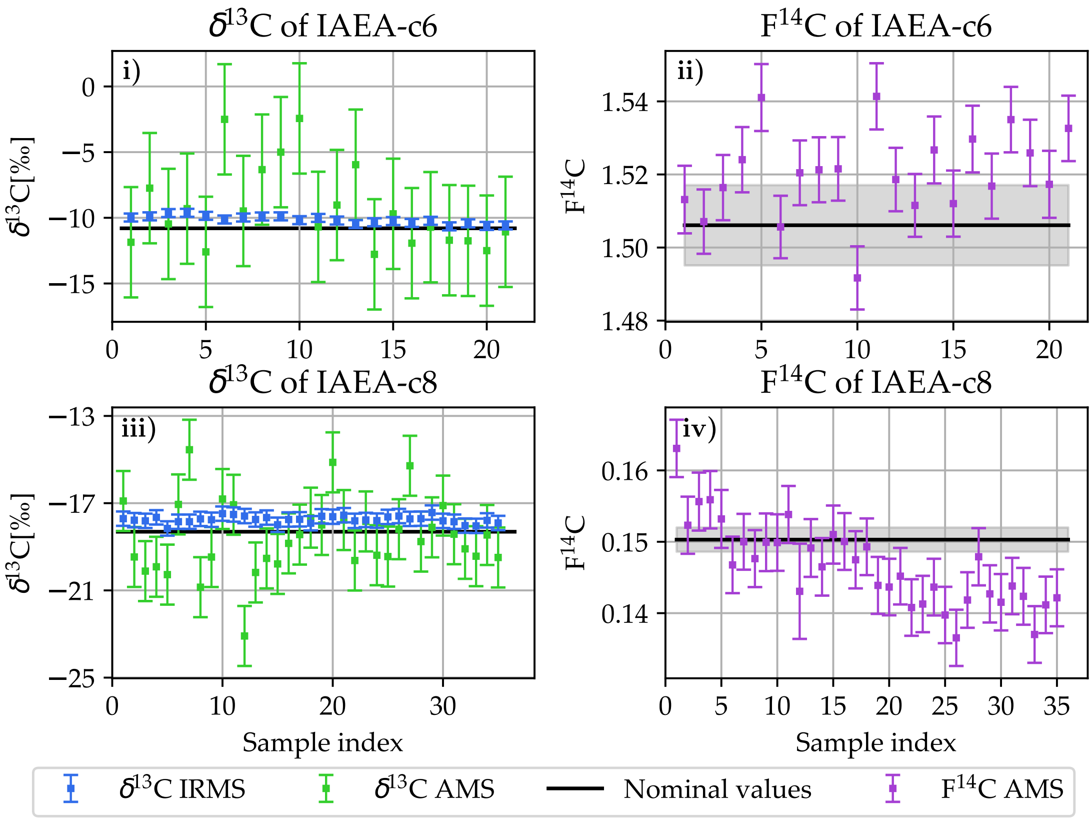

Figure 2.9: Comparison of $\delta^{13}$C and F$^{14}$C measurements for the IAEA-c6 and IAEA-c8 standards. Panels i) and iii) show the $\delta^{13}$C values measured by AMS (green) and IRMS (blue), alongside with the information values (black) [64]. Panels ii) and iv) show the corresponding F$^{14}$C values measured by AMS for the same standards. In each case, the $\delta^{13}$C and F$^{14}$C values shown in panels i) and ii), and in panels iii) and iv), were obtained from the same standard material.

agree with the information value within the uncertainty, however, some samples, such as IAEA-c6 with sample indices 6 and 10 or IAEA-c8 with sample indices 7 and 12, show scatter greater than 40 %.

In the determination of F$^{14}$C in $CO_2$ AMS measurements, uncertainties in F$^{14}$C of up to 10 % are common [57, 75]. The corresponding F$^{14}$C values shown in Fig. 2.9 ii) and iv) agree with the reference values within this range, showing scatter of up to 10 %.

Although the AMS-derived $\delta^{13}$C values exhibit substantially larger scatter than the corresponding IRMS measurements (2.33 ‰ vs. 0.26 ‰), their mean values remain close to the information values (-9.31 ‰ vs. -10.8 ‰ for IAEA-c6). Individual AMS measurements however, deviate strongly both from the $\delta^{13}$C information values and from one another, whereas the IRMS data show much smaller dispersion.

The magnitude and non-systematic nature of the AMS scatter observed for identical sample material exceed what would be expected from fractionation effects alone. Some studies report fractionation effects ranging from a few percent up to about 40 %. However, these investigations were typically conducted under deliberately extreme or non-routine operating conditions [76, 77]. Under stable operating

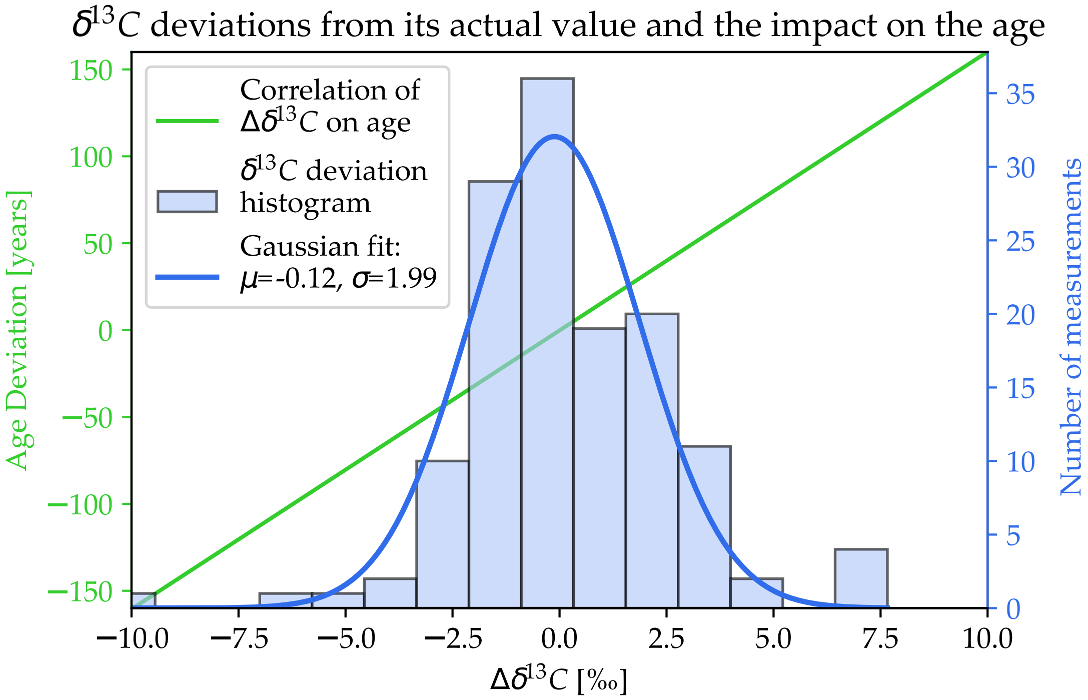

Figure 2.10: Histogram of the deviations in $\delta^{13}$C from the information values used for AMS measurements (blue bars). The blue curve shows a Gaussian fit to the distribution. The green line (left y-axis) indicates the corresponding deviation in radiocarbon age resulting from a given $\Delta\delta^{13}$C.

conditions and for comparable sample sizes, the calibration procedure should largely cancel such fractionation effects, leading to the assumption that IRMS values may improve the calculation of $F^{14}$C.

The key question, therefore, is whether the observed $\delta^{13}$C scatter is large enough to affect the calculated conventional radiocarbon age. In general, it is well established that the conventional radiocarbon age changes by approximately 16 years for a $\delta^{13}$C deviation of 1 ‰ [78]. The impact of the observed $\delta^{13}$C scatter on the age calculation is therefore assessed. Figure 2.9 shows the scatter of AMS-measured $\delta^{13}$C values relative to their information values from IAEA-c6 and IAEA-c8 standards. The distribution of these deviations, expressed as $\Delta\delta^{13}$C, is presented in Fig. 2.10. In total, 18 IAEA-c1 and 29 IAEA-c6 were measured in addition to the 21 IAEA-c6 and 35 IAEA-c8 already shown, and all are included in the statistics presented here.

To a good approximation, the histogram shows a Gaussian distribution. Although the residuals scatter around $\mu = -0.12$, there remains a non-negligible probability of observing large deviations of up to approximately ±10 ‰. This implies that, for an unknown sample, a deviation of this magnitude in $\delta^{13}$C can result in an age offset of 160 years. The fitted Gaussian has a $\sigma$ of 1.99. For some samples, deviations of around $4\sigma$ occur, corresponding to an actual $\delta^{13}$C deviation of 9.68 ‰.

Since even comparatively small deviations in $\delta^{13}$C can propagate into substantial convetional radiocarbon age offsets, it is important to examine how $\delta^{13}$C is calculated in AMS measurements. In general, the calculation of $\delta^{13}$C for a carbon measurement with AMS is

$$\delta^{13}\mathrm{C} = \left( \frac{\mathbf{a} \cdot {}^{13}\mathrm{R}_s \left( \frac{\delta^{13}\mathrm{C}_{Std}}{1000‰} + 1 \right)}{{}^{13}\mathrm{R}_{Std}} - 1 \right) 1000‰ \tag{2.14}$$

with $^{13}\mathrm{R}_s$ the $^{13}$R of the sample with unknown ratio and $^{13}\mathrm{R}_{std}$ the $^{13}$R of a standard material.

For AMS measurements, the parameter $a$ in the calculation of $\delta^{13}$C is nominally equal to one. A deviation of $\delta^{13}$C from its true value corresponds to a change in the $^{13}$R ratio, which can be expressed as a deviation of the parameter **a** from unity. The resulting impact on the calculated conventional radiocarbon age follows a logarithmic dependence, Age $\propto \ln(\mathbf{a})$, implying that small variations in **a**, and therefore in $\delta^{13}$C, lead to changes in the derived age. The condition for small variation is fulfilled, as the deviations in $\delta^{13}$C of up to 10 ‰ correspond to values a within ±0.008.

From this relationship, the age change resulting from a given $\delta^{13}$C deviation can be represented by the linear function added in Fig. 2.10. The linear correlation indicates that a $\delta^{13}$C deviation of 1 ‰ corresponds to an age deviation of approximately 16 years, consistent with the relationship discussed above.

While the logarithmic dependence of the conventional radiocarbon age on the parameter **a** implies that deviations in $\delta^{13}$C can introduce measurable age offsets, the magnitude of this effect must be evaluated using actual sample data. This motivates a direct comparison of age calculations based on AMS-derived and IRMS-derived $\delta^{13}$C values.

For this reason, a series of IAEA-c6 measurements was recalculated by replacing the AMS-derived $\delta^{13}$C value in the fractionation correction with the corresponding IRMS-derived value, as shown in Fig. 2.11. The conventional radiocarbon ages were calculated using the established blank subtraction and normalization with Ox-II described by Wacker et al. (2010) [46].

The substitution leads to measurable changes in the calculated ages of up to 100 years for individual samples. In cases where the AMS-derived $\delta^{13}$C values are lower than expected, the correction results in an increase in the calculated age (e.g., sample indices 6–12), whereas for samples with higher-than-expected AMS ages (e.g., sample indices 1–4), the correction acts in the opposite direction.

The standard deviation of the mean is also included in the plot. The mean conventional radiocarbon age obtained using IRMS-corrected $\delta^{13}$C values is -3 325.7 years BP, with an uncertainty of ±13.9 years BP. The conventional radiocarbon age is negative in this case because the Ox-II standard has a $^{14}$R value greater than the modern level and therefore corresponds to an apparent age in the future. The corresponding AMS-only dataset yields a mean age of -3 345.5 years BP ±13.5 years BP. In both cases, the standard deviation of the mean is calculated as the sample standard deviation divided by the square root of the number of measurements, reflecting the statistical uncertainty of the estimated mean rather than the spread of individual ages.

Both mean values lie within approximately 35–57 years of the reference age of -3 289 years BP, corresponding to a deviation of up to 2 %. The difference

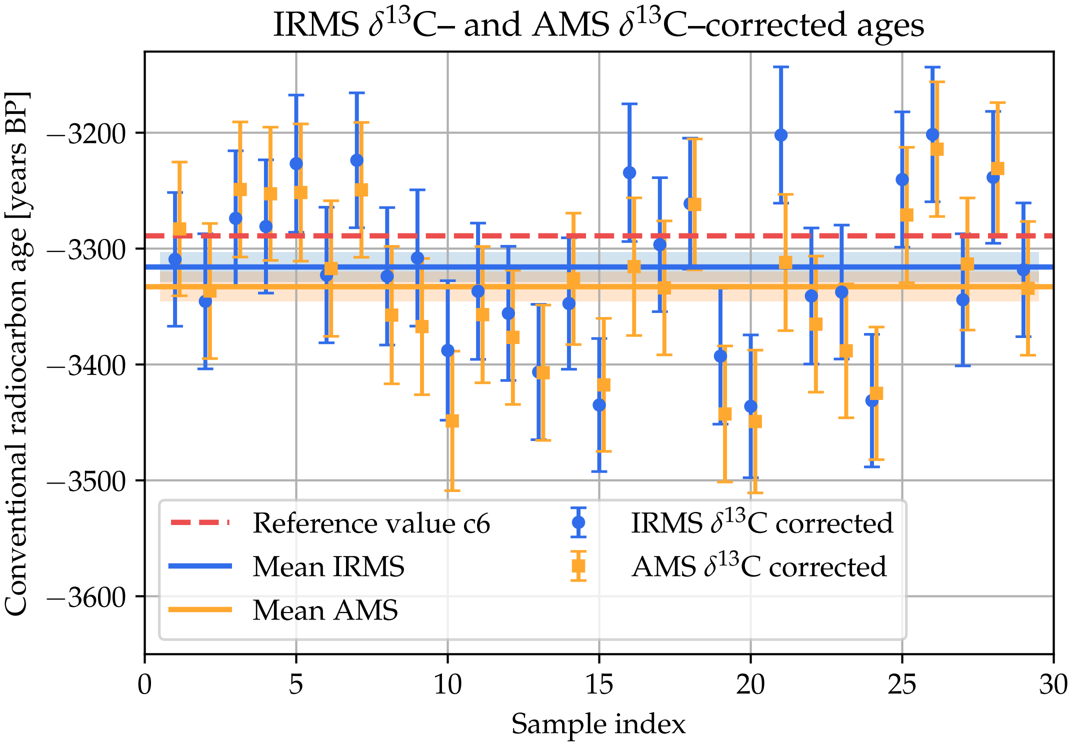

Figure 2.11: Conventional radiocarbon ages calculated for IAEA-c6 standard material, which has a $^{14}$R ratio greater than modern due to an artificially enhanced $^{14}$C. As a result, the calculated conventional radiocarbon ages are negative, indicating that they lie approximately 3 300 years "in the future" relative to the reference year 1950. The blue circles show ages calculated using IRMS-derived $\delta^{13}$C values; the blue line indicates the mean and the light-blue band the standard deviation of the mean. The same is shown for AMS-derived $\delta^{13}$C values in orange. The reference value is calculated from the F$^{14}$C reference value of IAEA-c6, 1.5061 [45].

between the two means is 19.7 years BP, corresponding to a $1.5\sigma$ deviation, well within statistical expectations. This suggests that other statistical and systematic effects, in addition to fractionation correction, play a substantial role in the age determination.

In the case of $CO_2$ AMS measurements, this implies that statistical and systematic uncertainties may dominate the results, thereby limiting the benefit of IRMS-derived $\delta^{13}$C corrections. To illustrate these statistical and systematic effects, a $CO_2$ measurement of Ox-II with the EA–GIS–AMS setup is shown in Fig. 2.12. The $^{12}$C and $^{13}$C currents are measured in the high-energy-side Faraday cup and plotted over the measurement time for a single $CO_2$ sample. The $^{14}$C counts are measured with a gas ionization detector.

A clear variation of the high-energy current over time is observed. In graphite targets, similar current changes occur due to the formation of craters in the target material during sputtering, which increases the exposed surface area and consequently the ion yield [79, 18]. In $CO_2$ measurements, craters do not form in the sample material itself; however, small changes in the ion current can arise from changes at the titanium inlet surface of the target. In addition, part of the current

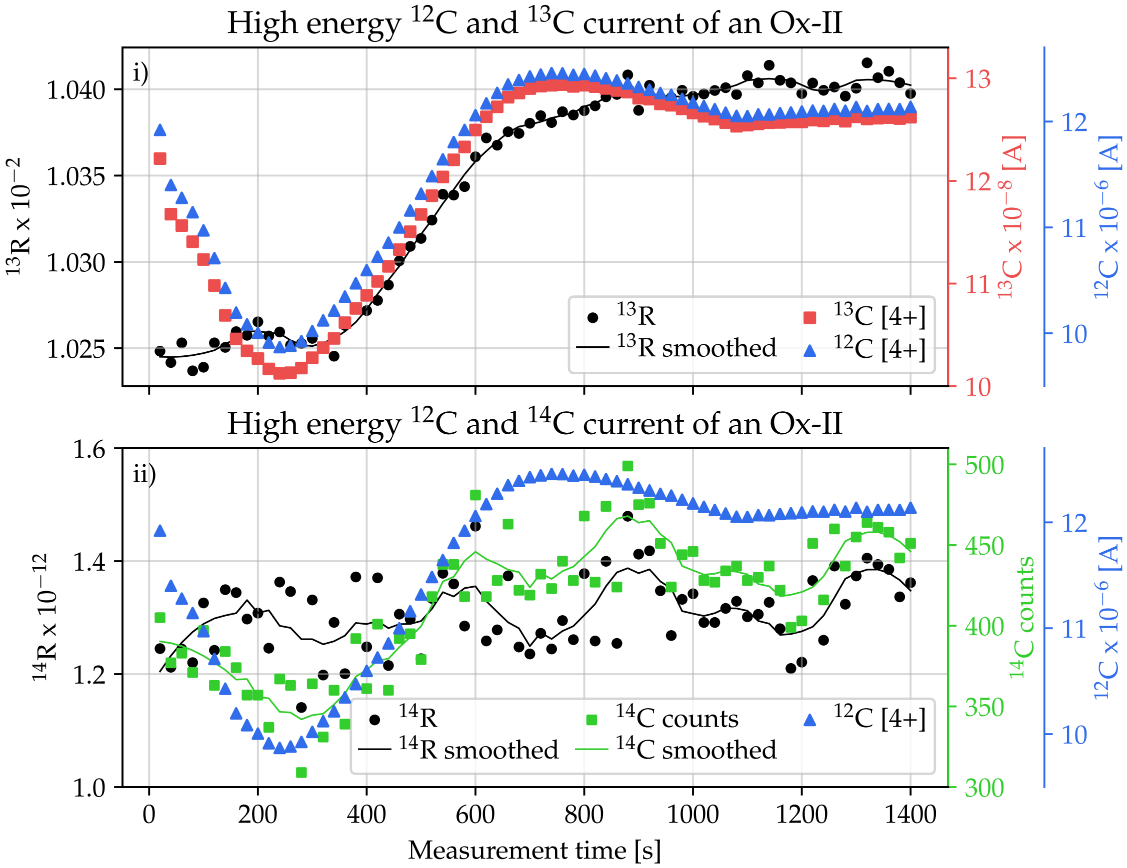

Figure 2.12: Measurement of an NIST Ox-II sample as $CO_2$. The standard was measured in one continuous run with COMORI at the SO-110 B ion source. Figure i) shows the high-energy currents of $^{12}C$ (blue) and $^{13}C$ (red), with the corresponding $^{13}R$ ratio shown in black. Figure ii) shows the $^{14}C$ counts (green) and the $^{14}R$ ratio in black.

variation can be attributed to the time required for the GIS syringe to stabilize the $CO_2$ mass flow. In each measurement, the pressure in the GIS syringe requires some time to reach a steady flow of approximately 1.4 $\mu$g per minute, after which the high-energy currents also stabilize.

In the $CO_2$ measurement shown in Fig. 2.12, an 80 $\mu$g sample is measured. The rise and fall of the current are relatively rapid, and a stable region is reached after about 1 000 s (≈16 min). The relative fluctuations of these currents are given in Tab. 2.2. Although the individual relative fluctuations of $^{12}C$ and $^{13}C$ are substantial, reaching up to 8 %, these variations largely cancel when their ratio, $^{13}R$, is formed. As a result, the relative scatter in $^{13}R$, which is used to determine the conventional radiocarbon age, is only 0.62 %. In contrast, the $^{14}C$ signal requires more careful interpretation. While the instantaneous $^{14}C$ count rate shows a rel-

Table 2.2: Results for the relative uncertainty of the different measurement parameters.

| | $^{12}C$ | $^{13}C$ | $^{14}C$ | $^{13}R$ | $^{14}R$ | $^{14}C$ Counts |
|---|---|---|---|---|---|---|
| relative scattering [%] | 7.38 | 7.90 | 9.89 | 0.62 | 5.17 | 29 032 |

ative scatter of nearly 10%, the Poisson uncertainty of the total integrated counts over the full measurement is only $1/\sqrt{N} = 0.59$ % for N = 29 032. The larger value reflects statistical fluctuations in short counting intervals with few events, whereas the smaller value describes the uncertainty of the total accumulated counts.

A similar distinction applies to the ratio $^{14}$R. When $^{14}$R is evaluated in short time segments, the low number of $^{14}$C counts in each segment leads to relatively large fluctuations, which are reflected in the observed scatter of the time-resolved $^{14}$R values. It primarily reflects the limited counting statistics of $^{14}$C in each time interval. In comparison, the stable-isotope currents are much larger, and the corresponding $^{13}$R ratio is therefore far less affected by counting uncertainties. This is consistent with the much smaller relative scatter of $^{13}$R (0.62 %) compared with $^{14}$R (5.17 %).

For the interpretation of the full $CO_2$ measurement, the relevant quantity is the uncertainty of the integrated $^{14}$R ratio obtained from the complete run. This uncertainty is governed mainly by the finite total number of detected $^{14}$C counts, whereas the variations of the $^{12}$C and $^{13}$C currents over time do not introduce an observable systematic bias into the final ratio. In other words, the within-run fluctuations of the $^{14}$C count rate are consistent with counting statistics, and the precision of the final $^{14}$R value is limited primarily by the total number of $^{14}$C counts collected during the measurement rather than by a drift in the stable isotope currents.

To test whether any additional systematic effects are present which could not be explained by statistical fluctuations, the stability of the $^{14}$R ratio over time shown in Fig. 2.12 ii) was evaluated using a Poisson model. Since $^{14}$C and $^{12}$C are treated here as the numbers of detected particles in each block (with one block corresponding to 20 s of measurement time), a single constant isotopic ratio, denoted by $\hat{\lambda}$, was estimated from the full dataset, yielding $\hat{\lambda} = 1.309647 \cdot 10^{-12}$. Under the null hypothesis of a time-independent isotopic ratio, the expected number of $^{14}$C particles in block $i$ is given by

$$\mu_i = \hat{\lambda}\, {}^{12}C_i, \tag{2.15}$$

and the observed number of $^{14}$C particles is assumed to follow

$${}^{14}C_i \propto \text{Poisson}(\mu_i). \tag{2.16}$$

The goodness of fit of this model was assessed using the Pearson chi-square statistic [80],

$$\chi^2 = \sum_i \frac{({}^{14}C_i - \mu_i)^2}{\mu_i}, \tag{2.17}$$

which is appropriate for Poisson-distributed data because, for a Poisson process, the variance is equal to the expectation value. With 70 blocks and one fitted parameter, the number of degrees of freedom is 69. The resulting Pearson statistic was $\chi^2 = 76.17$ ($p = 0.259$). This value is well above 0.05, indicating that the observed deviations from the constant-ratio model are compatible with statistical fluctuations.

In addition, the Poisson deviance [80],

$$D = 2 \sum_i \left[ {}^{14}C_i \ln\left(\frac{{}^{14}C_i}{\mu_i}\right) - ({}^{14}C_i - \mu_i) \right], \tag{2.18}$$

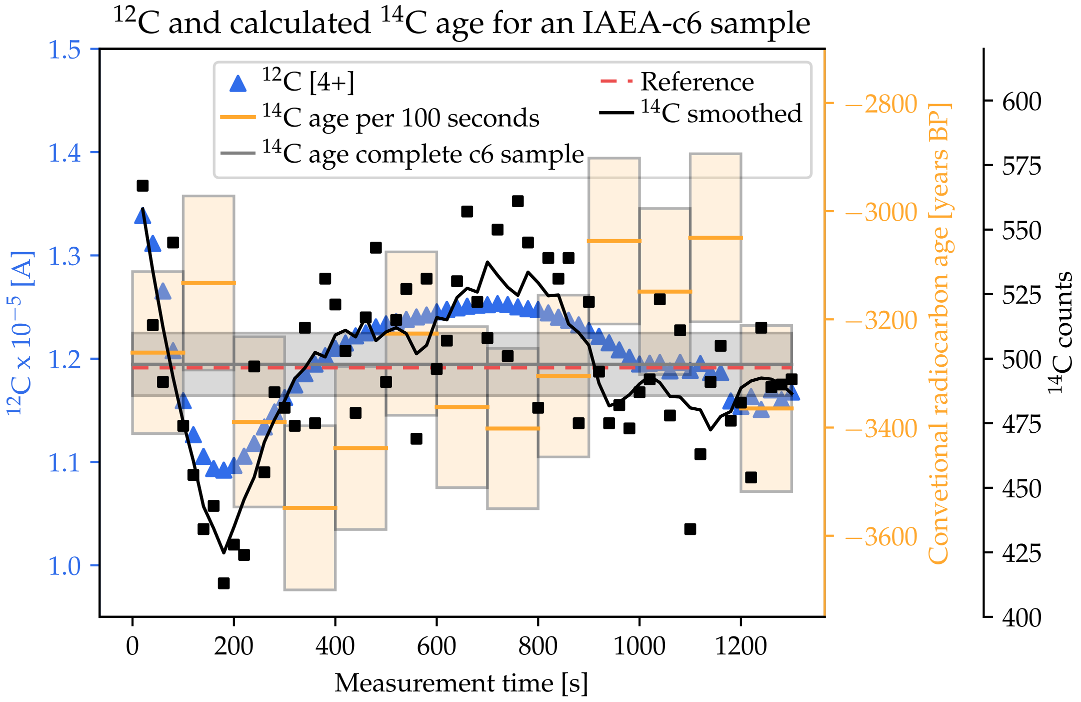

Figure 2.13: IAEA-c6 is a standard with a $^{14}$R ratio above modern, resulting in a negative conventional radiocarbon age that corresponds to a date “in the future” relative to the reference year 1950. The conventional radiocarbon ages calculated for consecutive 100 s sections are shown in orange, with the corresponding uncertainties indicated in light orange. The conventional radiocarbon age derived from the complete IAEA-c6 sample is shown in gray, with its associated uncertainty indicated in light gray. The reference value of the conventional radiocarbon age is calculated from the F$^{14}$C reference value of IAEA-c6, 1.5061, and is shown in red. The measured $\delta^{13}C_{VPDB}$ values are -9.84 ‰ by IRMS and -8.13 ‰ by AMS; the information value is -10.8 ‰ [45].

was 76.08 ($p$ = 0.261). Since this value is close to the number of degrees of freedom ($df$ = 69) and the corresponding $p$-value is well above 0.05, the deviations between the observed and expected $^{14}$C counts are consistent with Poisson fluctuations.

The dispersion parameter, defined as $\phi = \chi^2/df$, was 1.104, consistent with only minimal deviation from a Poisson behavior. These results show that the observed block-to-block variability is consistent with statistical fluctuations around a constant $^{14}$R ratio and provides no evidence for additional systematic drifts.

This behavior is also reflected in the conventional radiocarbon age calculations. Figure 2.13 illustrates this for an IAEA-c6 standard, for which the conventional radiocarbon age is calculated for consecutive 100 s sections and shown alongside with the corresponding uncertainties. The uncertainties of the individual intervals range from 149 to 155 years BP. For most of the measurement duration, the section-based conventional radiocarbon ages agree within uncertainty with the age obtained from the complete dataset, which has an uncertainty of 57.7 years BP. The section ages do not follow the temporal evolution of either the $^{12}$C current or the $^{14}$C count

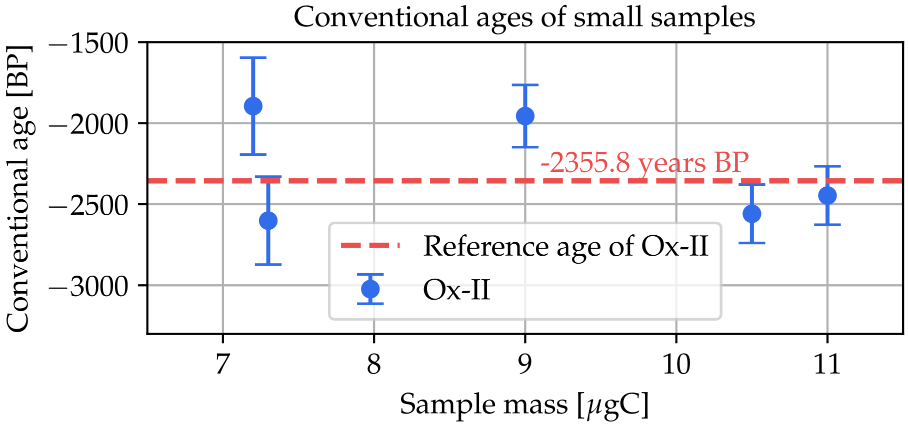

Figure 2.14: NIST Ox-II is a standard with a $^{14}$R ratio above modern, resulting in a negative conventional radiocarbon age that corresponds to a date “in the future” relative to the reference year 1950. The NIST Ox-II , which are treated as unknown samples in the measurements are corrected with NIST Ox-II (not shown here) of the same mass range NIST Ox-II is 1.3408 with a conventional radiocarbon age of -2 355.8 years BP.

rate. No systematic dependence of the calculated conventional radiocarbon age on the $^{12}$C current is observed. This indicates that the scatter of the interval-based ages is dominated primarily by the limited $^{14}$C counting statistics in the individual 100 s sections rather than by instrumental drift or by variations in the stable-isotope currents.

Finally, the question remains to what extent reliable conventional radiocarbon ages can be obtained from small samples. To address this, five Ox-II samples, which are also used in this study to determine the contamination of the samples, are evaluated. The resulting ages are shown in Fig. 2.14. For samples with carbon masses exceeding 10 $\mu$g C, the conventional radiocarbon ages agree with the reference value within their respective uncertainties. In contrast, two of the smallest samples exhibit deviations of up to 20 % relative to the reference value. Although these low-mass samples were calibrated using standards of comparable size, their conventional radiocarbon ages still show increased deviations from the expected value. This observation indicates that, while small samples can provide indicative age information, larger sample sizes generally yield more reliable age determinations.

### Blank level and constant contamination

For reliable $^{14}CO_2$ measurements, a low and well-characterized blank level must be ensured. Therefore, improvements in target processing were evaluated.

The processing of targets and target holders was investigated by measuring blank gas from a standard blank gas bottle. The samples were already gaseous, with each sample having a mass of 40 $\mu$g.

The resulting F$^{14}$C values for blank measurements performed after different heating procedures are shown in Fig. 2.15. The average F$^{14}$C value of the reference

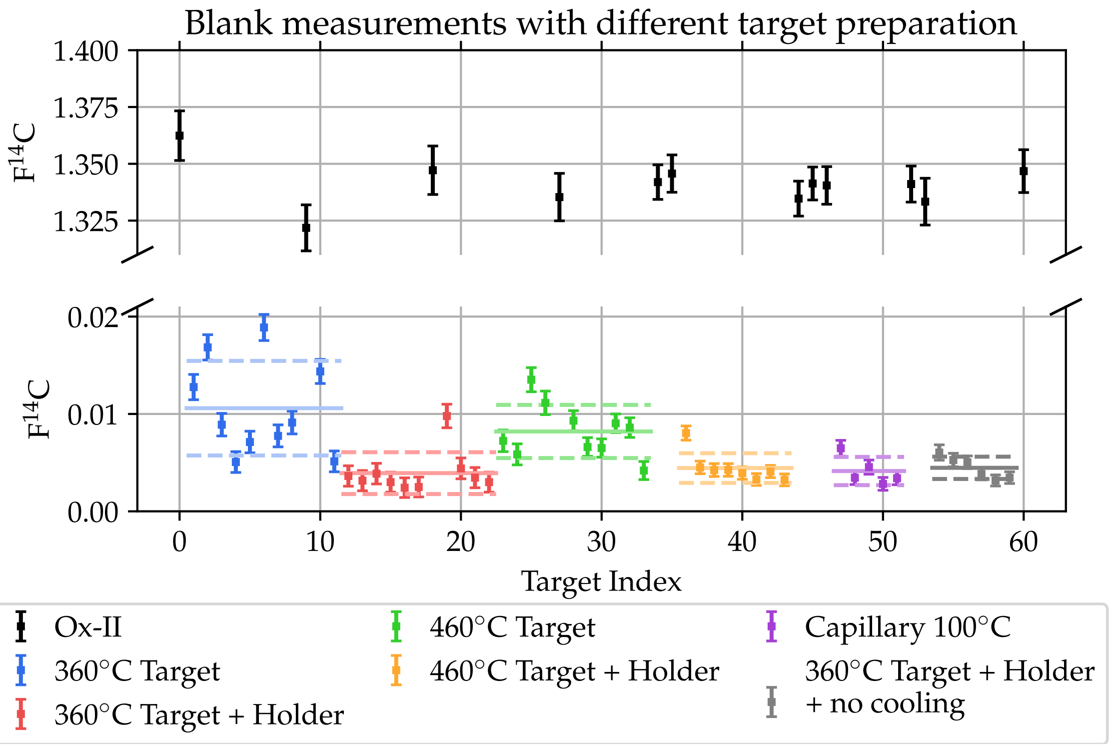

Figure 2.15: The blank measurements are plotted as a function of target index, with the different colors representing the individual groups of prepared targets and target holders. The black data points represent the Ox-II standards measured alongside the blanks for normalization. Both the blank samples and the Ox-II standards contain approximately 40 $\mu$g of carbon. The upper plot shows the Ox-II measurements, while the lower plot shows the blanks. The horizontal lines indicate the mean $F^{14}C$ value of each preparation group, while the dashed horizontal lines represent the corresponding standard deviation.

measurements, for which only the target was heated to 360°C (blue in Fig. 2.15), is 0.01059 ± 0.00486. In comparison, heating both the target and the holder to 360°C (red in Fig. 2.15) yields a lower $F^{14}C$ value of 0.00392 ± 0.00215, corresponding to an improvement of 63 %.

When the targets and holders are instead heated to 460°C (yellow in Fig. 2.15), an $F^{14}C$ value of 0.00444 ± 0.00152 is obtained. Although the standard deviation decreases, no further reduction in the $F^{14}C$ value is observed.

A comparison between targets heated only to 360°C and those heated to 460°C (green in Fig. 2.15) shows that the latter yield an $F^{14}C$ value of 0.00820 ± 0.00272, corresponding to an improvement of 23 %.

Another significant effect is an increase in the $F^{14}C$ ratio of blank samples measured directly after an Ox-II standard. In such cases, blank levels increase by up to 120 %.

Additional cleaning steps using acetone and ultrasound treatment were also tested, but did not result in a significant improvement. A measurement using targets and holders cleaned with acetone and ultrasound and heated to 360°C yielded a higher $F^{14}C$ value of 0.00538 ± 0.00187 and is therefore not shown here.

Another measurement series was performed using targets and holders heated to 360°C, with additional heating of the capillary connecting the GIS to the ion source. This temperature was chosen because discoloration of the holder was observed after heating to 460°C, raising concerns that repeated exposure to higher temperatures could lead to a loss of the holder's magnetism, which is essential for insertion into and extraction from the ion source. The capillary was heated to approximately 100°C using a heating wire. This temperature represented the maximum attainable value with the heating wire and its associated power supply (transformer). The capillary consists of fused silica (⌀60 $\mu$m, ≈1.5 m). The resulting $F^{14}C$ value is 0.00414 ± 0.00145 (purple in Fig. 2.15). The last measurement series (gray in Fig. 2.15), in which the hot target and target holder were inserted directly into the ion source, yielded a mean blank value of $F^{14}C = 0.004468 \pm 0.00114$.

In summary, the results show that improvements in target processing are achieved primarily by heating the target and target holder and inserting them directly into the ion source while still hot. This is the simplest and fastest way to achieve a low and reliable blank level. This procedure is also the least expensive, as no argon is required for cooling.

After the cleaning procedure had been established, a blank and Ox-II mass series was prepared, with blank standard material weighed into tin boats and oxidized in the EA. The resulting $F^{14}C$ values of the blank and standard measurements are shown in Fig. 2.16 i) and ii).

In total, 26 samples were measured, with carbon masses ranging between 5 $\mu$g and 220 $\mu$g for both Ox-II and blank samples. All measurements were performed on a single day, using targets and target holders that had been heated in an oven at 360°C prior to measurement and immediately placed into the sample wheel under vacuum.

From these data it can be seen that sample masses below 10 $\mu$g can be measured, but yield larger uncertainties and increased scatter. Above 10 $\mu$g, the $F^{14}C$ values are stable.

In addition, the data were processed to determine the extraneous carbon contribution for each sample using the constant-contamination model established by Hanke et al. (2017) [81]. This was done to enable comparison with the previous EA–GIS–AMS setup [57]. The model is based on the assumption that exogenous contamination with fraction modern carbon $F_C$ and mass $m_C$ contributes to the measured total $F^{14}C_M$ of a sample with measured mass $m_M$. This contamination is composed of a modern carbon component, for which $F^{14}C$ is one, and a $^{14}$C-free component, for which $F^{14}C$ is zero. Haghipour et al. (2019) published a Matlab script with which the exogenous carbon contribution can be determined [82]. The model is based on the mass-balance relation

$$F^{14}C_S = \frac{F^{14}C_M \cdot m_M - F^{14}C_C \cdot m_C}{m_M - m_C} \tag{2.19}$$

Here, $F^{14}C_M$ refers to the measured total sample value, and $m_M$ is the sum of the sample mass $m_S$ and the contamination mass $m_C$. Propagation of the corresponding uncertainties yields

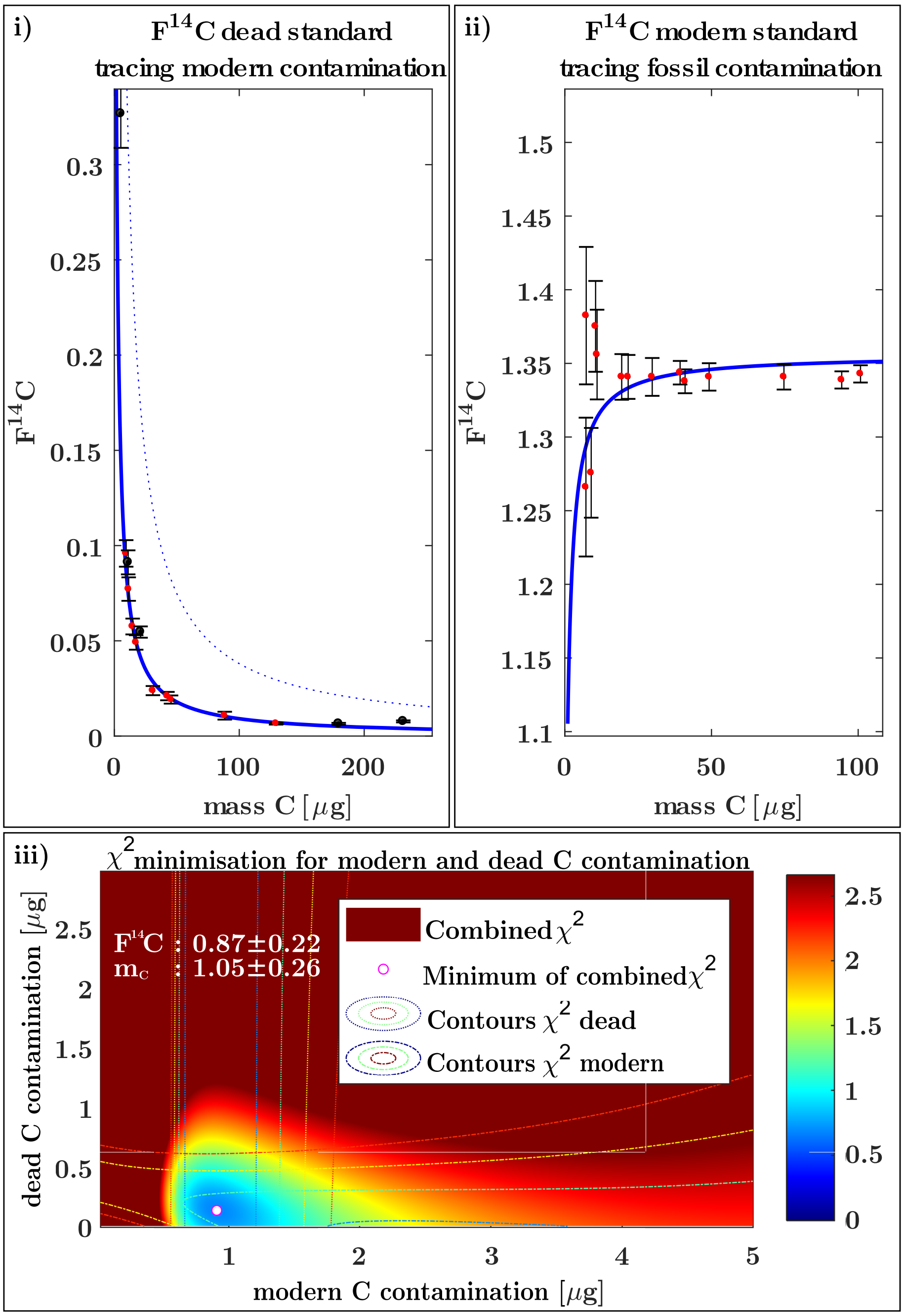

Figure 2.16: $F^{14}C$ plotted against sample mass for i) blank standards and ii) NIST Ox-II standards. The fit of the constant-contamination model is shown in blue, with the blue dotted line indicating the $1\sigma$ uncertainty. The red data points are included in the model, whereas the black data points are outliers. Panel iii) shows the $\chi^2$ minimization as a function of dead and modern contamination, with the circle indicating one possible solution.

$$\begin{aligned}
\sigma^2_{\mathrm{F^{14}C}_S} = {} & \left[\sigma_{\mathrm{m}_C}\left(\frac{\mathrm{F^{14}C}_M \cdot \mathrm{m}_M - \mathrm{F^{14}C}_C \cdot \mathrm{m}_C}{\mathrm{m}_M - \mathrm{m}_C}\right) - \left(\frac{\mathrm{F^{14}C}_C}{\mathrm{m}_M - \mathrm{m}_C}\right)\right]^2 \\
& + \left[\sigma_{\mathrm{m}_M}\left(\frac{\mathrm{F^{14}C}_M}{\mathrm{m}_M - \mathrm{m}_C} - \frac{\mathrm{F^{14}C}_M \cdot \mathrm{m}_M - \mathrm{F^{14}C}_C \cdot \mathrm{m}_C}{(\mathrm{m}_M - \mathrm{m}_C)^2}\right)\right]^2 \\
& + \left[\sigma^2_{\mathrm{F^{14}C}_M}\frac{\mathrm{m}_M}{\mathrm{m}_M - \mathrm{m}_C}\right]^2 + \left[\sigma^2_{\mathrm{F^{14}C}_C}\frac{-\mathrm{m}_C}{\mathrm{m}_M - \mathrm{m}_C}\right]^2 .
\end{aligned} \tag{2.20}$$

The depleted and modern standards are used to determine the modern and dead contamination components, respectively, with $\mathrm{F^{14}C}_C$ given by

$$\mathrm{F^{14}C}_C = \frac{\mathrm{F^{14}C}_{\mathrm{modern}} \cdot \mathrm{m}_{\mathrm{modern}}}{\mathrm{m}_{\mathrm{dead}} + \mathrm{m}_{\mathrm{modern}}} \tag{2.21}$$

with $\mathrm{m}_C$

$$\mathrm{m}_C = \mathrm{m}_{\mathrm{depleted}} + \mathrm{m}_{\mathrm{modern}}. \tag{2.22}$$

The Matlab script of Haghipour et al. (2018) determines the masses of modern and dead contamination using a least-squares approach. The model evaluates how well the measured data match a constant-contamination scenario by computing $\chi^2$ over a grid of possible contamination masses, varied in steps of 0.02 $\mu$g C. The contaminant-mass combination that minimizes $\chi^2$ is selected, and the 95 % $\chi^2$ limits define the $2\sigma$ uncertainties.

The constant-contamination model is shown in Fig. 2.16 and yields a contamination of 1.05 ± 0.26 $\mu$g C with a corresponding $\mathrm{F^{14}C} = 0.87 \pm 0.22$. Of this, 0.91 $\mu$g C is attributed to modern contamination and 0.14 $\mu$g C to dead-carbon contamination.

At first sight, the fit in Fig. 2.16 ii) does not appear to reproduce the measured data well. However, this behavior follows directly from the constant-contamination model. Rearranging Eq. 2.19 yields

$$\mathrm{F^{14}C}_M = \mathrm{F^{14}C}_S + \left(\mathrm{F^{14}C}_C - \mathrm{F^{14}C}_S\right)\frac{\mathrm{m}_C}{\mathrm{m}_M}. \tag{2.23}$$

For samples with smaller masses, the ratio $\mathrm{m}_C/\mathrm{m}_M$ approaches unity with $\mathrm{m}_M = \mathrm{m}_S + \mathrm{m}_C$. Consequently, as $\mathrm{m}_S$ tends toward zero, the fit approaches $\mathrm{F^{14}C}_C$.

### 2.4.6 Conclusion

This publication presents the first investigation of quasi-simultaneous $\delta^{13}$C measurements by IRMS and AMS alongside with $^{14}$R measurements from the same $\mathrm{CO_2}$ sample. Because IRMS requires only a small amount of $\mathrm{CO_2}$, it can be used reliably even for small samples. Furthermore, the scatter of $\delta^{13}$C values measured by AMS is consistent with results reported by other institutes. Although AMS systems can show different standard deviations for $\delta^{13}$C, values of around 2 to 3 ‰ are typical [83, 84]. With a standard deviation of 2.33 ‰, the 6 MV AMS system of CologneAMS therefore performs within the expected range.

As expected, the IRMS-derived $\delta^{13}$C values show substantially less scatter, namely 0.26 ‰, which is at the lower end of the range of 0.3–0.6 ‰ reported by other institutes [83].

The statistical and systematic effects in AMS measurements were investigated with particular focus on the carbon current at the high-energy side of the AMS and on the impact of $\delta^{13}$C scatter on radiocarbon age calculation. The $CO_2$ measurements show a clear time dependence of the carbon currents. In $CO_2$ measurements, these effects can be attributed primarily to pressure stabilization in the GIS. However, these current variations have no significant influence on the measured $^{14}$R ratios. The $\chi^2$ tests do not reject the hypothesis that the $^{14}$R values are statistically distributed, and any potential effects caused by scattered $\delta^{13}$C values are dominated by the counting uncertainty of $^{14}$C.

The impact on conventional radiocarbon age calculation is potentially significant, because a $\delta^{13}$C deviation of 1 ‰ corresponds to an age offset of approximately 16 years, and deviations of up to 3.5 ‰ occur with non-negligible probability. However, because the $^{14}$R measurements have larger uncertainties, deviations from the reference conventional radiocarbon age are dominated primarily by the statistical uncertainties of $^{14}$C. Nevertheless, large $\delta^{13}$C deviations can lead to conventional radiocarbon age offsets of several decades. In contrast, IRMS-derived $\delta^{13}$C measurements show significantly lower scatter (0.26 ‰) and can therefore provide a more stable basis for fractionation correction. Accordingly, when multiple related samples are measured and the AMS-derived $\delta^{13}$C values show unexplained scatter, the use of independently measured IRMS-derived $\delta^{13}$C values is recommended to improve the accuracy of the age calculation, provided that other possible sources of deviation have been carefully excluded. For individual samples, however, this approach is less suitable, and the conventional correction using AMS-derived $\delta^{13}$C should be retained.

Furthermore, samples down to about 10 $\mu$g C can be measured reliably with respect to their conventional radiocarbon age, whereas age calculations for even smaller samples should be treated with caution.

The most reliable target preparation which yields the lowest blank level achieved by COMORI is 0.00392 ± 0.00215 (44 500 radiocarbon years). When the target and target holder are inserted directly into the ion source while still hot, an even smaller uncertainty is obtained, namely 0.004468 ± 0.00114. For comparison, the former EA–GIS–AMS setup reported a blank level of 0.0127 ± 0.0012 for 50 $\mu$g [57], corresponding to an improvement of approximately 69 %.

The constant contamination of the COMORI setup was determined to be 1.05 ± 0.22 $\mu$g C, corresponding to an F$^{14}$C value of 0.87 ± 0.22. Within uncertainty, this isotopic ratio is consistent with that reported for the previously used setup, for which an F$^{14}$C value of 0.93 ± 0.23 was obtained [57]. However, the corresponding constant contamination is higher than in the earlier setup, where a value of 0.30 ± 0.08 $\mu$g C was reported. Possible explanations are the longer capillaries and larger EA reactor volumes in COMORI relative to the previous setup contributing to an intrinsic constant contamination that cannot easily be reduced.

# Acknowledgment

We would like to acknowledge Prof. Dr. Rethemeyer and her group for providing access to their laboratory facilities and for their support in weighing some of the

standard materials.

## Appendix

The radiocarbon calculations in this work follow the outline of Lund (2011) [45]. After the measured $^{14}$R values undergo a blank subtraction, the $\delta^{13}$C fractionation correction of the AMS system is calculated. The $\delta^{13}$C of a sample is the relative deviation of its $^{13}C/^{12}C$ to a $^{13}C/^{12}C$ of a standard. The standard can be PDB with $^{13}C/^{12}C_{PDB} = 0.0112372$ or $^{13}C/^{12}C_{VPDB} = 0.0111802$. The definition of $\delta^{13}$C for an unknown sample is

$$\delta^{13}\mathrm{C} = \left(\frac{^{13}\mathrm{R}_S -^{13} \mathrm{R}_{VPDB}}{^{13}\mathrm{R}_{VPDB}}\right) \cdot 1000‰$$

with $\mathrm{R}_S$ as $^{13}C/^{12}C$ of the measured sample and $^{13}\mathrm{R}_{VPDB}$ as the $^{13}C/^{12}C_{VPDB}$. In case of AMS measurements $\delta^{13}$C needs to be expressed relative to the used standard material. Then the calculation would be as followed with $^{13}\mathrm{R}_{Std}$ as the $^{13}C/^{12}C$ of the standard material.

$$\begin{aligned}
\delta^{13}\mathrm{C} &= \left(\frac{^{13}\mathrm{R}_s \cdot {}^{13}\mathrm{R}_{Std} - {}^{13}\mathrm{R}_{VPDB} \cdot {}^{13}\mathrm{R}_{Std}}{^{13}\mathrm{R}_{VPDB} \cdot {}^{13}\mathrm{R}_{Std}}\right) 1000‰ \\
&= \left(\frac{^{13}\mathrm{R}_s \cdot {}^{13}\mathrm{R}_{Std} - {}^{13}\mathrm{R}_{VPDB} \cdot {}^{13}\mathrm{R}_{Std} + {}^{13}\mathrm{R}_s \cdot {}^{13}\mathrm{R}_{VPDB} - {}^{13}\mathrm{R}_s \cdot {}^{13}\mathrm{R}_{VPDB}}{^{13}\mathrm{R}_{VPDB} \cdot {}^{13}\mathrm{R}_{Std}}\right) 1000‰ \\
&= \left(\frac{\frac{^{13}\mathrm{R}_s \cdot {}^{13}\mathrm{R}_{Std}}{^{13}\mathrm{R}_{VPDB}} - {}^{13}\mathrm{R}_{Std} + {}^{13}\mathrm{R}_s - {}^{13}\mathrm{R}_s}{^{13}\mathrm{R}_{Std}}\right) 1000‰ \\
&= \left(\frac{^{13}\mathrm{R}_s \left(\frac{^{13}\mathrm{R}_{Std}}{^{13}\mathrm{R}_{VPDB}} - 1\right) - {}^{13}\mathrm{R}_{Std} + {}^{13}\mathrm{R}_s}{^{13}\mathrm{R}_{Std}}\right) 1000‰ \\
&= \left(\frac{^{13}\mathrm{R}_s \left(\frac{\delta^{13}C_{Std}}{1000‰}\right) - {}^{13}\mathrm{R}_{Std} + {}^{13}\mathrm{R}_s}{^{13}\mathrm{R}_{Std}}\right) 1000‰ \\
&= \left(\frac{^{13}\mathrm{R}_s \left(\frac{\delta^{13}C_{Std}}{1000‰} + 1\right) - {}^{13}\mathrm{R}_{Std}}{^{13}\mathrm{R}_{Std}}\right) 1000‰ \\
&= \left(\frac{^{13}\mathrm{R}_s \left(\frac{\delta^{13}C_{Std}}{1000‰} + 1\right)}{^{13}\mathrm{R}_{Std}} - 1\right) 1000‰
\end{aligned}$$

## 2.5 Summary

The new COMORI setup at the 6 MV AMS system of CologneAMS allows the quasi-simultaneous measurement of $\delta^{13}$C by IRMS and $^{14}$C by AMS from the same $CO_2$ sample. Using this setup, it was investigated whether high-precision $\delta^{13}$C measurements obtained by IRMS improve the determination of fraction modern carbon (F$^{14}$C) and conventional radiocarbon ages compared with $\delta^{13}$C values derived directly from AMS.

Measurements of IAEA and NIST reference materials demonstrate a clear difference in precision between the two techniques. AMS-derived $\delta^{13}$C values show a standard deviation of 2.33 ‰, whereas IRMS measurements achieve a significantly smaller scatter of 0.26 ‰. Despite this difference in precision, the mean $\delta^{13}$C values obtained by both methods agree with the information values of the standards within their uncertainties. The deviations of AMS-derived $\delta^{13}$C values from their information values follow a Gaussian distribution centered close to zero.

The influence of these differences in $\delta^{13}$C on the calculated conventional radiocarbon age was evaluated by substituting AMS-derived $\delta^{13}$C values with the corresponding IRMS measurements in the fractionation correction. Individual samples exhibit age shifts of up to approximately 100 years when corrected with IRMS data. However, the mean difference between ages calculated using AMS- and IRMS-derived $\delta^{13}$C values is about 20 years and remains statistically insignificant within the measurement uncertainty.

Further investigation of the AMS measurements shows that the variability in $^{14}$R ratios is dominated by $^{14}$C counting statistics rather than by systematic effects related to the AMS measurement. Analysis of the carbon currents and $^{14}$C count rates during $CO_2$ measurements demonstrates that fluctuations in ion currents do not introduce systematic biases into the $^{14}$R ratio. A Pearson $\chi^2$ test confirms that the measured $^{14}$R values are statistically distributed and consistent with the expected counting statistics.

The impact of sample size on radiocarbon age determination was also examined. Measurements of Ox-II samples with carbon masses between 5 $\mu$g C and 220 $\mu$g show that reliable conventional radiocarbon ages are obtained for samples larger than approximately 10 $\mu$g C. Smaller samples exhibit increasing scatter and deviations from the reference value despite calibration with standards of comparable mass.

In addition to these investigations, improved cleaning procedures for targets and target holders were developed in order to reduce background contamination in $CO_2$ measurements. Heating both targets and holders prior to measurement significantly reduced blank levels compared with earlier procedures. Application of the constant-contamination model indicates a total contamination of 1.05 ± 0.26 $\mu$g C for the COMORI system, consisting predominantly of modern carbon.

The investigations presented here demonstrate that $CO_2$ AMS measurements with the COMORI setup provide a reliable approach for high-precision radiocarbon dating. Even ultra-small samples, down to around 10 $\mu$g C, deliver meaningful information on conventional radiocarbon ages, making the technique particularly suitable for materials for which only limited sample mass is available. The low and well-characterized blank levels achieved with the system enable measurements of samples with ages of up to approximately 44 500 years.

Overall, the $CO_2$ AMS approach proves to be highly stable and extremely useful, particularly for rare or precious samples from archaeological or early historical contexts, where sample material is often limited.

# Chapter 3

# Radiocarbon dating of tree rings

The results presented in the previous chapter demonstrate that the COMORI setup enables reliable radiocarbon analysis of microgram-scale $CO_2$ samples, combining improved blank, high-precision $\delta^{13}C$ measurements, and reliable evaluation of small-sample uncertainties. On this basis, the COMORI system can now be applied to specific research questions that require the analysis of small amounts of carbon.

One such application addressed in this thesis is the measurement of tree rings for age determination. While AMS measurements are commonly performed on graphite targets because they generally provide lower uncertainties but need more sample material (<3 mg), direct $CO_2$ measurements offer an important alternative when insufficient sample material is available for graphitization, such as the rare and poorly preserved pine trees investigated here.

This chapter examines the application of $CO_2$-based AMS to dendrochronological material in two stages. It begins with a proof-of-concept study on dendrochronologically dated oak tree rings to evaluate whether $CO_2$ measurements produce reliable radiocarbon ages consistent with the independently determined ages by dendrochronology. It then extends the method to Late Glacial pine trunks from Schloss Neuhaus in Paderborn, where radiocarbon dating is used to constrain the chronology of a rare wood assemblage that cannot be securely dated by dendrochronology alone. Because these samples are rare and poorly preserved, only limited material is available for dating, making direct $CO_2$ AMS measurements the preferred approach.

## 3.1 Theoretical basis of dendrochronology

Dendrochronology is based on the analysis of variations in tree-ring width and the construction of chronologies by cross-dating overlapping ring patterns against absolutely dated reference sequences [85]. Further details on dendrochronology are given in this chapter.

The term dendrochronology derives from the Greek words *dendron* (tree) and *chronos* (time) and refers to the study of annual growth through tree rings. These dendrochronologies form part of the basis of the calibration curve discussed in Chap. 2.2.

Trees assimilate atmospheric $CO_2$ through photosynthesis and thereby incorporate $^{14}C$ into their biomass. In regions with pronounced seasonality, trees form distinct annual growth rings on the outside of the trunk. Each ring is characteristic of the year in which it formed and preserves the atmospheric $^{14}$R present during that growing season. In addition to recording atmospheric radiocarbon, tree rings also archive environmental information related to climate and weather conditions, for example by $\delta^{13}$C and $\delta^{18}$O [86].

Dendrochronology is based on the measurement and cross-dating of annual ring widths in order to establish tree-ring chronologies. The ring-width sequence of a single tree can be matched to overlapping sequences from other trees, allowing the construction of continuous chronologies. If the calendar year of felling, or of formation of the outermost ring, is known for at least one tree, absolute calendar ages can be assigned to all rings within the matched sequence. An example is shown in Fig. 3.1. By cross-dating successively older overlapping tree-ring series, continuous chronologies have been extended back to approximately 14 000 years BP.

In European chronologies, oak (*Quercus* sp.) is used most extensively and covers almost the entire Holocene, up to approximately 10 000 calBP [88]. Not all tree species are equally suitable for dendrochronological dating. Suitable trees must have distinct growth rings, a wide ecological and geographical distribution, and commonly grow in positions so that their growth reflects regional climatic signals. In addition, their heartwood must be sufficiently durable to ensure long-term preservation, and the wood must have been widely used over extended periods. European oak fulfills these criteria particularly well. Owing to its durable heartwood and favorable mechanical properties, oak has been extensively used since prehistoric times [89].

However, the oak chronology terminates for climatic reasons. The Late Glacial period (ca. 14 450–11 500 calBP) was characterized by rapid and pronounced climatic fluctuations. During this interval, Northern Europe transitioned from final

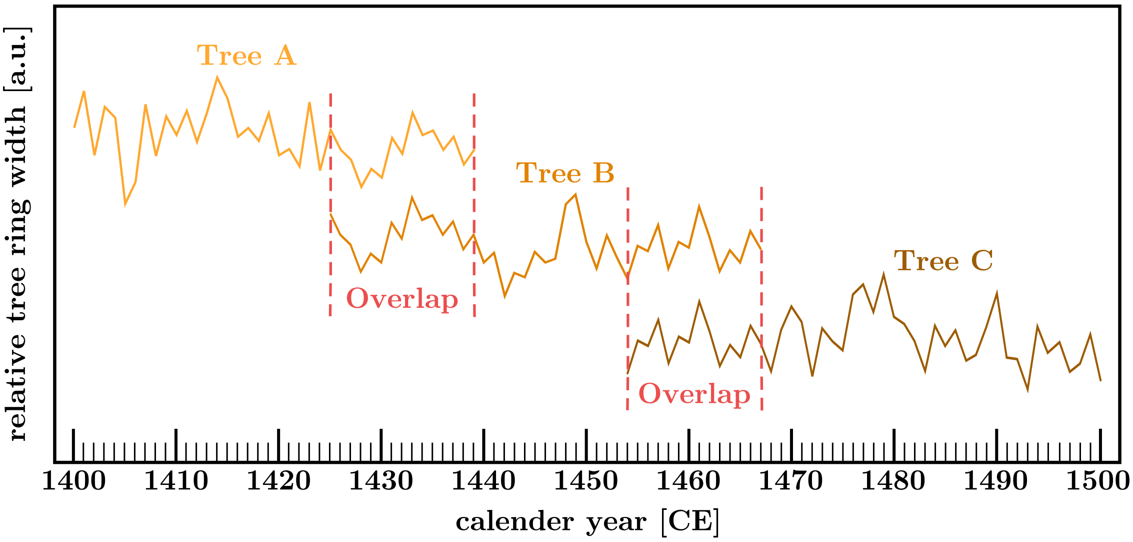

Figure 3.1: Schematic example of a sequential dendrochronology from three trees. The variations in relative tree-ring thickness are plotted against growth year. Matching patterns between different trees can then be overlapped to extend the chronology and establish a database of $^{14}$R values corresponding to calendar years. This figure was adapted from [87].

glacial conditions into the warmer Holocene climate following the retreat of extensive ice sheets [90]. Pine trees were among the first to colonize this changing landscape because of their high tolerance for cold conditions and dry, nutrient-poor soils [91]. As the climate became warmer, other tree species such as oak became more widespread. For this reason, between 10 000 and 14 000 calBP, pine plays a crucial role in bridging the final gap between radiocarbon-dated non-tree archives and the oak dendrochronology at the end of the Late Glacial period [92].

## 3.2 II Manuscript: Tree ring measurement with a $CO_2$ AMS system and its application to dating of pine trees from the last glacial period

With $CO_2$ as a reliable method to determine the ages of tree rings, the following study on Late Glacial pine is presented.

The following manuscript is the result of a collaboration between the Institute for Nuclear Physics at the University of Cologne, the Department of Prehistoric Archaeology and the Dendro Archaeology Laboratory at the University of Cologne, the Institute of Geology and Mineralogy, and the Curt-Engelhorn-Zentrum Archäometrie (CEZA) in Mannheim.

Within this collaboration, the Dendro Archaeology Laboratory carried out the dendrochronological analyses and provided the tree-ring samples. Radiocarbon measurements were performed using two different approaches: $CO_2$ measurements were conducted at the 6 MV AMS system in Cologne, while graphite targets were chemically prepared and measured at CEZA in Mannheim.

The manuscript was written for this work, with the exception of Chapter 3.2.3, which was originally provided in German by Thorsten Westphal (Dendro Archaeology Laboratory, University of Cologne) and translated for inclusion in this manuscript.

Chemical pretreatment of the oak samples was carried out at the Institute of Geology and Mineralogy (University of Cologne) in the group of Prof. Dr. J. Rethemeyer, with the assistance of Nora Benz as part of her Master's thesis.

# II Manuscript:
# Tree ring measurement with a $CO_2$ AMS system and its application to dating of pine trees from the last glacial period

**Martina Gwozdz**[1], Thorsten Westphal[2], Stefan Heinze[1], Nora Benz[1], Markus Schiffer[1,3], Dennis Mücher[1]

[1]University of Cologne, Institute for Nuclear Physics, Zuelpicher Str. 77, Cologne, 50937, Germany
[2]University of Cologne, Dendro Archaeology Laboratory, Institute of Prehistoric Archaeology, Unnauer Weg 7A, Cologne, 50767, Germany
[3]University of Cologne, Laboratory of Isotope Archaeology, Institute of Prehistoric Archaeology, Bernhard-Feilchenfeld-Str. 11, Cologne, 50969, Germany

# Abstract

This study first evaluates direct AMS radiocarbon measurements of tree rings analyzed as $CO_2$ using oak samples of independently established dendrochronological age. The insights gained from this validation are then applied to Late Glacial pine material, which represents a rare and chronologically important wood archive. The validation measurements of oak were modelled in OxCal. The $CO_2$ data yielded good overall agreement ($A_{comb} = 95.9$), and application of a `D_Sequence` model reduced the calibrated age uncertainties to ± 31 years. The graphite measurements produced modelled uncertainties of ± 13 years and a strong agreement index ($A_{comb} = 125.8$). For the Late Glacial pine material, the University of Cologne (UzK) $CO_2$ measurements placed the samples in the same age range as the Curt-Engelhorn-Zentrum Archäometrie (CEZA) graphite measurements. Comparison of weighted mean $CO_2$ ages with the corresponding graphite ages showed agreement within 1 or 2 $\sigma$ for part of the dataset, indicating that the $CO_2$ measurements provide reliable first-order age estimates but limited precision for detailed chronological interpretation. The graphite-based OxCal models yielded the most robust chronology and place the dated tree groups within the Late Glacial, mostly between about 13 400 calBP and 13 000 calBP. Overall, the results might indicate that the Paderborn wood assemblage represents several temporally distinct phases rather than a single depositional event.

## 3.2.1 Introduction

Radiocarbon dating by Accelerator Mass Spectrometry (AMS) is most commonly performed on graphite targets and has become a standard method for determining the age of organic material [92, 93].

AMS measurement with $CO_2$ becomes particularly relevant when only small amounts of sample material are available and graphitization would consume too much of the sample. This is especially important for valuable or highly limited materials, such as individual tree rings or rare wood findings. Under such conditions, direct $CO_2$ analysis represents an alternative, provided that it yields radiocarbon ages consistent with those obtained by conventional graphite preparation.

The present study investigates the feasibility of dating tree rings as $CO_2$ and compares the results with conventional graphite measurements at the 6 MV AMS system in Cologne. For this purpose, oak tree rings with an independently established dendrochronological age of approximately 1 400 calBP were selected as validation material. The use of oak with a known-age allows a direct assessment of the accuracy of the $CO_2$-based AMS approach.

Following this validation, the method is applied to Late Glacial (ca. 14 450-–11 500 calBP) pine material. Pines were among the first tree species to establish themselves in Northern Europe during the transition from glacial to interglacial conditions. As a result, such finds are rare, yet they are of particular importance as they represent a possibility for extending Late Glacial chronologies in Northern Europe.

### 3.2.2 Validation of $^{14}CO_2$ measurements using oak tree rings dated by dendrochronology

The oak wood was provided by the Dendro Archaeology Laboratory, Institute of Prehistoric Archaeology, University of Cologne. It originates from archaeological excavations carried out in 2011 at Rübenstraße in Jülich (Kreis Düren, Germany). The excavation was conducted by the firm *Goldschmidt Archäologie & Denkmalpflege*, where the find was registered under the internal designation Ordnungsnummer 3422. The recovered timber fragment, labeled k000512 by the Dendro Archaeology Laboratory, was identified as oak and formed part of a historical pile construction.

Based on tree-ring cross-dating, the wood was assigned to the period from 1 453 calBP to 1 397 calBP. Owing to its excellent state of preservation, the annual rings could be identified clearly. An image of the sample is shown in Fig. 3.2.

#### Sample preparation and measurement setup for a proof-of-concept study on oak

For radiocarbon analysis, individual tree rings were carefully separated from the oak sample. Chemical pretreatment to extract $\alpha$-cellulose was carried out at the Institute of Geology and Mineralogy of the University of Cologne. The samples were pretreated following the protocol described by Rethemeyer et al. (2013) [63]. The tree rings measured in this work with their ages in calBP (calibrated before 1950) determined by dendrochronology are:

- ring 6 - 1 448 calBP
- ring 16 - 1 438 calBP
- ring 24 - 1 430 calBP
- ring 33 - 1 421 calBP
- ring 47 - 1 407 calBP
- ring 55 - 1 399 calBP.

For each tree ring, three replicate $CO_2$ samples were prepared and measured. In parallel, the same tree rings were also converted to graphite and measured with the graphite ion source, with one graphite target prepared per ring. In addition, blank samples and Ox-II standards were prepared for both the $CO_2$ and graphite methods and measured alongside the tree-ring samples.

The masses for the graphite targets are between 990 and 1000 $\mu$g C, while the $CO_2$ samples masses measured are between 70 and 180 $\mu$g C.

After pretreatment, the samples for the $CO_2$ measurement was done with COMORI and the 6 MV AMS system of CologneAMS (Chap. 2.4.1). Each selected ring was combusted to $CO_2$ in an EA, and the resulting gas was introduced directly with a GIS into the second ion source SO-110 B [51].

Figure 3.2: Photo of the oak piece (K000512) dated by dendrochronology by T. Westphal (Dendro Archaeology Laboratory, Institute of Prehistoric Archaeology, University of Cologne). Every ring from 1 453 BP (inner ring, left side) to 1 397 BP (outer ring, right side) can be seen. Photo by T. Westphal.

### OxCal results

Radiocarbon AMS measurements first yield an $F^{14}C$ value with an associated uncertainty. From this value, the conventional radiocarbon age is calculated (Chap. 2.2), which is then entered into OxCal and calibrated with the IntCal20 calibration curve.

In OxCal, unmodelled ages are the calibrated age distributions obtained directly from the radiocarbon measurements and the calibration curve alone. These distributions represent the calibrated likelihood. Modelled ages, in contrast, are posterior age distributions derived after incorporating additional prior information from a chronological model, such as the known spacing between tree rings. The result is a calendar-age probability distribution from which confidence intervals are derived.

When several samples from one tree-ring series are available, the `D_Sequence` model in OxCal can be used. This model is suited for wiggle-matching tree-ring series because it allows the known temporal spacing between individual measurements to be incorporated into the model. The temporal spacing is done by inserting `Gap()` commands, in which the number of rings, and therefore the number of years between two dated samples, is specified. In this way, not only are the individual radiocarbon ages calibrated, but the known temporal structure of the tree-ring sequence is also incorporated into the model.

If multiple radiocarbon measurements are available for the same sample, they can be combined in OxCal using the `R_Combine` command. This produces a single combined radiocarbon determination before calibration. At the same time, OxCal applies a chi-squared test to assess whether the individual measurements are statistically consistent with one another.

To assess how well a model fits the data in OxCal, agreement indices are used.

The index A is the individual agreement index and indicates how well a single radiocarbon determination agrees with the applied OxCal model. The agreement index A is a scaled measure of overlap between the likelihood of an individual radiocarbon determination and its posterior distribution after application of the chronological model. It is primarily used to identify samples that are inconsistent with the model, and values should generally exceed 60 %.

The index $A_{comb}$ is the combination agreement index and indicates whether several radiocarbon measurements are statistically consistent enough to be combined into a single result. Its acceptable threshold also lies at 60 %.

### Results for $CO_2$

The radiocarbon results of the $CO_2$ measurements of the selected tree rings were evaluated in OxCal using the `D_Sequence` model. The three samples per ring were combined in OxCal with the `R_Combine` command, incorporating the known dendrochronological spacing between the samples. The calibrated results are shown in Fig. 3.3 with the red crosses marking the ages of the tree rings determined by dendrochronology. The confidence ranges and the agreement index of the OxCal model are shown in Tab 3.1.

For the $CO_2$ measurements, the uncertainties of the conventional radiocarbon ages range from 59 to 63 years. The corresponding unmodelled OxCal ages show $1\sigma$

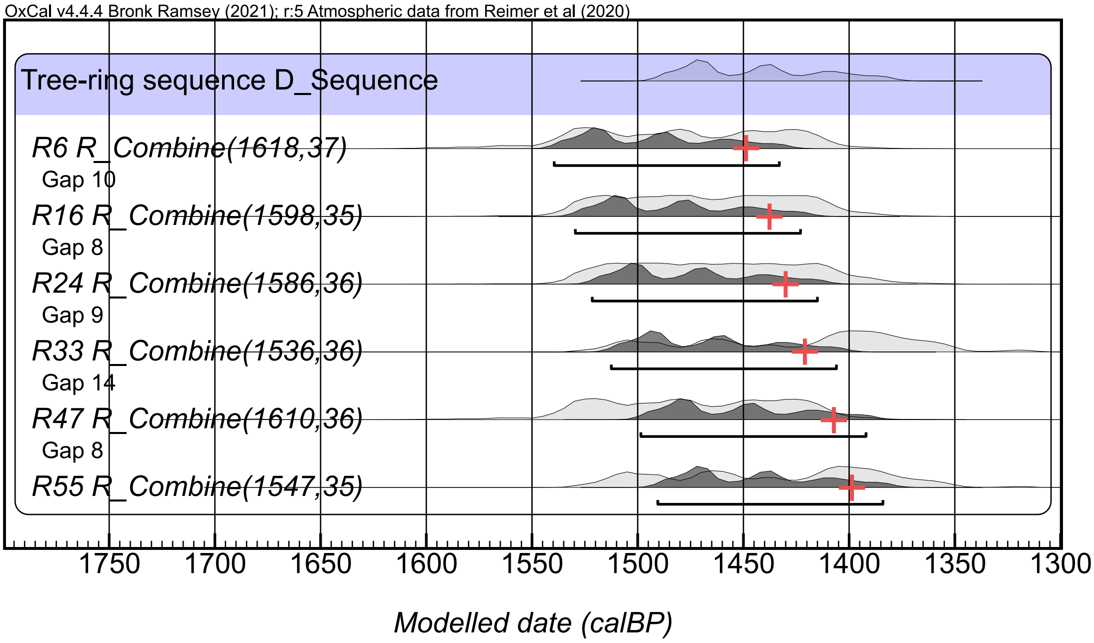

Figure 3.3: OxCal results for the $CO_2$ measurements of different tree rings. The light gray shaded areas show the unmodelled calibrated probability distributions of the individual samples (95.4 % range), while the dark gray shaded areas show the modelled posterior probability distributions obtained by applying the known temporal spacing between the tree rings (68.3 % range). The red crosses mark the dendrochronologically determined ages of the respective tree rings. The horizontal line below the distribution marks the 95.4 % highest posterior density interval of the calibrated date.

Table 3.1: OxCal results for the $CO_2$ measurement of oak tree rings.

| Ring | Dendro [BP] | Unmodelled (calBP) $\mu \pm 1\sigma$ | Unmodelled (calBP) 95.4% range | Modelled (calBP) $\mu \pm 1\sigma$ | Modelled (calBP) 95.4% range | A |
|---|---|---|---|---|---|---|
| R6 | 1448 | 1481 ± 48 | 1570–1400 | 1492 ± 31 | 1540–1433 | 109.1 |
| R16 | 1438 | 1468 ± 41 | 1538–1398 | 1482 ± 31 | 1530–1423 | 107.6 |
| R24 | 1430 | 1463 ± 41 | 1534–1389 | 1474 ± 31 | 1522–1415 | 109.7 |
| R33 | 1421 | 1424 ± 51 | 1519–1349 | 1465 ± 31 | 1513–1406 | 74.5 |
| R47 | 1407 | 1475 ± 44 | 1547–1397 | 1451 ± 31 | 1499–1392 | 98.9 |
| R55 | 1399 | 1436 ± 49 | 1520–1356 | 1443 ± 31 | 1491–1384 | 95.1 |

uncertainties between 41 and 51 years. After application of the `D_Sequence` model, the uncertainties of all individual ages are reduced to ± 31 years. The individual agreement indices range from 74.5 to 109.7, while the combined agreement index for the entire sequence is $A_{comb} = 95.9$, indicating good overall agreement between the radiocarbon data and the imposed dendrochronological sequence. As shown in Fig. 3.3, the modelled OxCal ages agree well with the dendrochronological ages marked by the red crosses, although they are systematically slightly older.

Comparison of the modelled OxCal mean ages with the dendrochronological ages shows that the OxCal ages are systematically older by 44 years. This uniform offset results from the application of the `D_Sequence` model, in which the relative spacing between the dated tree rings is fixed according to the dendrochronological information. Consequently, OxCal does not adjust each ring independently, but shifts the entire sequence as a block relative to the calibration curve. The observed offset is therefore compatible with the model structure and remains within the range expected from the approximately 10 % measurement uncertainty (Chap. 2.4.5).

### Results for graphite

For each tree ring, one graphite sample was prepared and measured to compare it to the $CO_2$ measurements. The resulting radiocarbon data were modelled in OxCal using a `D_Sequence` model that incorporates the known dendrochronological spacing between the rings. The initial model is shown in Fig. 3.4 i).

One measurement, however, showed insufficient agreement with the sequence model. Ring 33 yields an agreement index of A= 57.2, which falls below the critical threshold $A_c = 60$ required for acceptable agreement in OxCal. For this reason, ring 33 was excluded from the final model, which is shown in Fig. 3.4 ii). The confidence ranges and the agreement index of the OxCal model are shown in Tab 3.2.

For the graphite measurements, the uncertainties of the conventional radiocarbon ages lie between 38 and 39 years. The corresponding unmodelled OxCal ages show $1\sigma$ uncertainties between 30 and 52 years. After application of the `D_Sequence` model, the uncertainties of all individual ages are reduced to ± 13 years. The final `D_Sequence` model shows strong overall agreement, with $A_{comb} = 125.8$, indicating that the radiocarbon data are statistically consistent with the imposed dendrochronological sequence.

Comparison of the modelled OxCal mean ages with the independently determined dendrochronological ages shows that the graphite-based ages are systematically younger by 40 years.

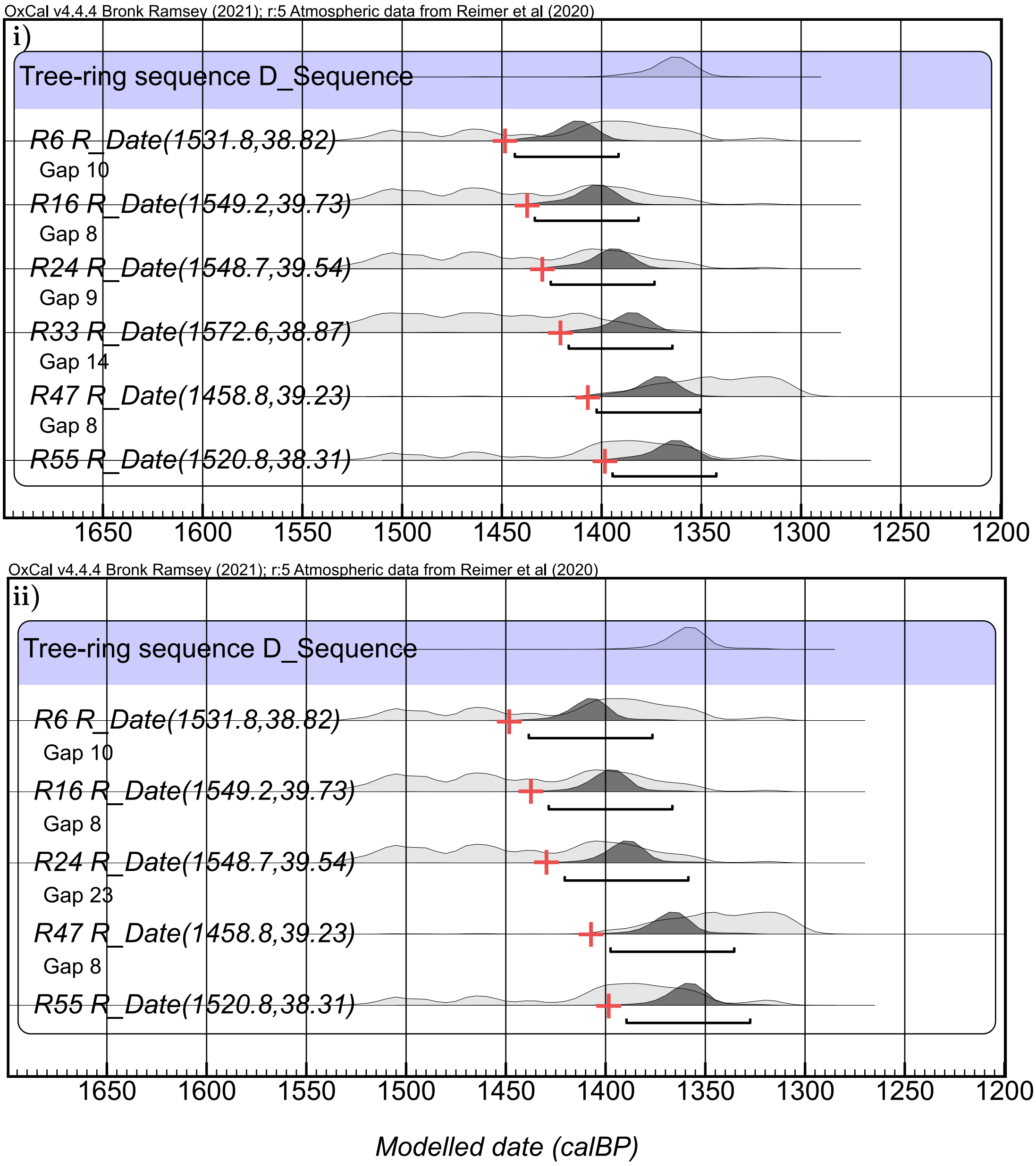

Figure 3.4: OxCal results for the graphite measurements of different tree rings.The light gray shaded areas show the unmodelled calibrated probability distributions of the individual samples (95.4 % range), while the dark gray shaded areas show the modelled posterior probability distributions obtained by applying the known temporal spacing between the tree rings (68.3 % range). i) shows the OxCal model including all six measured rings, while ii) shows the same model excluding ring 33 because of poor agreement with the sequence model. The red crosses mark the age of the tree ring dated by dendrochronology. The horizontal line below the distribution marks the 95.4 % highest posterior density interval of the calibrated date.

Table 3.2: OxCal results for the graphite measurement of oak tree rings.

| Ring | Dendro [BP] | Unmodelled (calBP) $\mu \pm 1\sigma$ | Unmodelled (calBP) 95.4% range | Modelled (calBP) $\mu \pm 1\sigma$ | Modelled (calBP) 95.4% range | A |
|---|---|---|---|---|---|---|
| R6 | 1448 | 1419 ± 52 | 1522–1345 | 1408 ± 13 | 1439–1377 | 117.2 |
| R16 | 1438 | 1438 ± 50 | 1524–1355 | 1398 ± 13 | 1429–1367 | 128.3 |
| R24 | 1430 | 1438 ± 50 | 1524–1355 | 1390 ± 13 | 1421–1359 | 119.4 |
| R47 | 1407 | 1344 ± 30 | 1398–1297 | 1367 ± 13 | 1398–1336 | 86.7 |
| R55 | 1399 | 1405 ± 51 | 1518–1312 | 1359 ± 13 | 1390–1328 | 107.3 |

### $CO_2$ vs graphite

Overall, the results demonstrate that the OxCal `D_Sequence` model yields good agreement for the $CO_2$ data, and the reduction in calibrated age uncertainties shows that the known tree-ring spacing can be used effectively to constrain the sequence. This confirms that direct $CO_2$ analysis can provide chronologically meaningful results for tree-ring material.

For the $CO_2$ measurements, the uncertainties of the conventional radiocarbon ages range from 59 to 63 years, and the unmodelled OxCal ages show $1\sigma$ uncertainties between 41 and 51 years. After application of the `D_Sequence` model, these uncertainties are reduced to ±31 years. Although the modelled $CO_2$ ages are systematically older than the dendrochronological ages by 44 years, they still overlap well with the independent age control. Because the `D_Sequence` model fixes the internal spacing of the tree-ring series, this offset reflects a shift of the sequence as a whole relative to the calibration curve rather than a mismatch in the relative spacing of the individual rings.

The graphite measurements yield a similar internal chronological pattern, but with slightly different offsets relative to the dendrochronological ages. In contrast to the $CO_2$ results, the modelled graphite ages tend to be slightly younger than the known calendar ages of the tree rings. For the graphite samples, the uncertainties of the conventional radiocarbon ages lie between 38 and 39 years, and the modelled OxCal uncertainties are reduced to ±13 years. Because these uncertainties are smaller, the resulting modelled age ranges are narrower, and the systematic offset of about 40 years becomes more clearly visible.

In total, small systematic shifts in the graphite data or $CO_2$ measurements are common. Previous measurements on the 6 MV system have shown that the corresponding $F^{14}C$ values agree with reference values within uncertainty, therefore with scatter of up to 10 % (Chap. 2.4.5), which may contribute to the observed offset. In addition, one graphite measurement, corresponding to ring 33, showed poor agreement with the sequence model and was therefore excluded. Such deviations may arise from contamination during graphitization or from statistical uncertainty in the measurement. After excluding this sample, the agreement of the graphite sequence improved substantially.

The apparently better agreement of the $CO_2$ data with the dendrochronological ages should therefore be interpreted with caution. A likely reason is the larger uncertainty of the $CO_2$ measurements, which produces broader probability distributions and thus increases the likelihood of overlap with the dendrochronological ages.

The graphite data, by contrast, provide more precise age estimates and therefore make the systematic offset more apparent.

In summary, the comparison between $CO_2$ and graphite measurements shows that direct $CO_2$ analysis of tree rings is feasible and can produce chronologically consistent results when combined with dendrochronological information. Although graphite measurements generally yield smaller uncertainties because of improved counting statistics, the $CO_2$ measurements presented here provide comparable results. This highlights the potential of direct $CO_2$ measurements for radiocarbon analysis of tree rings, particularly when only limited sample material is available or when rapid measurements are required.

### 3.2.3 Late Glacial Pine Wood

In February 2021, archaeological investigations of Late Iron Age to Early Modern sites on the grounds of the former parsonage in the Schloss Neuhaus district of Paderborn led to the discovery of 80 relatively well-preserved pine trunks (*Pinus sylvestris*) beneath the archaeological layers at a depth of approximately 3.3 m below the present surface. For geological context the trees were found beneath a sterile Late Glacial sand layer and in the absence of any indications of human activity. This suggests a date within the Allerød Interstadial and, more generally, within the Late Palaeolithic (ca. 11 400–10 700 BC) [94]. This interpretation was supported by radiocarbon dating of a pine cone at the AMS laboratory of the University of Cologne (AMS Lab ID: COL7375.1.1), which yielded an age of 11 017–10 797 calBC (95.4 % probability; S. Heinze, personal communication; see also [94]). Because the trunks contained only 59–147 rings, they could not be securely cross-dated with existing Late Glacial pine chronologies from Central Europe.

The Allerød Interstadial represents the final warm phase of the Weichselian glaciation before the onset of the Younger Dryas cold period. Rising temperatures during this time allowed the development of boreal coniferous forests on the formerly frozen tundra soils of East Westphalia.

Within an area of approximately 300 $m^2$, more than 80 pine trunks were documented, with lengths of up to 8 m and diameters of up to 0.3 m. None of the trunks showed evidence of human modification. In addition, around 1 000 preserved pine cones were recovered, all identified as *Pinus sylvestris* (Scots pine).

#### Dendrochronological classification

At similar sites, such as Uetliberg in Zürich, Switzerland (Reinig et al., 2018) [92] or Reichwalde in Saxony (Friedrich, M. et al., 2001) [93], tree stumps firmly anchored in the subsoil have been found. These indicate that the trees grew in situ before being sedimented. In Paderborn, this was not the case, suggesting that the trees discovered here were uprooted by fluvial erosion upstream, transported, and ultimately redeposited at the find site. This interpretation is also supported by occasional entanglements of crowns and root systems from different trees (see also Gai, S. et al., 2023 [94], Fig. 3.5).

In total, 107 samples were submitted to the Dendro Archaeology Laboratory at the University of Cologne for dendrochronological age determination. So far, 47 measurements have been carried out on 31 samples, representing 20 individual trees, since multiple samples were taken from some trunks. While other contemporaneous sites yielded pines several hundred years old, the material from Paderborn consists of relatively wide-ringed, and thus ring-poor, specimens. The total ring count to date ranges between 59 and 147 as the maximum measurable rings in a single sample.

The overall state of preservation is moderate. The wood is partially extremely soft and spongy and strongly water-saturated. It is also quite knotty, often in the outer sections, and in some cases strongly compressed up to the pith, resulting in associated cracking. Consequently, both the search for suitable, uncompressed radii and the preparation of measurement sections is very labor-intensive and time-consuming.

Based on the current annual ring width measurements, seven groups of contemporaneous pieces have been identified. Three samples could not be assigned to any of these groups. Comparison with various Late Glacial pine chronologies from sites in Germany, Switzerland, Poland, and the Netherlands has, so far, yielded no matches, likely due to the small number of rings. Correlation between the groups themselves could also not be established. This has led to the hypothesis that the deposition of the wood did not occur as a single event but rather in multiple phases.

Furthermore the location where the trees were found was documented and presented in Fig. 3.5. The colors mark the location of the studied groups in this work.

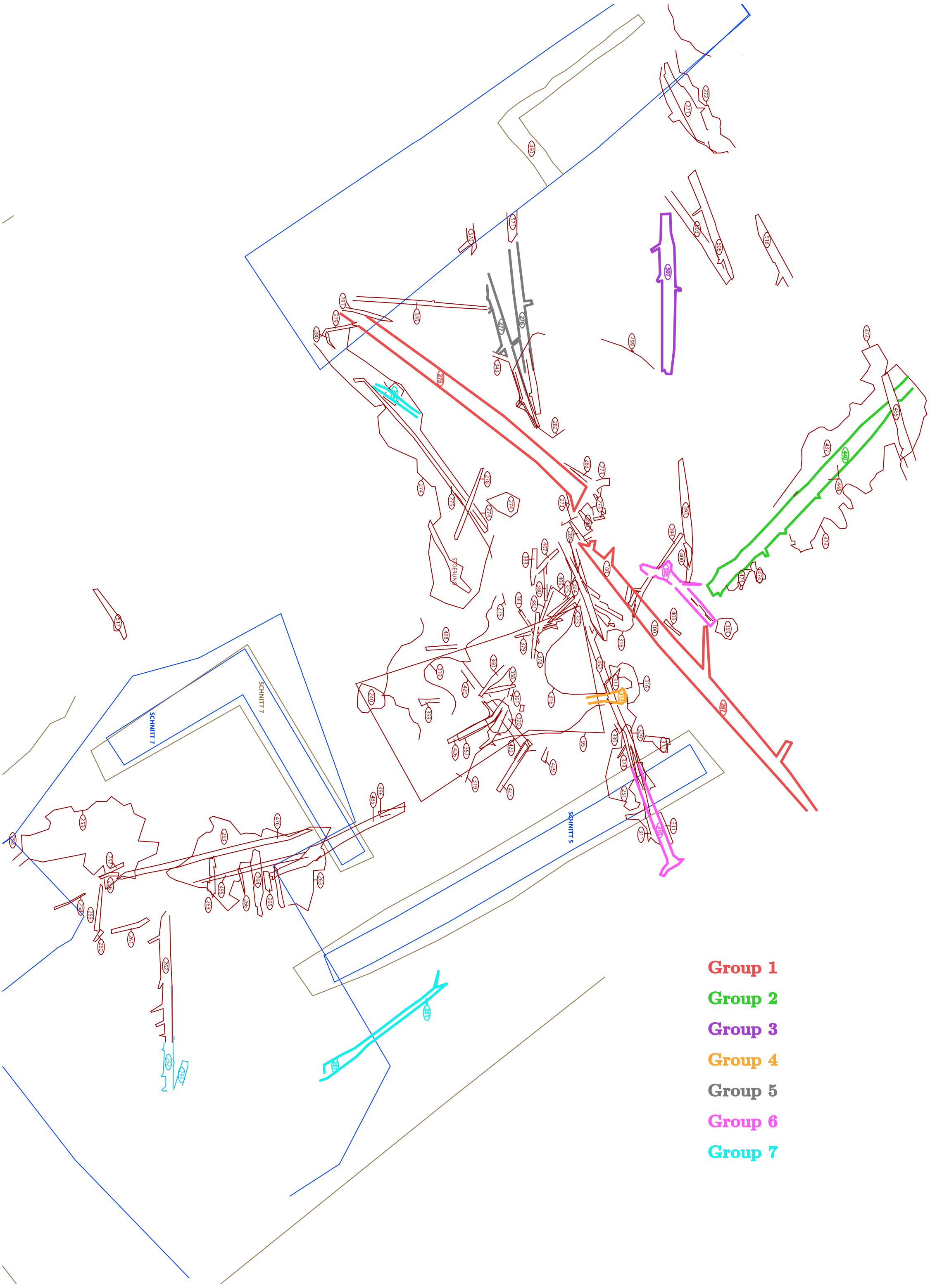

Figure 3.5: Excavation map from the archaeology excavation firm *EggensteinExca GmbH*. Marked in color are the seven dendrochronology tree groups with the outline of the trees drawn. The dark blue lines are the excavation trenches.

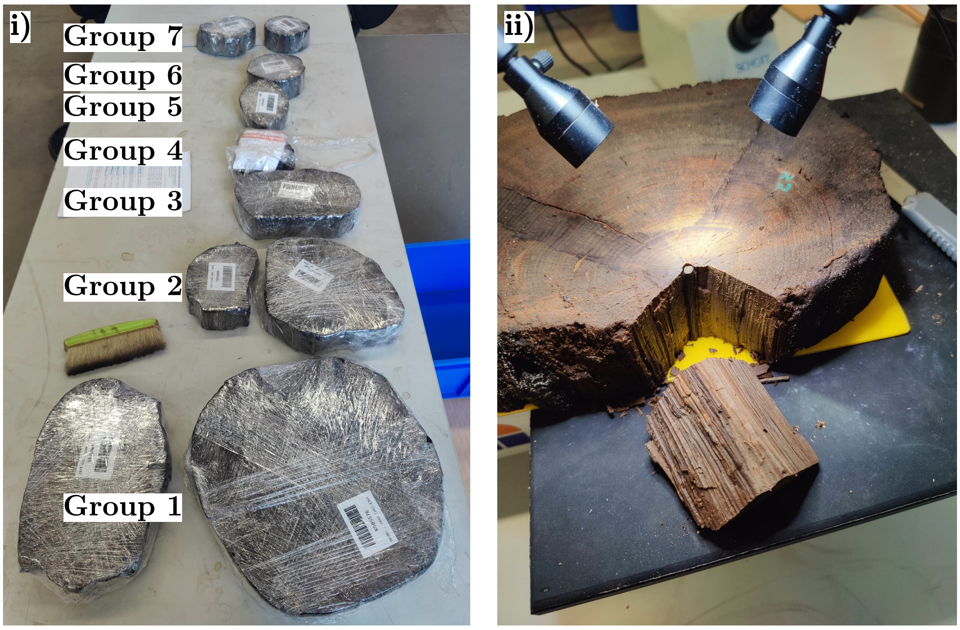

Figure 3.6: i) Picture of all seven dendrochronology pine tree groups which were analyzed for this study. The trees are cut into discs and wrapped in cling wrap to be able to store them in a freezer. Some groups consist of multiple discs from different trees, which were successfully matched with dendrochronology. ii) Example of the sampling procedure, which also illustrates the preservation state of the wood. The darker, thicker lines on the wood surface mark the sections used for dendrochronological measurements.

### Sample preparation and experimental setup

The tree ring samples for the project were prepared with the help of the Dendro Archaeology Laboratory at the University of Cologne. The trees analyzed dendrochronologically can be assigned to seven groups based on their annual ring patterns. An image of the tree discs representative of these seven groups is shown in Fig 3.6 i). Because the trees were recovered from waterlogged sediment, the wood is soft and must be stored frozen or freeze-dried to prevent deterioration.

For preparation, a few grams of the desired annual rings are removed with a scalpel from the tree discs representative of the seven groups and stored in a refrigerator until further sample processing. From each group, three annual rings were individually cut out for measurement (see graphical representation of the sampling locations with year-precise spacing within the different groups, Fig. 3.7). From each group this is the most inner ring (ring 1), then one ring from the middle of the tree rings inside the group and lastly the outer ring if possible. An example of how this process looks like can be seen in Fig. 3.6 ii). The rings that were cut out are shown in Tab. 3.3. Individual rings could not always be separated because the waterlogged wood was soft. In such cases, multiple rings were combined in one sampled when the ring boundaries were not sufficiently distinct or when the material from a single ring was insufficient for analysis.

To measure $^{14}C$ the tree needs to be chemically prepared to extract the alpha-cellulose. These steps were done with the help of the CEZA in Mannheim. The

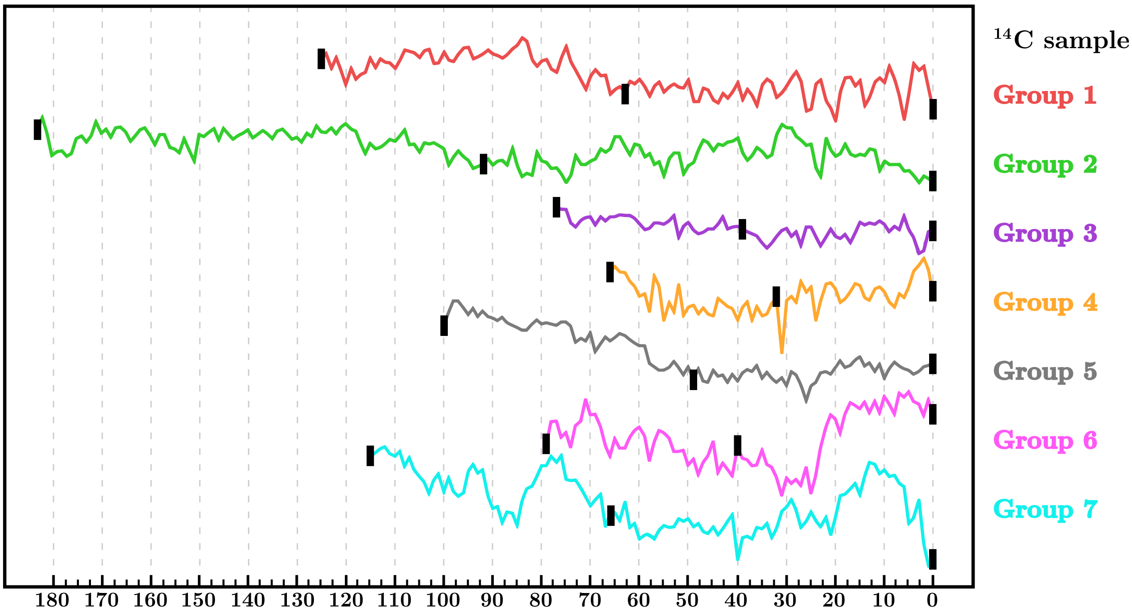

Figure 3.7: Dendrochronological ring-width series of the seven groups, shown in different colors. The black rectangles mark the rings selected for $^{14}$C sampling. Adapted from T. Westphal, Dendro Archaeology Archive, University of Cologne.

routine concludes the following steps:

- HCl (1.5 M), 80°C, 20 minutes
- Rinse twice with demineralized water
- NaOH (17.5 % w/vol), room temperature, 60 minutes
- Rinse twice with demineralized water
- HCL (1.5 M), 80°C, 20 minutes
- $NAClO_2$ (1.5 % w/vol in HCL (0.06 M)), 80°C, 16 hours
- Refresh $NAClO_2$ (1.5 % w/vol in HCL (0.06 M)), 80°C, 4 hours
- Rinse three times

These steps follow the publication of Dee et al. [95].

After a drying period a part of the samples are weighed into cleaned tin boats to be measured as $CO_2$ with the COMORI and the 6 MV AMS system of CologneAMS. Each ring was measured one to three times as $CO_2$ and, where enough sample material was available, once as graphite, as listed in Tab. 3.3. For the $CO_2$ measurements, three replicate samples were initially prepared for each ring. During the measurement process, however, several samples were lost. One $CO_2$ sample was lost for Group 1, ring 1; two for Group 1, ring 124; and one each for Group 3, ring 39; Group 5, ring 1; Group 5, rings 98–101; Group 6, ring 1; and Group 7, rings 114–116. For the $CO_2$ measurements, three replicate samples were initially prepared for each ring. During the measurement, some samples were lost because the GIS software experienced technical interruptions and had to be restarted.

Table 3.3: Conventional radiocarbon ages and their uncertainties of the Late Glacial pine tree-ring samples measured as $CO_2$ at the University of Cologne (UzK) and as graphite at CEZA Mannheim. For the $CO_2$ measurements, all available replicate measurements are listed individually. In cases where single annual rings could not be separated reliably because of poor preservation or very narrow ring widths, combined samples comprising multiple rings were measured.

| | | $CO_2$ (UzK) | | Graphite (CEZA) | |
|---|---|---|---|---|---|
| Group | Ring(s) | Conv. $^{14}$C age (yr BP) | ± | Conv. $^{14}$C age (yr BP) | ± |
| 1 | 1 | 11 374.8 | 102.6 | 11 508 | 26 |
| | | 10 910.1 | 109.2 | | |
| 1 | 63 | 11 050.1 | 97.3 | | |
| | | 11 352.4 | 99.2 | | |
| | | 11 288.0 | 90.4 | | |
| 1 | 126 | 10 734.6 | 146.9 | 11 491 | 27 |
| 2 | 1 | 11 318.5 | 186.6 | 11 479 | 26 |
| | | 11 277.6 | 115.6 | | |
| | | 10 781.6 | 99.8 | | |
| 2 | 92 | 11 170.6 | 99.8 | 11 357 | 28 |
| | | 10 686.3 | 100.4 | | |
| | | 11 101.7 | 94.5 | | |
| 2 | 177 | 10 689.3 | 93.8 | | |
| | | 10 738.1 | 107.3 | | |
| | | 10 935.4 | 108.9 | | |
| 3 | 1 | 11 267.0 | 91.9 | 11 260 | 25 |
| | | 10 999.1 | 101.6 | | |
| | | 11 071.0 | 94.2 | | |
| 3 | 39 | 11 248.6 | 133.7 | | |
| | | 11 366.9 | 129.2 | | |
| 3 | 78 | 11 021.4 | 124.6 | 11 031 | 25 |
| | | 11 219.3 | 121.8 | | |
| | | 11 092.2 | 117.9 | | |
| 4 | 1 | 11 703.7 | 159.9 | | |
| | | 11 982.1 | 133.8 | | |
| | | 11 443.6 | 162.4 | | |
| 4 | 34-35 | 11 525.2 | 128.5 | 11 533 | 26 |
| | | 11 709.1 | 246.3 | | |
| | | 11 231.2 | 126.8 | | |
| 4 | 66-67 | 11 290.4 | 178.2 | | |
| | | 11 205.0 | 179.4 | | |
| | | 11 197.7 | 177.5 | | |
| 5 | 1 | 10 945.7 | 179.9 | 11 282 | 26 |
| | | 11 040.8 | 182.5 | | |
| 5 | 51-53 | 11 368.9 | 182 | 11 355 | 26 |
| | | 11 345.3 | 177.3 | | |
| | | 11 442.9 | 178.3 | | |
| 5 | 98-101 | 10 450.7 | 183.9 | | |
| | | 10 975.4 | 177.2 | | |
| | | 10 894.7 | 184.1 | | |
| 6 | 1 | 11 652.9 | 186.5 | | |
| | | 11 368.4 | 191.2 | | |
| 6 | 40-41 | 11 577.0 | 185.6 | 11 535 | 26 |
| | | 11 584.6 | 184.4 | | |
| | | 11 636.8 | 185.7 | | |
| 6 | 80 | 11 325.9 | 183.3 | | |
| | | 11 330.4 | 182.1 | | |
| | | 11 384.3 | 187.4 | | |
| 7 | 1 | 10 661.4 | 175.1 | | |
| | | 10 864.3 | 168.5 | | |
| | | 10 353.8 | 183.3 | | |
| 7 | 66 | 10 738.8 | 175.6 | 11 075 | 25 |
| | | 10 914.6 | 172.4 | | |
| | | 11 195.1 | 179.3 | | |
| 7 | 114-116 | 11 525.2 | 187.2 | 11 495 | 26 |
| | | 11 555.1 | 188 | | |

These losses reduced the number of successful $CO_2$ measurements for several ring samples (Tab. 3.3). The affected samples are distributed across different groups and ring positions. Additionally to the samples, several Blanks, also chemically processed alongside the tree samples, as well as Ox-II is weighed into tin boats.

Another part of the samples underwent graphitization and was measured at CEZA with a MICADAS system. At least one ring from each group is measured at CEZA.

### Results

The calculated conventional radiocarbon ages of the graphite and $CO_2$ samples are shown in Tab. 3.3. The conventional radiocarbon age uncertainties obtained for the UzK $CO_2$ measurements are substantially larger than those of the CEZA graphite measurements. For the UzK data, the uncertainties range from 90.4 to 246.3 years, with most values lying between about 100 and 190 years. In contrast, the CEZA graphite measurements show much smaller and more uniform uncertainties of 25 to 28 years. Thus, the CEZA ages are consistently more precise than the UzK ages.

Compared with the oak tree-ring measurements discussed above, the uncertainties of the present UzK $CO_2$ dataset are larger than those obtained for the oak $CO_2$ measurements (59–63 years), whereas the CEZA graphite uncertainties are even smaller than those observed for the oak graphite measurements (38–39 years). Graphitization generally yields lower uncertainties because comparatively large amounts of carbon can be measured, approximately 1 000 $\mu$g C for graphite compared with about 100 $\mu$g C for $CO_2$ measurements. This results in higher count rates and improved counting statistics. The comparatively low $^{14}C$ count numbers obtained for the pine samples, are only about 6 000–10 000 counts, compared with 23 000–28 000 counts for the younger oak samples. Since counting uncertainty scales approximately with $1/\sqrt{N}$, these lower count numbers result in larger statistical fluctuations and hence larger measurement uncertainties.

In addition, the oak samples measured above have ages of around 1 400 calBP, whereas the pine samples are about 12 000 years older. Since this age difference corresponds to more than two half-lives of $^{14}C$, the remaining $^{14}C$ content is reduced to less than one quarter of the original amount, which further decreases counting statistics.

For a first-order estimate based on counting statistics alone, a $CO_2$ sample of 100 $\mu$g C yielding about 7 000 $^{14}C$ counts would correspond to a relative statistical uncertainty of approximately 1.2 %, which for an age of about 11 000 years, translates to an uncertainty of about ± 132 years. By contrast, a graphite sample of 1 000 $\mu$g C yielding about 70 000 counts would correspond to a relative uncertainty of about 0.4 %, equivalent to ± 44 years at the same age. The observed UzK uncertainties are of the same order, whereas the CEZA graphite uncertainties are even smaller. Overall, the comparison confirms that the much higher count numbers obtained from the larger graphite samples lead to improved age precision relative to the direct $CO_2$ measurements.

To improve the counting statistics, the $CO_2$ samples size must be larger. A first-order estimate of the sample size required for older $CO_2$ samples can be obtained by assuming that the number of detected $^{14}C$ counts scales with both carbon mass

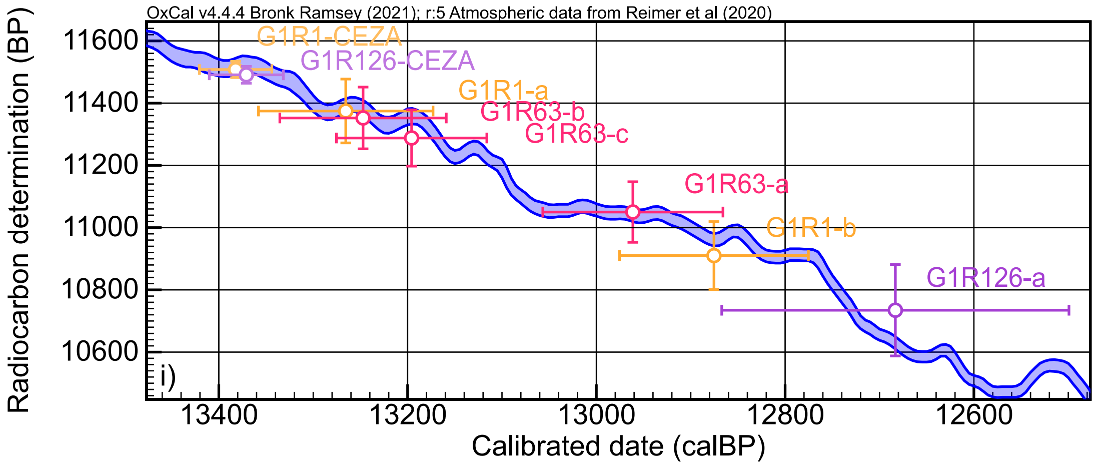

Figure 3.8: Individual OxCal calibrations of the $^{14}$C measurements from the sampled tree rings. Samples labeled 'CEZA' were measured at CEZA in Mannheim, while indices a, b, and c denote measurements performed in Cologne. Yellow corresponds to samples from Group 1, ring 1; pink represents samples from Group 1, ring 63; and purple represent samples from Group 1, ring 126.

and the remaining $^{14}$C abundance. Using the observed pine measurements as a reference, a sample of about 50 $\mu$g C yielded only about 6 000–10 000 counts. To reach count numbers comparable to those obtained for the younger oak samples (about 25 000 counts), the required carbon mass lies between about 125 and 210 $\mu$g C for the observed pine count range. Thus, a practical estimate is that Late Glacial pine samples would need roughly 150–200 $\mu$g C to approach the counting statistics, achieved for the younger oak samples.

In order to assess an approximate calendar age ranges the $CO_2$ and graphite measurement with samples from group 1, calibrated in OxCal without applying a model are shown in Fig. 3.8. The UzK $CO_2$ measurements place the samples within the same Late Glacial age range as the CEZA graphite measurements. However, the uncertainties of the UzK data remain substantially larger, which limits the chronological resolution that can be achieved from the $CO_2$ data alone. To assess the agreement between the UzK $CO_2$ measurements and the corresponding CEZA graphite ages, an inverse-variance weighted mean was calculated for each set of UzK replicate measurements. In this approach, individual measurements with smaller uncertainties contribute more strongly to the mean than measurements with larger uncertainties. The weighted mean age, $\bar{t}_{\mathrm{UzK}}$, was calculated from the individual UzK radiocarbon ages $t_i$ and their associated uncertainties $\sigma_i$, where $i$ denotes the individual replicate and $n$ the total number of UzK replicates for a given sample. Here, $\sigma_i$ represents the uncertainty obtained from error propagation of an individual radiocarbon age derived from the analytical error calculation. The weighted mean is given by

$$\bar{t}_{\mathrm{UzK}} = \frac{\sum_{i=1}^{n} \frac{t_i}{\sigma_i^2}}{\sum_{i=1}^{n} \frac{1}{\sigma_i^2}} \qquad \text{with} \qquad \sigma_{\bar{t}} = \left( \sum_{i=1}^{n} \frac{1}{\sigma_i^2} \right)^{-1/2} . \tag{3.1}$$

The uncertainty of the weighted mean is denoted by $\sigma_{\bar{t}}$. The difference between both laboratories was then expressed as $\Delta t$, defined as the CEZA graphite age $t_{\mathrm{CEZA}}$ minus the weighted mean UzK age $\bar{t}_{\mathrm{UzK}}$. To evaluate the significance of this difference, a standardized difference $z$ was calculated by dividing $\Delta t$ by the combined uncertainty of both values, where $\sigma_{\mathrm{CEZA}}$ is the uncertainty of the graphite measurement as given by CEZA:

$$z = \frac{\Delta t}{\sqrt{\sigma_{\bar{t}}^2 + \sigma_{\mathrm{CEZA}}^2}} \qquad \text{with} \qquad \Delta t = t_{\mathrm{CEZA}} - \bar{t}_{\mathrm{UzK}}. \tag{3.2}$$

The results of this comparison are listed in Tab. 3.4 and show that the two datasets do not agree consistently. Three samples (groups 5, 6, and 7 for rings 51–53, 40–41, and 114–116, respectively) agree within $1\sigma$, while a further three samples (groups 3, 4, and 7 for rings 78, 34–35, and 66, respectively) agree within $2\sigma$. In the remaining cases, the differences between the UzK and CEZA ages exceed the combined uncertainties. A likely reason is the comparatively large scatter among the UzK $CO_2$ replicate measurements, which in some cases reaches about 10 % and is typical for samples of this size and age. The precision of the UzK results could probably be improved by measuring a larger fraction of the available sample material and thereby increasing the $^{14}C$ count statistics. In several cases, the lack of agreement may also reflect the limited number of $CO_2$ measurements available for a given ring. The fact that only one or two replicates were available for some sample groups was due to the loss of several measurements caused by technical difficulties in the setup. For example, G1R126 is based on only a single $CO_2$ measurement, while G1R1 and group 5 ring 1 are represented by only two measurements that are widely separated in age.

In contrast, the disagreement observed for group 2 cannot be explained in the same way and remains unresolved. In addition, it cannot be excluded that the quoted uncertainties of the CEZA graphite measurements are slightly underes-

Table 3.4: Comparison of UzK $CO_2$ weighted mean ages with CEZA graphite ages. The weighted mean of the UzK replicates was calculated by inverse-variance weighting. The difference is defined in Eq. 3.1. Agreement was assessed using the standardized difference defined in Eq. 3.2.

| Group | Ring | $\bar{t}_{\mathrm{UzK}}$ (yr BP) | $\sigma_{\mathrm{UzK}}$ (yr) | CEZA (yr BP) | $\sigma_{\mathrm{CEZA}}$ (yr) | $\Delta t$ (yr) | $z$ | Agreement |
|---|---|---|---|---|---|---|---|---|
| 1 | 1 | 11 156.9 | 74.8 | 11 508 | 26 | +351.1 | +4.43 | no |
| 1 | 126 | 10 734.6 | 146.9 | 11 491 | 27 | +756.4 | +5.06 | no |
| 2 | 1 | 11 039.2 | 70.0 | 11 479 | 26 | +439.8 | +5.89 | no |
| 2 | 92 | 10 991.6 | 56.7 | 11 357 | 28 | +365.4 | +5.78 | no |
| 3 | 1 | 11 120.5 | 55.2 | 11 260 | 25 | +139.5 | +2.30 | no |
| 3 | 78 | 11 111.9 | 70.1 | 11 031 | 25 | -80.9 | -1.09 | within $2\sigma$ |
| 4 | 34–35 | 11 415.6 | 84.7 | 11 533 | 26 | +117.4 | +1.32 | within $2\sigma$ |
| 5 | 1 | 10 992.6 | 128.1 | 11 282 | 26 | +289.4 | +2.21 | no |
| 5 | 51–53 | 11 385.8 | 103.4 | 11 355 | 26 | -30.8 | -0.29 | within $1\sigma$ |
| 6 | 40–41 | 11 599.4 | 106.9 | 11 535 | 26 | -64.4 | -0.59 | within $1\sigma$ |
| 7 | 66 | 10 945.7 | 101.4 | 11 075 | 25 | +129.3 | +1.24 | within $2\sigma$ |
| 7 | 114–116 | 11 540.1 | 132.7 | 11 495 | 26 | -45.1 | -0.33 | within $1\sigma$ |

timated, which would also increase the apparent disagreement between the two datasets. Thus, although the UzK $CO_2$ and CEZA graphite measurements do not show agreement at the level required for detailed chronological interpretation, the $CO_2$ results nevertheless reproduce the correct broad Late Glacial age range and therefore provide a reliable first-order chronological estimate.

Although an OxCal model based on arithmetic mean conventional radiocarbon ages of both graphite and $CO_2$ can be constructed and yields a consistent sequence, the uncertainties of the combined average model remain too large to draw more specific conclusions about the chronology of the individual tree groups. For this reason, only the CEZA graphite results are considered in the following and shown in Fig. 3.9.

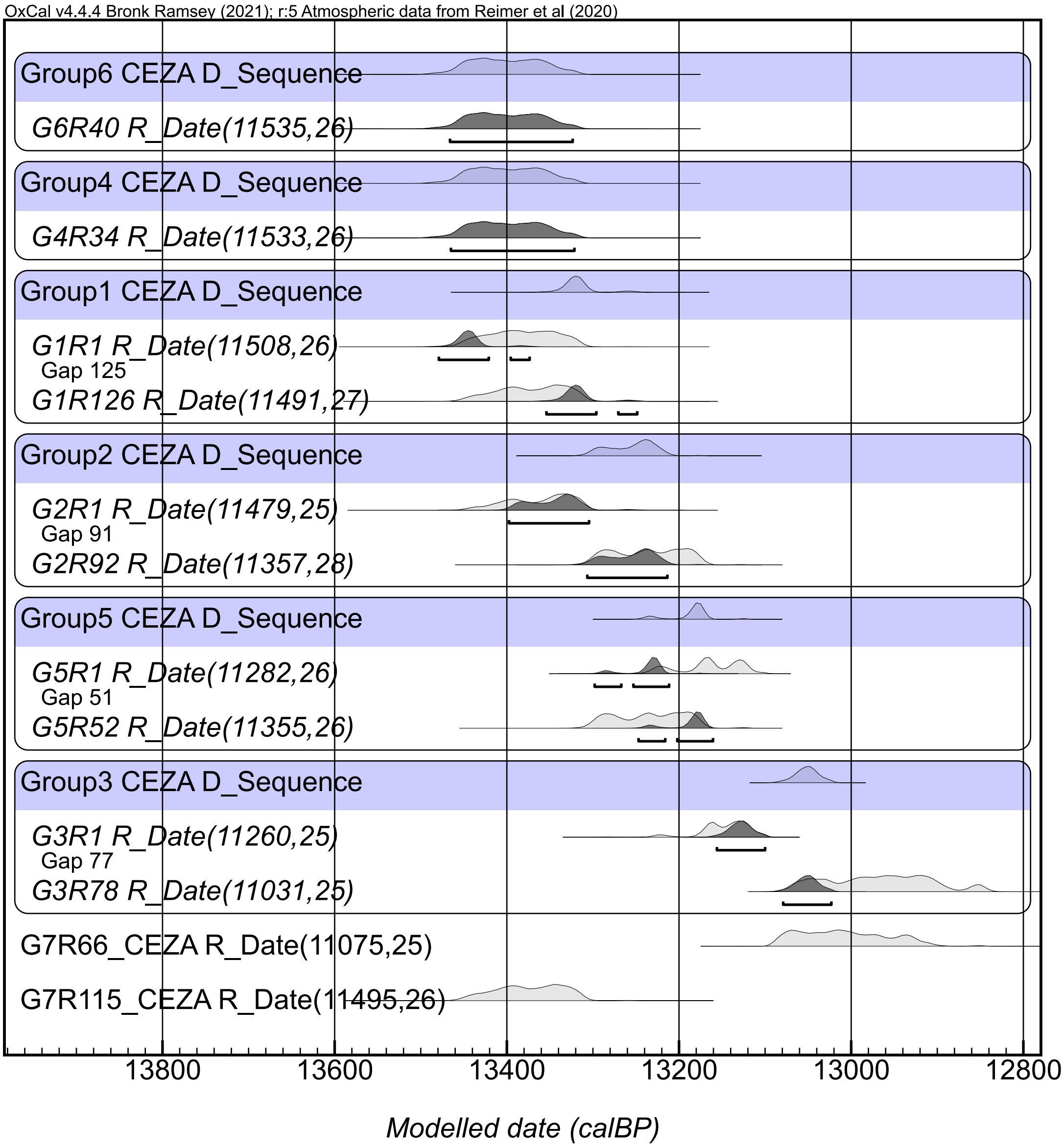

Figure 3.9: Modeled dates for the graphite measurements at CEZA. The individual groups are arranged according to the age of ring 1, with progressively younger groups plotted lower in the figure. The horizontal line below the distribution marks the 95.4 % highest posterior density interval of the calibrated date.

The CEZA graphite measurements were evaluated in OxCal using `D_Sequence` models for those groups for where more than one dated ring was available.

During the calibration in Oxcal, two cases of insufficient agreement became evident. Firstly, group 5 yields a modelled age of 13 187 ± 23 BP, but the agreement of this sequence is poor with an agreement overall of $A_{comb} = 50.8$, which is mainly caused by the low agreement of G5R1 ($A = 44.2$).

The OxCal model of group 5 therefore does not meet the formal agreement criterion. However, inspection of the data on the calibration plot, shown in Fig. 3.10 i) suggests that the samples could agree well with the calibration curve. Both determinations, G5R1 (11 282 ± 26 BP) and G5R52 (11 355 ± 26 BP), appear to fall on plausible parts of the calibration curve, and the approximately 50-year offset between them can be accommodated within this section of the curve. Visual inspection indicates that the two determinations are consistent with the local shape of the calibration curve: G5R1 falls on a lower section of the curve, whereas G5R52 falls on a higher section. Notably, the conventional radiocarbon age of ring 1 is younger than that of ring 52, although ring 1 is earlier in the tree-ring sequence. This relationship can only be explained if the samples are placed across a local decline and subsequent rise in the calibration curve. There does not appear to be an obvious alternative placement that would provide a substantially better fit. This raises the possibility that the poor agreement value is not caused by an incorrect dendrochronological position of the samples, but rather by uncertainties in the AMS measurement that are slightly underestimated.

Secondly, group 1 with a modelled age of 13 317 ± 20 BP is only marginally acceptable, with $A_{comb} = 61.1$, and one of its two measurements (G1R1) falls below the critical threshold with $A = 57.4$.

Although group 1 also yields an agreement index below the commonly accepted threshold, the calibration plot in Fig. 3.10 ii) indicates that the fit to the curve is still reasonable. The determinations G1R1 and G1R126 both fall within the same plausible segment of the calibration curve and are consistent with its local shape. Since this segment is comparatively flat, the sequence is constrained by only limited variation in radiocarbon age, which may contribute to the low formal agreement. Furthermore, the laboratory uncertainty may be slightly underestimated. Overall, the placement of group 1 on the calibration curve appears convincing by eye.

Furthermore, the two CEZA measurements from group 7 were not combined into OxCal with a `D_Sequence` because their modelled agreement was poor ($A = 0$). As can be seen in Fig. 3.9, even the unmodelled ages differ substantially, with G7R66 yielding 13 008 ± 50 BP and G7R115 yielding 13 374 ± 39 BP. This large difference indicates that the dated rings from group 7 do not form a short internally consistent sequence in the same way as the successfully modelled groups.

In the remaining cases, the resulting modelled ages produce samples and groups with good agreement indices. The oldest modelled groups are group 6 and group 4, with virtually identical ages of 13 400 ± 39 BP and 13 399 ± 39 BP, respectively. These single-dated rings each yield an $A = 100$ in OxCal.

Group 2 calculated in OxCal to 13 255 ± 27 BP, and group 3 represents the youngest successfully modelled sequence with 13 052 ± 13 BP. Group 2 and group 3 show strong agreement, with $A_{comb}$ values of 104.9 and 97.5, respectively.

Since the combined agreement index summarizes the agreement of the group as

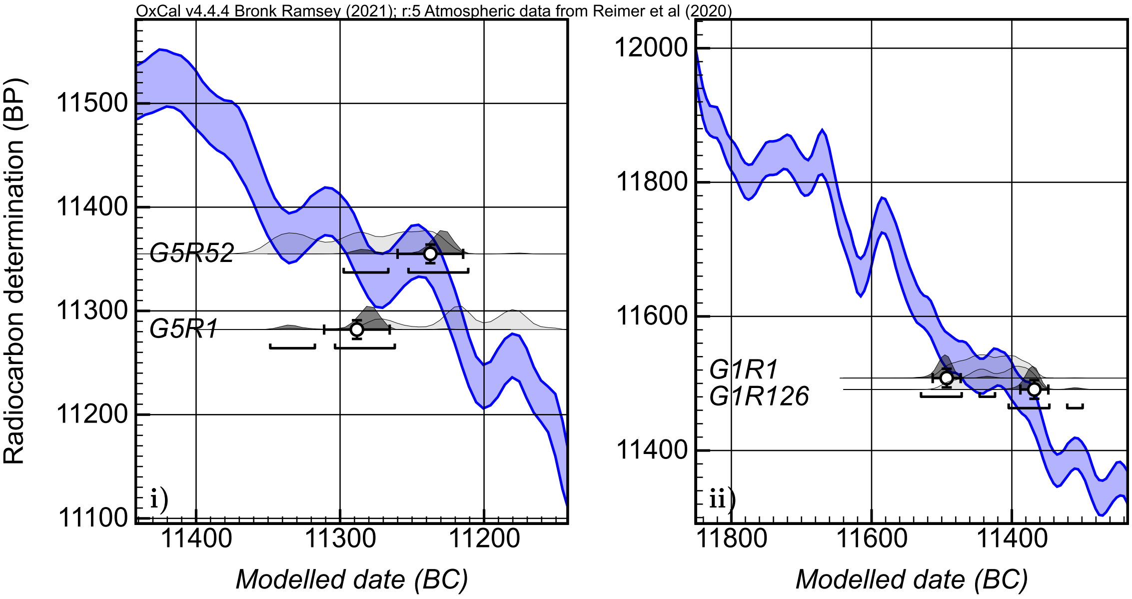

Figure 3.10: OxCal plots of the wiggle-matched samples on the calibration curve. i) shows group 5 with rings 1 and 52, and ii) shows group 1 with rings 1 and 126. The blue line represents the calibration curve. The circles indicate the posterior mean distribution of the samples on the curve, the vertical bars represent the uncertainties of the radiocarbon determinations, and the horizontal bars show the modelled calendar-age ranges (posterior distributions).

a whole, these values indicate that the internal spacing of the dated rings and their placement on the calibration curve are mutually consistent. In this respect, these groups provide strong support for the overall model.

Overall, the CEZA graphite data indicate that the sampled wood covers a time span of about 600 years, with most groups clustering between about 13 400 calBP and 13 050 calBP. As the final outcome of the graphite radiocarbon measurements, the calibration, and the modelling in Oxcal, the dated groups can be placed on a timeline. Fig. 3.11 presents this timeline by arranging the groups according to their OxCal-derived mean ages ($\mu$) and displaying their associated $\sigma$ uncertainties. While group 1 and group 5 are also included in this plot due to the convincing placement on the calibration curve, group 7 is excluded due to the poor agreement. In this way, the figure provides an overview of a possible relative sequence.

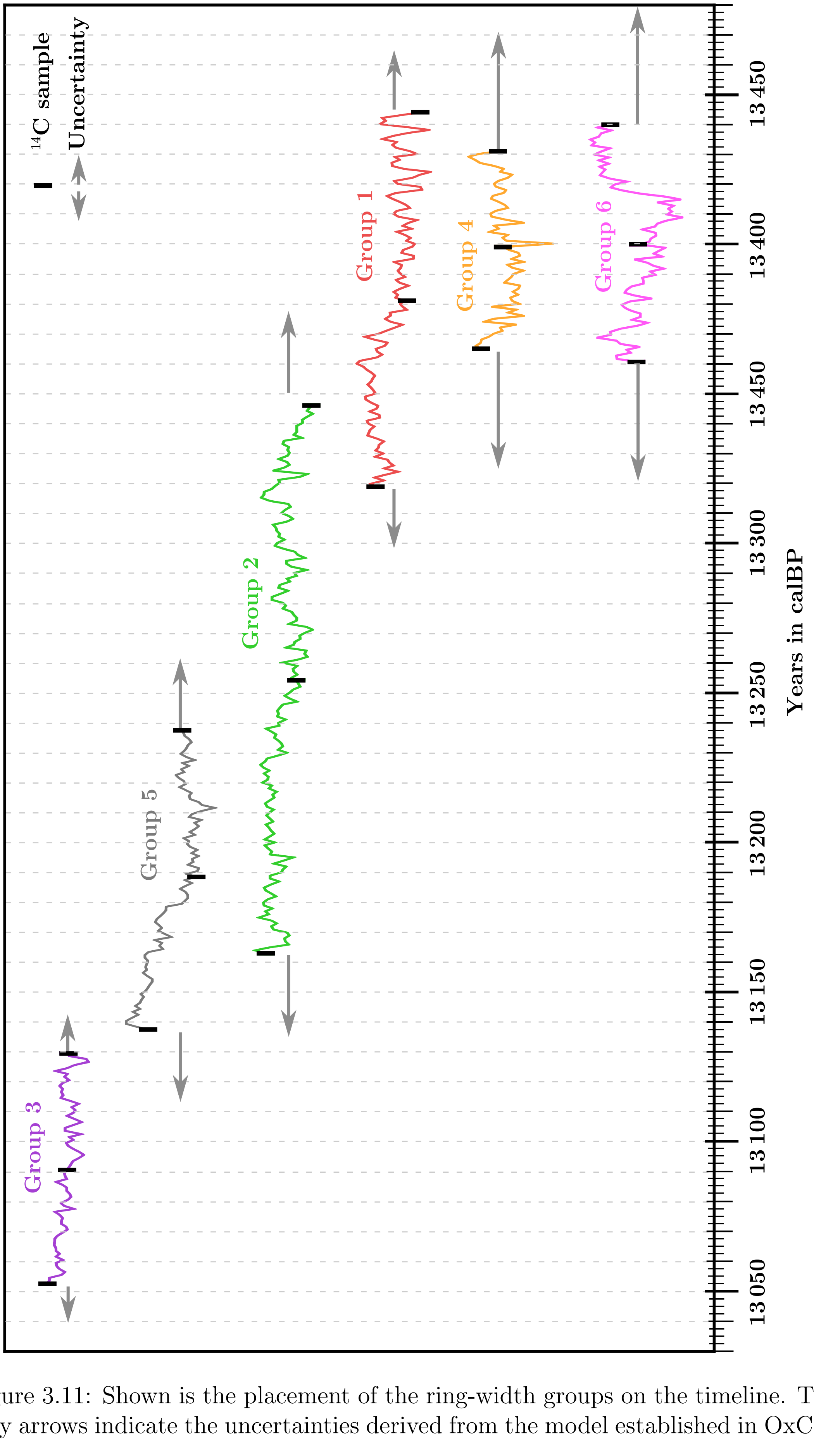

Figure 3.11: Shown is the placement of the ring-width groups on the timeline. The gray arrows indicate the uncertainties derived from the model established in OxCal.

### 3.2.4 Discussion

The modeled ages of the dendrochronologically defined groups indicate that the sampled trees span an overall time frame of approximately 600 years. Groups 6 and 4 represent the oldest trees in the dataset, with modeled mean ages of 13 400 ± 39 calBP and 13 399 ± 39 calBP, respectively. The chronological ranges of these two groups overlap, suggesting that at least part of their growth periods may have occurred simultaneously. However, the overlapping interval is limited, and the individual trees contain only relatively small numbers of annual rings (80 rings in group 6 and 67 rings in group 4). Consequently, it cannot be conclusively determined whether the trees of these groups grew during the same time period. The limited ring counts reduce the statistical strength of comparisons with existing Late Glacial dendrochronologies and may partially explain why cross-dating attempts have so far remained unsuccessful.

A similar relationship in time can be observed for groups 1 compared to groups 6 and 4. Group 1 ring 1 has a modeled mean ages of 13 442 ± 20 calBP indicating that these trees likely grew during broadly similar periods. Groups 5 and 2 are slightly younger, with modeled ages of 13 238 ± 23 calBP (ring 1) and 13 346 ± 27 calBP (ring 1). Although these modelled ages suggest a general chronology, the uncertainties associated with the radiocarbon measurements and the limited number of rings in each sample make it difficult to establish precise temporal relationships between all groups.

The spatial distribution of the groups within the excavation area provides additional insights into the depositional history of the wood. As shown in Fig. 3.5, the trunks belonging to groups 4 (yellow), 6 (pink), and 1 (red) are located in close proximity to each other. Their similar spatial position and the fact that many of the trunks lie parallel to one another may indicate that these trees were transported and deposited during the same fluvial event. Such an interpretation could be consistent with the hypothesis that the trees were uprooted upstream and subsequently transported before being redeposited at the site.

In contrast, group 2 (green) is directed away from this main cluster, while groups 3 (purple) and 5 (gray) appear more isolated within the excavation area. Nevertheless, the trunks of groups 3 and 5 show similar orientations, suggesting that they may have been deposited under comparable hydrological conditions, possibly during a separate transport event. One of the trees of group 7 (cyan), which lies considerably further from the other groups (bottom of Fig. 3.5), may represent yet another depositional phase or may have been transported from a different upstream location. The other tree sample of group 7 (upper middle of Fig. 3.5) lies considerably far away from the second piece of the group. This would support the hypothesis that the two groups do not belong to each other. But the statistical and visual comparison of the dendrochronology of the samples shows that they could belong to the same sequence.

In conclusion, the chronological and spatial patterns suggest that the wood assemblage was not deposited during a single event but rather accumulated over multiple phases. Individual transport and sedimentation events may have introduced trees of different ages from various upstream areas into the depositional environment. This interpretation would also explain the absence of clear dendrochronological correlations between the groups, despite their broadly overlapping radiocarbon ages.

An alternative explanation is that at least part of the assemblage was not transported directly to its final depositional position immediately after tree death, but was first stored and later remobilized. In such a scenario, the trunks may have accumulated temporarily upstream or in a nearby fluvial setting and were only subsequently reworked and redeposited at the excavation site during a later transport event. This possibility could also account for the mixture of different ages within the assemblage and for the absence of clear dendrochronological connections between the groups.

### 3.2.5 Conclusion

The pine trunks discovered at the Schloss Neuhaus excavation site in Paderborn represent a rare Late Glacial wood archive spanning the later part of the Allerød and possibly the onset of the Younger Dryas. Dendrochronological analysis allowed the material to be divided into seven distinct groups, but the relatively small number of annual rings per sample prevented cross-dating with established Central European Late Glacial pine chronologies. Radiocarbon measurements of selected rings, performed on both $CO_2$ and graphite targets, indicate that the dated groups span roughly 600 years, from about 13 500 calBP to 13 040 calBP.

Methodologically, the graphite results generally provide a robust input into the OxCal models for the present dataset .Most groups show acceptable internal agreement, while groups 5 and 7 remain less secure; however, their dated samples can still be placed plausibly on the calibration curve.

In contrast to Late Glacial sites with rooted or clearly in situ woodland remains, such as Reichwalde, Koźmin, and the Swiss sites [92, 96, 93], the Paderborn assemblage is best interpreted as a redeposited wood deposit. The absence of stumps anchored in the subsoil, the partial entanglement of crowns and root systems, the spatial clustering of some groups, and the differing orientations of others could support repeated fluvial transport and redeposition rather than burial of a forest that grew directly at the find spot. The Paderborn material therefore most likely represents trees eroded from one or several upstream stands and introduced to the site during multiple depositional phases, possibly including an intermediate phase of storage followed by later remobilization and redeposition.

This distinction is important for interpretation. Whereas in situ sites can be used to reconstruct local forest development and tree mortality directly, the Paderborn assemblage primarily records Late Glacial river dynamics and the reworking of pine wood from the surrounding landscape. Even so, it remains scientifically valuable: it adds new radiocarbon data for an underrepresented dendrochronological interval, enlarges the pool of available Late Glacial pine material from Central Europe, and may help to strengthen the floating dendrochronological and radiocarbon framework for the Allerød–Younger Dryas transition.

# Acknowledgment

This research was supported by the CEZA Mannheim. We would like to thank Dr. Susanne Lindauer and Dr. Ronny Friedrich for their support with the chemical preparation of the samples and for performing the measurements of the graphite samples.

## 3.3 Summary

The pine trunks discovered at the Schloss Neuhaus excavation site in Paderborn represent a rare Late Glacial wood assemblage dating to the Allerød Interstadial. More than 80 well-preserved trunks of *Pinus sylvestris* were documented during archaeological excavations. Among other reasons, the relatively small number of annual rings in the individual samples (59–147 rings), did not allow for direct cross-dating with existing Late Glacial pine chronologies from Central Europe.

Based on dendrochronological ring-width patterns, the material could be divided into seven independent groups. Radiocarbon measurements of selected tree rings were carried out using both $CO_2$ targets measured at the CologneAMS facility and graphite targets measured at CEZA Mannheim. Statistical evaluation of the results demonstrated that the arithmetic mean between the two measurement approaches generally provided the most consistent calibration results in OxCal. The modeled ages indicate that the trees span an overall time interval of roughly 600 years, ranging from approximately 13 500 calBP to 13 040 calBP.

The chronological distribution of the groups, combined with their spatial arrangement within the excavation area, could suggest that the wood assemblage was not deposited during a single event. Instead, multiple phases of fluvial transport and sedimentation likely introduced trees from different upstream locations into the depositional environment. This interpretation could be supported by the clustering of several groups with similar trunk orientations, as well as by the presence of more isolated trunks that may represent separate transport events. It could also be interpreted, that part of the material may have been accumulated elsewhere and only later remobilized and redeposited at the site.

Although the relatively small ring counts limit direct integration into existing dendrochronological chronologies, the Paderborn material nevertheless represents a valuable Late Glacial archive. The combination of dendrochronology, radiocarbon dating, and spatial analysis provides important insights into the depositional history of the site and contributes new radiocarbon data for the Allerød period. With additional sampling and further measurements, this assemblage may help to refine the chronological framework for Late Glacial pine records in Central Europe.

The results obtained from graphite and $CO_2$ measurements proved to be generally coherent, indicating that both approaches yield reliable radiocarbon ages. In particular, $CO_2$ measurements appear to be a highly useful method for small samples or for obtaining an initial estimate of the age of wood material, offering an efficient and less resource-intensive alternative to graphite preparation.

Given the large number of trunks recovered from the site, further investigation of their ages is strongly recommended. Expanding the dataset may increase the likelihood of identifying temporal overlaps between individual trees, which could enable the construction of longer, continuous chronologies and potentially bridge gaps in existing Late Glacial dendrochronological records.

Moreover, high-resolution, ring-by-ring radiocarbon measurements would represent a valuable next step. Such data are still relatively scarce but could provide significantly improved insights into short-term variations and enhance the precision of dendrochronological alignment. This approach would not only refine the age estimates of the Paderborn material but also contribute to a better understanding of

Late Glacial environmental.

# Chapter 4

# $^{14}$C AMS measurements of reactor graphite

In contrast to the old and modern samples discussed in Chap. 2 and Chap. 3, the focus of the present chapter is not on age determination but on quantifying the $^{14}$C activity in activated material. As in the previous radiocarbon applications, the samples studied here are combusted in an EA to produce $CO_2$, which is transferred to the GIS and subsequently analyzed by AMS. Building on the successful use of $^{14}CO_2$ measurements for radiocarbon analysis, this approach offers an important additional advantage for activated material: a substantial reduction in sample preparation effort. Since conventional preparation methods for activated samples are often labor-intensive, the direct measurement of $CO_2$ represents an efficient alternative for determining $^{14}$C activity.

## 4.1 Motivation

The second application addressed in this thesis concerns nuclear waste management, in particular the characterization of activated reactor graphite. Worldwide, approximately 250 000 tons of reactor graphite require quantitative characterization prior to final disposal [97]. In Germany alone, about 1 000 tons originate from the two prototype reactors AVR in Jülich and THTR-300 in Hamm-Uentrop [98].

Reactor graphite presents a major disposal challenge because neutron activation produces long-lived radionuclides such as $^{14}$C, $^{36}$Cl, and tritium, which may be released in gaseous form under repository conditions. Among these radionuclides, $^{14}$C is particularly critical, since it is chemically indistinguishable from the graphite matrix and therefore cannot be selectively separated. In addition, the regulatory requirements for clearance are very strict. In Germany, the clearance limit for $^{14}$C in graphite was reduced in 2019 from 80 Bq/g to 1.0 Bq/g, which requires highly accurate characterization. Without prior conditioning, reactor graphite would occupy about 70 % of the disposal capacity of the KONRAD repository [98].

At present, $^{14}$C determination in reactor graphite is usually performed by Liquid Scintillation Counting (LSC). LSC is a technique used to measure the activity of radioactive samples that emit low-energy $\beta$-radiation. The sample is mixed with a liquid scintillation cocktail consisting of an organic solvent, an organic scintillator, and a surfactant (emulsifier). When $\beta$-particles emitted by the radionuclide interact with the cocktail, their energy is converted into short flashes of light (scintillations). These light pulses are detected by photomultiplier tubes, converted into electrical signals, and counted. The number of pulses is proportional to the radioactive activity of the sample, allowing quantitative determination of $\beta$-emitting radionuclides [99].

Although LSC is a well-established method for measuring low-energy $\beta$-emitters, it requires labor-intensive sample preparation and may be affected by interfering radionuclides such as $^{36}$Cl. For this reason, AMS offers an attractive alternative.

In the AMS approach, graphite is oxidized to $CO_2$ and the $^{14}$R ratio is measured directly. This method combines high sensitivity with comparatively small sample masses and has the potential to increase sample throughput. Using an EA coupled to AMS, $CO_2$ samples with $^{14}$R values as low as $5{\cdot}10^{-14}$ can be measured. This is well below the free-release limit for reactor graphite of 1 Bq/g, which corresponds to a $^{14}$R value of $5.2{\cdot}10^{-12}$.

A challenge is that highly activated samples may contaminate the AMS measurement setup and thereby complicate subsequent measurements of low $^{14}$R ratios, typical for radiocarbon dating. To address this problem, the project investigates controlled dilution strategies prior to AMS analysis, including both mechanical dilution with dead graphite and gas dilution using the GIS.

The scientific objective of the project *"Charakterisierung und Quantifizierung von C-14 in Reaktorgrafit mittels Beschleuniger-Massenspektrometrie"* is therefore to establish a simple and efficient method for determining $^{14}$C in activated reactor graphite via AMS. Before presenting the first measurements, a short insight in $^{14}$C in nuclear power plants is given. Afterwards, the setup from this work, the sample material, and its irradiation are described in detail.

## 4.2 $^{14}$C in nuclear power plants

As discussed previously in Chap. 2.1, the atmospheric $^{14}$R can be modified by anthropogenic influences. However, there are also anthropogenic sources of $^{14}$C that do not enter the natural carbon cycle, because their high activity requires controlled storage and disposal.

Compared with the natural global production of $^{14}$C, anthropogenic production in nuclear reactors is substantial. The total annual production depends on reactor type and power, but has been estimated at approximately $1.1\cdot10^{15}$ Bq/a[1] [100].

In nuclear reactors, $^{14}$C is produced primarily through neutron-induced reactions in moderator and structural materials. In graphite moderators, the dominant production pathways are listed in Tab. 4.1. In addition to the $^{14}$N(n,p)$^{14}$C reaction, which is analogous to atmospheric production, neutron capture by $^{13}$C and $^{17}$O also contributes to the $^{14}$C inventory.

This thesis focuses specifically on $^{14}$C production in graphite-moderated reactors, in which reactor graphite constitutes the primary source of $^{14}$C activity. In Germany, most irradiated reactor graphite requiring storage originates from the prototype reactors THTR-300 (Thorium High Temperature Reactor) in Hamm-Uentrop and AVR (*Arbeitsgemeinschaft Versuchsreaktor Jülich*) in Jülich. Both facilities are pebble-bed reactors, with activated graphite occurring in reflector components, thermal columns, and fuel pebbles [98]. A simplified schematic of a pebble-bed reactor is shown in Fig. 4.1.

A pebble-bed reactor is a type of high-temperature[2] gas-cooled nuclear reactor that uses spherical graphite fuel elements, known as pebbles, instead of conventional fuel rods. Each pebble contains thousands of TRISO[3]-coated fuel particles, in which the fuel kernel is encapsulated by multiple ceramic layers that retain fission products and provide intrinsic containment. The reactor core consists of a vessel filled with graphite fuel pebbles, which also act as the neutron moderator. Helium gas flows through the pebble bed to remove the heat generated by nuclear fission and transfer it to the power conversion system. Fuel is continuously circulated: fresh pebbles are added at the top, move downward by gravity during operation, and are removed, inspected, and reintroduced at the top [101].

Nuclear fission reactions that generate heat occur within the fuel pebbles. Thermal neutrons interact with the uranium contained in the kernels, inducing fission

Table 4.1: Neutron induced reactions in graphite. Values taken from the IAEA nuclide chart.

| Reaction | Natural abundance of target | Thermal neutrons [b] |
|---|---|---|
| $^{14}$N(n,p)$^{14}$C | 99.6205 % | $1.86\pm0.03$ |
| $^{17}$O(n,$\alpha$)$^{14}$C | 0.03835 % | $0.235\pm0.01$ |
| $^{13}$C(n,$\gamma$)$^{14}$C | 1.06 % | $1.50\cdot10^{-3}\pm2\cdot10^{-5}$ |

---

[1] Estimate reported by the IAEA for 1998.

[2] Temperatures inside the reactor can reach up to 900°C [101].

[3] A TRISO-coated fuel particle consists of a uranium-bearing kernel (350–600 $\mu$m) surrounded by four coating layers: a porous pyrocarbon buffer layer, a dense inner pyrocarbon layer, a silicon carbide layer, and an outer pyrocarbon layer [102, 103].

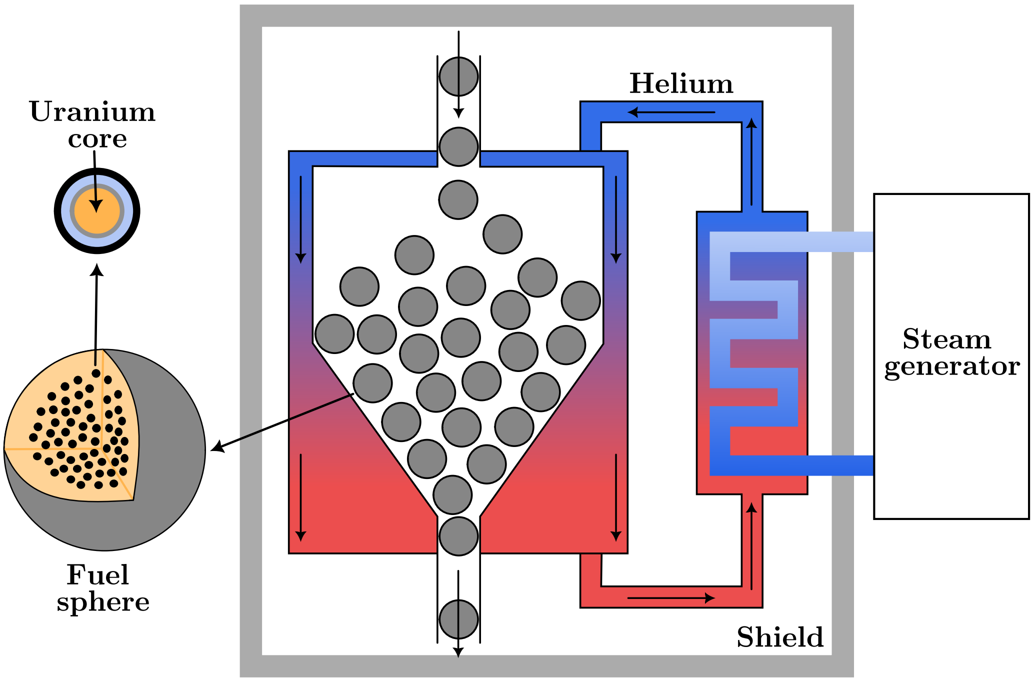

Figure 4.1: Schematic of a pebble-bed nuclear reactor. Fuel spheres are introduced from the top and gradually move downward through the reactor core. Nuclear fission within the fuel spheres generates heat, which is removed by circulating helium coolant. The heated helium is then used to produce steam, which in turn drives a turbine to generate electricity.

and producing fission products alongside with fast neutrons. The fission products are retained within the multilayer TRISO coating, particularly by the pyrocarbon layers, while the emitted neutrons are moderated by the surrounding graphite matrix and can subsequently induce further fission events.

In contrast to water-cooled reactors, where a loss of coolant, and thus moderator, suppresses the chain reaction, pebble-bed reactors exhibit inherent negative temperature feedback. As the fuel temperature rises, the fission rate decreases because of Doppler broadening[4].

---

[4] At higher temperatures, resonance absorption peaks broaden because of thermal motion of the nuclei, increasing neutron capture and thereby reducing reactivity [104].

## 4.3 Experimental Set-Up

As mentioned before, highly activated sample material can potentially contaminate the measurement setup and hinder reliable determination of low $^{14}$R ratios. Therefore, a different experimental setup was employed, using a separate EA (EuroVector EA3000) in combination with an in-house-built GIS, so that measurements of highly activated material can be carried out without risking contamination of the system used for radiocarbon dating with low $^{14}$R samples.

A picture of this system is shown in Fig. 4.2. A schematic of the EA used in this project, is shown in Fig. 4.4 i) of the publication in Chap. 4.5. It consists of an oxidation tube, a reduction tube, and a separation column. Similar to the COMORI setup, the samples are packed in tin boats and combusted in the oxidation reactor at approximately 1 000°C with the addition of $O_2$. During combustion, the gaseous products $CO_2$, $SO_2$, $H_2O$, and $NO_x$ are formed. These gases are transported by a helium flow to the copper-filled reduction reactor, where $NO_x$ is reduced to $N_2$. Subsequently, $N_2$ and $CO_2$ are separated in the separation column. First, $N_2$ is detected by the thermal conductivity detector (TCD), which generates a signal as described in Chap. 2.3.1. Afterwards, the separation column is heated to release the trapped $CO_2$, which is then detected by the TCD. Initially, the EA included an additional $H_2O$ trap; however, this was removed because it increased cross-talk between successive samples.

After detection in the EA, the $CO_2$ is transferred to the GIS, a schematic of which is shown in Fig. 4.4 ii). The GIS was built in-house and is used to dilute highly active sample gas with blank gas and to transfer the sample gas to the ion source through a capillary with a diameter of 60 $\mu$m. Similar to the GIS used in the COMORI setup, the system is equipped with a heatable zeolite trap, which

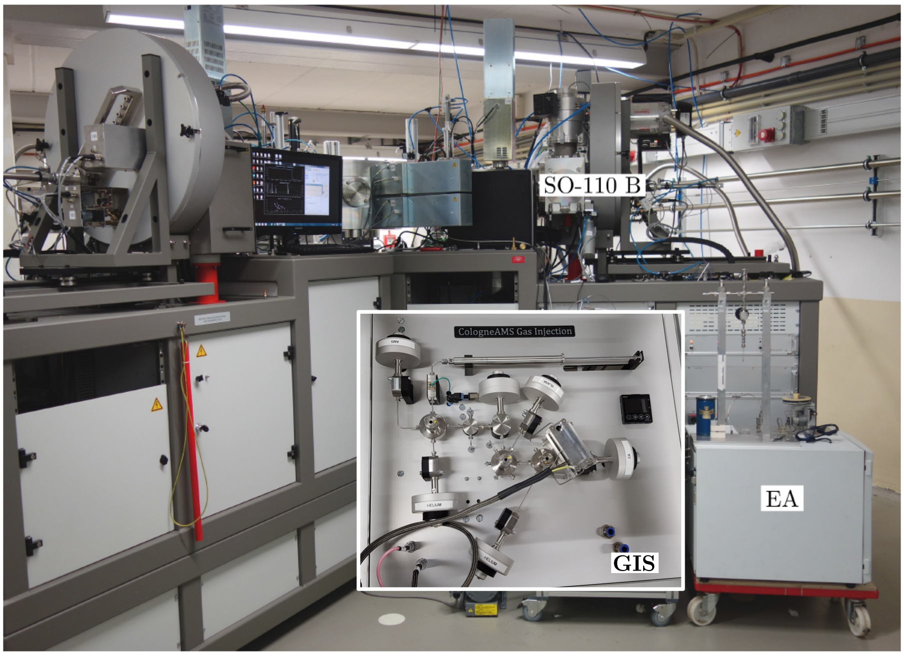

Figure 4.2: The $CO_2$ setup at the SO-110 B ion source of the 6 MV AMS system of CologneAMS. This figure was adapted from [51].

captures the $CO_2$ produced in the EA during the combustion of solid samples.

Further details on the EA (EuroVector EA3000) and the GIS can be found in [51].

## 4.4 Sample material and irradiation

For this project, different graphite materials were neutron-irradiated at the TRIGA II reactor of Johannes Gutenberg University Mainz by the Institute of Nuclear Chemistry of the University of Cologne. The sample material is shown in Fig. 4.3.

Materials labeled *K* and *S* are unused graphite components from the high-temperature reactor (AVR) operated by JEN mbH in Jülich. Material labeled *K* is identical to the graphite reflector material installed in close proximity to the AVR reactor core, whereas material labeled *S* corresponds to the graphite used in the thermal shield. Material labeled *G*, in contrast, served as shielding material for a decommissioned low-background measurement facility of the Department of Nuclear Chemistry at the University of Cologne.

The irradiation was carried out on 22.07.2019 and on 09.03.2020 by the Institute of Nuclear Chemistry of the University of Cologne. The exact irradiation times, reactor positions, and neutron fluxes $\mathbf{\Phi}$ are listed in Tab. 4.2.

Table 4.2: Neutron irradiation of sample graphite K, G and S. For run a and b the samples were irradiated sequentially in the pneumatic transfer systems, for run c all three samples were irradiated simultaneously in the central tube. The table is adapted from [98].

| | Duration [s] | $\mathbf{\Phi}$ [n cm$^{-2}$s$^{-1}$] | Date | Time |
|---|---|---|---|---|
| a | 60 | $1.6 \cdot 10^{12}$ | 09.03.2020 | K 11:58, G 11:38, S 11:16 |
| b | 1600 | $1.6 \cdot 10^{12}$ | 09.03.2020 | K 11:23, G 11:59, S 11:40 |
| c | 10800 | $4.2 \cdot 10^{12}$ | 22.07.2019 | 13:06 |

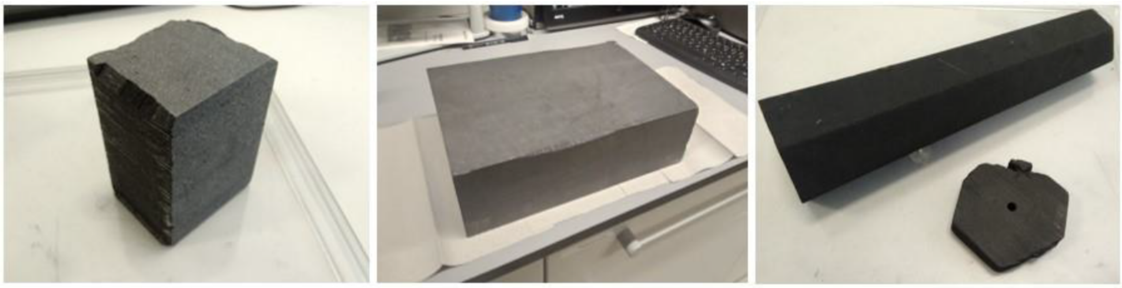

Figure 4.3: From left to right are shown the graphite sample materials *K*, *G* and *S*. The picture is adapted from [98].

## 4.5 III Publication: $^{14}$C AMS measurement of gas diluted reactor graphite using a Gas Injection System

In this paper, the measurement of activated reactor graphite by AMS using both mechanical dilution and gas dilution as an alternative to laborious LSC measurements is addressed. The work builds on preliminary studies shown in the following publication. In this preliminary work, mechanical dilution, done by the Institute of Nuclear Chemistry of the University of Cologne was first tested. Additionally, the newly developed gas dilution approach was validated using Ox-II standard material which was diluted with blank gas and subsequently measured for its $^{14}$R ratios with the AMS.

The research presented in this chapter was conducted within a nuclear waste management project funded by the German Federal Ministry of Education and Research (BMBF) under the project *"Charakterisierung und Quantifizierung von C-14 in Reaktorgrafit mittels Beschleuniger-Massenspektrometrie"* [98].

This work represents a collaboration between the Institute of Nuclear Chemistry and the Institute for Nuclear Physics at the University of Cologne, as well as the *Gesellschaft für Anlagen- und Reaktorsicherheit (GRS) gGmbH.*

Sample irradiation and preparation were carried out by the Department of Nuclear Chemistry, while the development of the experimental GIS setup, the sample measurements, and the data analysis were performed in this work.

Mechanical dilution of the graphite sample was carried out by R. Margreiter in the Department of Nuclear Chemistry. The AMS measurements of these samples at the 6 MV system were performed in this work [105].

The following publication is reproduced in its original published form in *Nuclear Instruments and Methods in Physics Research B.* For this reason, the wording, structure, and time perspective have been retained as in the original version. Statements referring to future work or ongoing developments reflect the status at the time of writing of the original manuscript.

# III Publication:
# $^{14}$C AMS measurement of gas diluted reactor graphite using a Gas Injection System

**Martina Gwozdz**[1], Raphael Margreiter[2], Timm-Florian Pabst[1], Gereon Hackenberg[1], Klaus Eberhardt[3], Stefan Heinze[1], Susan Herb[1], Markus Schiffer[1], Alexander Stolz[1], Erik Strub[2], Dennis Mücher[1], Alfred Dewald[1]

[1]University of Cologne, Institute for Nuclear Physics, Zuelpicher Str. 77, Cologne, 50937, Germany
[2]University of Cologne, Division of Nuclear Chemistry, Zuelpicher Str. 45, Cologne, 50674, Germany
[3]Johannes Gutenberg University Mainz, Institute for Nuclear Chemistry, Fritz-Strassmann-Weg 2, Mainz, 55128, Germany

published in

Nuclear Instruments and Methods in Physics Research B

Volume 533, Page 76-80

15 December 2022

## Abstract

For the final disposal of reactor graphite a quantitative characterization of its radioactivity is needed. In this work an emphasis is placed on the isotope $^{14}$C, an isotope accessible to AMS measurements. Reactor graphite can be highly activated and therefore difficult to measure without the risk of contaminating the AMS setup. Using an Elemental Analyzer (EA), a Gas Injection System (GIS) and the 6 MV AMS system of the Institute for Nuclear Physics, University of Cologne, we automated the measurement process for gaseous, diluted samples. This work presents initial steps toward verifying the feasibility of gas dilution and provides a comparison to samples with known concentrations of $^{14}$C. In the future, our system will provide a high sample throughput of gas-diluted probes with high activities.

### 4.5.1 Introduction

Currently, there are 250,000 tons of activated reactor graphite worldwide with no well-defined disposal path [106]. A relevant subgroup of this material is the approximately 1000 tons of reactor graphite in Germany, primarily from the prototype reactors AVR (Jülich) and THTR-300 (Hamm-Uentrop). The disposal of this type of material is still a challenge. The aim of the presented work is to develop and test efficient procedures and techniques using Accelerator Mass Spectrometry (AMS) to determine the concentration of radioactive elements in irradiated reactor graphite. This process would optimize the treatment of waste material and its final disposal.

Produced by the reactions $^{13}\mathrm{C}(\mathrm{n},\gamma)^{14}\mathrm{C}$, $^{14}\mathrm{N}(\mathrm{n},\mathrm{p})^{14}\mathrm{C}$ and $^{17}\mathrm{O}(\mathrm{n},\alpha)^{14}\mathrm{C}$ [107], $^{14}$C is one of the most relevant elements determining the total radioactivity of reactor graphite. The $^{14}$C activity ranges from the exemption limit of 80 Bq/g up to $\sim 10^6$ Bq/g [108, 109].

Since $^{14}$C is a low-energy $\beta$-emitter, its activity is usually measured via liquid scintillation counting (LSC) [110], requiring an elaborate sample preparation. AMS, as shown in [111][5], can offer alternative methods. One of these alternatives has been demonstrated by Enachescu *et al.* in [109]. Samples for their small 1 MV AMS facility are produced by combustion of the graphite material. After the combustion, the isotopes are separated by a dedicated apparatus which allows the extraction of $^3$H as HTO, $^{14}$C as $CO_2$ and $^{36}$Cl as ClAg. From these materials, standard sputter targets are prepared for the AMS measurement with no pre-treatment of the graphite.

In our work we follow a similar procedure as described in [109] but without the graphitization step and therefore without the production of $^{14}$C sputter targets. Instead, we inject the $^{14}CO_2$ gas, which is extracted after the combustion, directly into the sputter ion source via a dedicated Gas Injection System (GIS). A GIS (from Ionplus) has already been used successfully at CologneAMS for small samples with masses in the milligram range [57].

To allow measurements of samples with $^{14}\mathrm{C}/^{12}\mathrm{C}$ ratios above $10^{-12}$, we have built a new GIS system. The new system consists of an Elemental Analyzer (EA) from Elementar [51] and a GIS that we developed based on experience with the gas

---

[5] The original publications also referred to two additional manuscripts that were intended for publication but were ultimately not published.

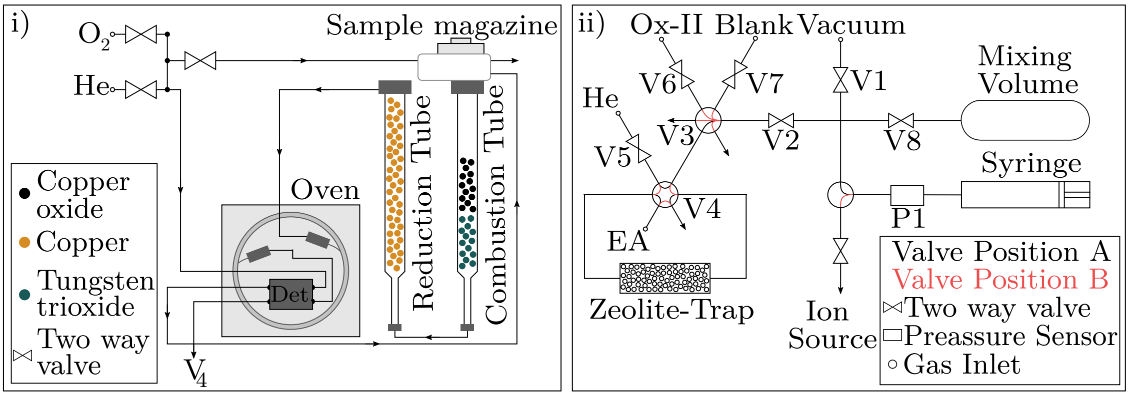

Figure 4.4: i) Experimental setup of the EA where samples are oxidized in the combustion tube and detected in the Thermal Conductivity Detector. ii) Tubing paths of the newly developed GIS. $CO_2$ of the samples oxidized in the EA, can be captured in the syringe after separation from other gases by the zeolite trap. This schematic is adapted from [51].

handling systems of Ionplus [58]. The hardware of the GIS is similar to the Ionplus system. An additional reservoir allows for a controlled dilution of sample material to allow for the measurement of higher activated probes. Additionally, a new software was developed to control the EA, GIS and the 6 MV AMS simultaneously to enable fully automated measurements.

In this work we present first test measurements of irradiated reactor graphite performed with the separate GIS from Ionplus. We also show first results using the new GIS by combusting standard Ox-II material and diluting it with blank gas.

### 4.5.2 Sample preparation and experimental setup

The principle of how samples are processed and measured does not depend on which GIS system is used. Therefore, the setup of the newly developed system is presented.

To test the principle of our combustion technique, reference samples of activated reactor graphite were created. The samples were prepared from graphite bricks from reflector material of the AVR reactor (sample K), which has not been previously irradiated. The material underwent neutron activation at the TRIGA II research reactor in Mainz, Germany, for 3 h in the central irradiation tube at a neutron flux of $4.2 \cdot 10^{12}$ cm$^{-2}$ s$^{-1}$.

The irradiated material was used to establish a reference sample with a specific dilution. The mechanical dilution of the irradiated samples was done with blank material. For this, the irradiated and blank materials were ground separately for 30 min at 30 Hz with 8–10 stainless steel balls (3 mm) in a VWR Star Beater ball mill. The procedure was repeated with a mixture of both materials in the mass ratios of 1:4 (sample K3t) and 1:10 (sample K9t). All materials were weighed separately and mixed in the milling container. The exact dilution ratios are 1:4.006 for K3t with an error of ±0.007 and 1:10.00 with an error of ±0.05 for K9t. The errors given for the dilution ratios include the error of the scale. By weighing each sample three times, then calculating the average mass and standard deviation, the Gaussian propagation gave the ratio error accounting for any error in the weighing process.

The GIS-AMS setup consists of three devices: the EA, where solid samples are oxidized; the GIS, to capture the $CO_2$ gas; and finally the 6 MV AMS for the $^{14}$C measurement.

The solid samples were oxidized in an EuroVector EA3000 Elemental Analyzer (see Fig. 4.4(i)). The EA consists of two reactors: a combustion reactor at 1020 °C filled with copper oxide to aid the combustion reaction, and a reduction reactor at 560 °C filled with copper to remove $NO_x$ from the combustion products. A thermal conductivity detector (TCD) detects the gas from the reduction reactor. From here, the helium carrier gas transports the gaseous sample towards the GIS. The tube paths of the new GIS, which were specifically designed to enable routine measurements of highly activated samples, can be seen in Fig. 4.4(ii). They have a similar setup as the EA (EuroVector EA3000) system but with an additional mixing volume. The gas from the EA passes through the zeolite trap of the GIS to capture the $CO_2$. Gases other than $CO_2$ pass through the trap and exit the GIS. The zeolite trap is then heated and releases the $CO_2$ into the syringe of the GIS.

The captured $CO_2$ sample gas can be diluted inside the syringe with blank gas. If higher dilutions are desired, the gas can also be led into the mixing volume. Samples diluted in the mixing volume are led back to the syringe. After the dilution, it is necessary to mix the sample and blank gas. This is done by driving the syringe back and forth to ensure a homogeneous sample gas. From the syringe, the sample gas is directed towards the ion source of the AMS. Measurements of $^{14}$C were performed using our 6 MV AMS. The setup is equipped with an extra HVE SO-110 B ion source from High Voltage Engineering Europa B.V. (2015) [112]. The ion source is optimized for gaseous $CO_2$. Stable isotopes such as $^{12}$C and $^{13}$C were measured in the offset Faraday cups behind the second magnet, while $^{14}$C was measured at the end in an ionization detector after the third magnet. With this setup, the measurement of one graphite sample can be completed in approximately 45 min.

The undiluted, neutron-activated graphite (K) as well as the dead graphite diluted samples (K9t and K3t) were measured with the old EA-GIS system. The purpose of the measurement was to test the mechanical dilution and to test the undiluted graphite for its activity. Diluted and activated samples were both measured to compare the $^{14}C/^{12}C$ ratio. Furthermore, the limits of the EA-GIS-AMS system were tested.

Finally, the Ox-II samples for the gas dilution in the new EA-GIS system were weighed and packed for oxidation. No further treatment was needed for these samples. For the first test run of the new GIS, a total of six Ox-II samples were oxidized. Two samples were measured without dilution, another two were diluted inside the GIS with blank gas approximately 3.5 times the amount of the sample mass. The last two were diluted with approximately 10 times the amount of blank gas than the sample mass. The dilution is represented as the dilution factor. The dilution factor is calculated by dividing the measured blank mass by the sum of the measured blank mass and sample mass.

### 4.5.3 CO$_2$ data analysis

In this section we describe the process to obtain the $^{14}C/^{12}C$ ratios for each sample. The raw AMS data obtained from the CO$_2$ measurements needs to be processed to reduce the effect of cross-contamination between samples and cross talk between measurements. The cross talk between measurements needs to be reduced especially for samples with high $^{14}$C content.

To correct for cross-contamination, which can occur during preparation and handling of the sample and during the measurement, blank material was oxidized in the EA. The data from the blank material is then subtracted from the sample ratios [58]. Additionally, the measuring routine is optimized. To reduce the cross talk, samples should be measured from the lowest to the highest $^{14}$C content, and cleaning of the GIS and the capillary (that leads the gaseous sample to the ion source) is performed in between each sample [14]. At the end, the data was calibrated with Ox-II standard samples, which have known ratios.

The $^{14}C/^{12}C$ ratio is represented as $^{14}$R and is corrected by subtracting the average $^{14}$R of the blanks and additionally calibrated by dividing this value by the average $^{14}$R of the corrected standards. Furthermore, $^{14}$R is standardized to $-25$ ‰ with an additional fractionation correction [51].

### 4.5.4 Results

#### Graphite measurements

In Fig. 4.5 three sample series are shown, where the measured $^{14}$R is corrected for its dilution. The blue data points are the undiluted graphite (K) with an average $^{14}$R value of $2.006 \pm 0.013 \cdot 10^{-11}$, the red are the same material diluted with dead graphite with a ratio of 1:4 (K3t). The average $^{14}$R value for K3t before the dilution correction lies at $4.877 \pm 0.032 \cdot 10^{-12}$. The black data points are the K9t samples with an average $^{14}$R value of $2.418 \pm 0.034 \cdot 10^{-12}$ before dilution correction. The standard deviation for the data set of K is $0.354 \cdot 10^{-12}$, $0.046 \cdot 10^{-12}$ for K3t and $0.053 \cdot 10^{-12}$ for K9t.

From the K series, $^{14}$R values for K3t and K9t can be calculated. Dividing the $^{14}$R by the respective dilution factor gives rise to $^{14}$R of K3t and K9t seen in Fig. 4.5.

Furthermore the measuring sequence of the samples is shown in Fig. 4.6. Each dilution series was measured on different days. Multiple Ox-II and blank samples were measured alongside each series for correction and calibration.

#### Ox-II dilution

The resulting $^{14}$R measured at the AMS for the Ox-II sample dilution can be seen in Fig. 4.7. For this measurement the samples are captured and diluted inside the syringe, then introduced to the ion source. The expected $^{14}$R ratios in Fig. 4.7 were determined by taking the mean of the measured $^{14}$R ratio of the undiluted sample and dividing it by the exact dilution factor which can be seen in Table 4.3.

For the final results, the data was calibrated and corrected as described in Section 3 and additionally corrected for its dilution. The error for the dilution

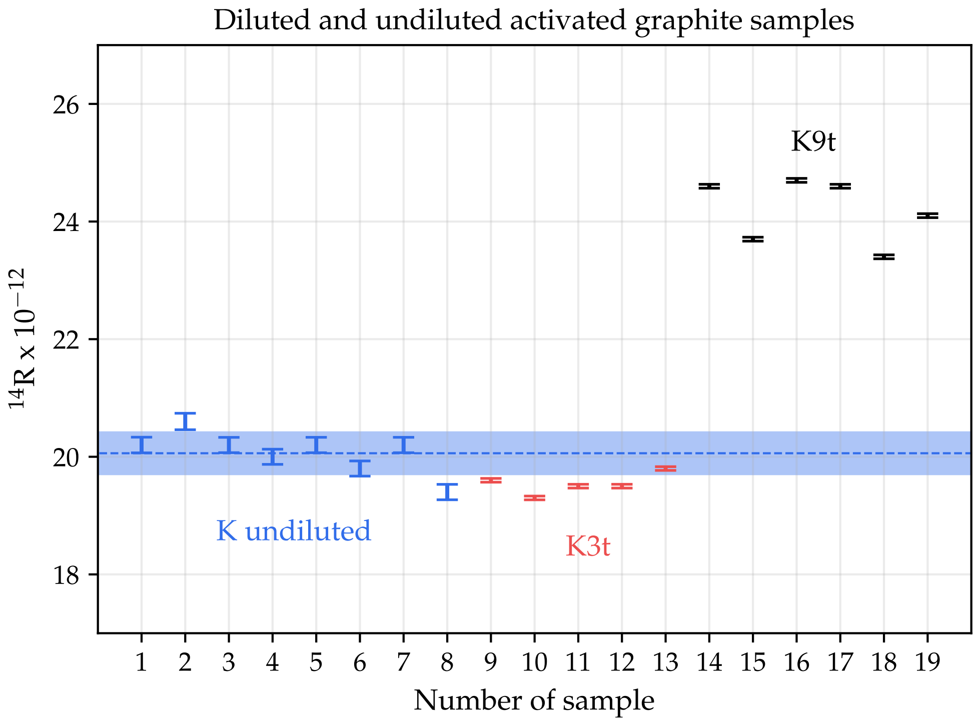

Figure 4.5: Three measurement series of activated graphite. The blue data shows the $^{14}$R of the undiluted graphite (K). The blue dotted line is the average $^{14}$R(K) with its standard deviation. The red data represents the diluted K3t graphite with a dilution ratio of 1:4.006 ± 0.007 and already corrected for its dilution factor. K9t is shown as the dilution corrected black data and their dilution is 1:10.00 ± 0.05.

factor is ±0.001 and is dependent on the accuracy of the pressure sensor in front of the syringe.

The dilution correction in Table 4.3 is done by multiplying the exact dilution factor with the measured $^{14}$R. The final results for the $^{14}$R of the Ox-II dilution can be seen in Table 4.3.

## 4.5.5 Discussion

### Graphite measurements

While the measured $^{14}$R values for the K3t are in agreement with expectations, Fig. 4.5 reveals a significant deviation of $^{14}$R for the K9t samples by 24.31% com-

Table 4.3: Results for the $^{14}$R ratio after calibration and dilution correction.

| Sample | Dilution | ± | Dilution corrected $^{14}$R | ± |
|---|---|---|---|---|
| 1 | Undiluted | - | $1.610\cdot10^{-12}$ | $1.723\cdot10^{-14}$ |
| 2 | Undiluted | - | $1.567\cdot10^{-12}$ | $1.746\cdot10^{-14}$ |
| 3 | 0.715102 | 0.001 | $1.493\cdot10^{-12}$ | $2.649\cdot10^{-14}$ |
| 4 | 0.675054 | 0.001 | $1.508\cdot10^{-12}$ | $2.345\cdot10^{-14}$ |
| 5 | 0.904812 | 0.001 | $1.569\cdot10^{-12}$ | $4.348\cdot10^{-14}$ |
| 6 | 0.904568 | 0.001 | $1.568\cdot10^{-12}$ | $3.299\cdot10^{-14}$ |

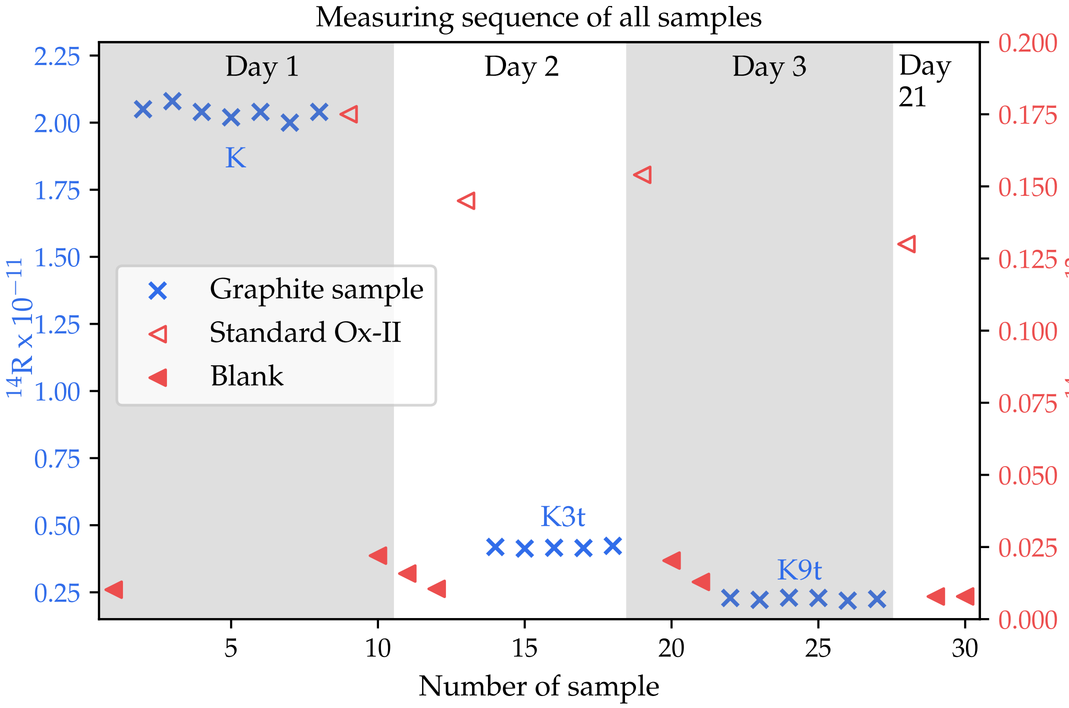

Figure 4.6: Measurement sequence of the samples on consecutive days. While the left hand axis shows the $^{14}$R of the graphite samples in blue, the right hand axis shows the $^{14}$R of the standard materials in red. The error for all blank samples is approximately 15 %, and approximately 2 % for Ox-II. The average error for K is 0.121 %, for K3t 0.256 %, and for K9t 0.353 %. Day 21 shows two blank values that were measured three weeks later, these values are normally reached.

pared to the K sample. To test if this issue can be explained by a cross talk problem due to measurements with higher activated samples, we show the measurement sequence of the graphite samples in Fig. 4.6.

Indeed, while $^{14}$R for the Ox-II standard typically is $1.3 \cdot 10^{-12}$, after the K series measurement this value was elevated to $1.751 \pm 0.011 \cdot 10^{-12}$. On day 2, after the K3t series measurement, this value was reduced to $1.448 \pm 0.006 \cdot 10^{-12}$, and further lowers to the expected value of $1.332 \pm 0.008 \cdot 10^{-12}$ by day 21.

This trend is also observed inspecting the measured raw data of the blank samples. After the K series $^{14}$R of the blank is $2.197 \pm 0.025 \cdot 10^{-13}$. Directly after K3t, which was measured a day later it was reduced to $1.313 \pm 0.026 \cdot 10^{-13}$. Three weeks later the blank further improves to $7.858 \pm 0.130 \cdot 10^{-14}$ which is the value normally reached.

Past tests of the EA-GIS system showed that the main source of cross talk is the GIS and its capillary to the ion source [51]. The capillary is a 2 m long glass capillary with an inner diameter of 60 $\mu$m which is protected by a PEEK capillary. The PEEK capillary is from Phenomenex. Although in our measurements the capillary was flushed with helium gas for several minutes between each measurement, we still observe this known cross talk in our data. Prior measurements have shown that, after a measurement of an activated sample with a $^{14}$R of $2 \cdot 10^{-10}$, eight hours of constant flushing with helium of the capillary was required to regain the full

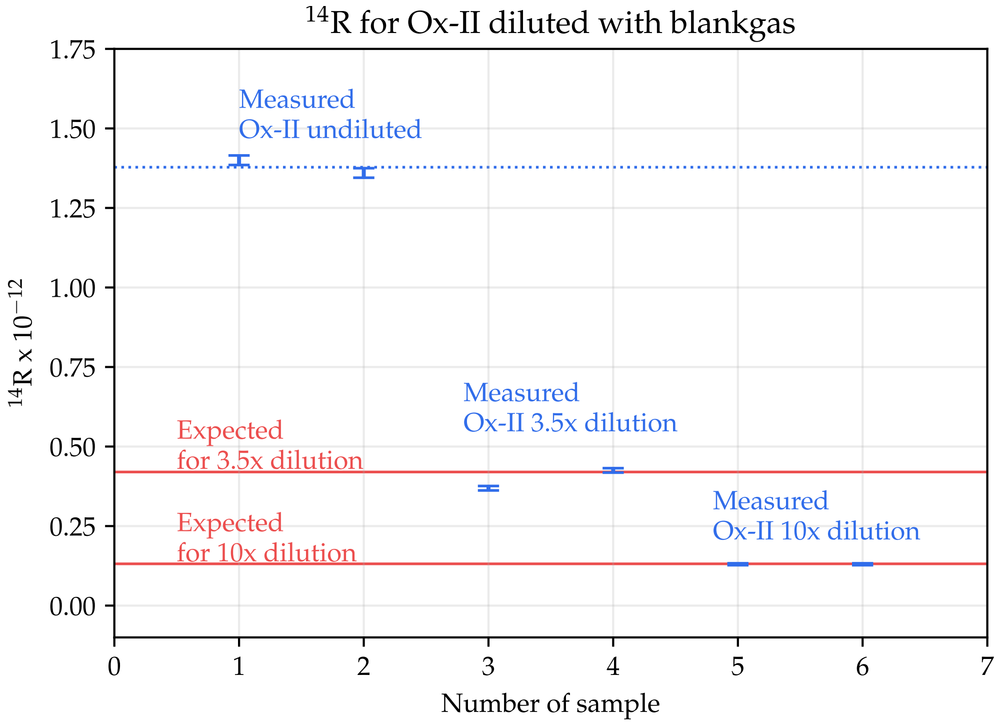

Figure 4.7: Measured $^{14}$R of standard Ox-II samples. The first two samples are undiluted samples to serve as a comparison. The red line describes the expected $^{14}$R for each dilution. The blue dotted line shows the average $^{14}$R of the measured Ox-II.

sensitivity of the setup. It was furthermore found that the EA does not play an important part in cross talk because the ratio of blank levels from the EA with blank gas directly from the GIS were consistent. Additionally, the 6 MV AMS device also can be eliminated as a source of cross talk as experience at the second identical ion source of the 6 MV AMS has shown that a $^{14}$R of three orders of magnitude higher than the $^{14}$R of the blank can be measured without cross talk.

Later tests of the new GIS showed a significant reduction of cross talk by having longer periods of flushing the system with blank gas and cleaning the system twice between samples. In those measurements, not reported here, dilutions of up to 1:81 were measured successfully. However, although we observe cross talk in our data based on the elevated blank and Ox-II results (see Fig. 4.6), this effect does not explain the observed discrepancy for the K9t data (Fig. 4.5). While a cross talk correction for K3t might explain the small systematic discrepancy towards lower $^{14}$R values, a cross talk correction would shift K9t to even higher $^{14}$R values. Furthermore, the observed effect of 24.31% is much larger than observed for the K3t data. A possible explanation for the K9t result might be attributed to sample losses during sample preparation. The initial K test series shows that non-uniform sample loss during the material transfer from the weighing to the grinding equipment significantly impacts the final results. Therefore, in the future, the mechanical dilution process needs to be adjusted to minimize sample losses. Future measurements will test our hypothesis.

Nevertheless, each dilution series indicates a good relative consistency, with the standard deviation of $^{14}$R being $0.354 \cdot 10^{-12}$ for the K series, $0.046 \cdot 10^{-12}$ for the K3t dilution, and $0.053 \cdot 10^{-12}$ for the K9t dilution. This result demonstrates that the dilution with dead graphite gives consistent data sets.

#### Ox-II dilution

The new EA-GIS-AMS system was tested with a small dilution series of Ox-II samples. Results are shown in Fig. 4.7 and are in good agreement with the expectations after a dilution correction. Cross contamination is not an issue in these measurements, as there are no highly activated samples used.

As expected, errors increase with higher dilutions because blank materials deliver a low $^{14}$C count leading to smaller statistics. From our result we estimate that Ox-II material can only be diluted up to a factor of approximately 13. As an example, Ox-II has a measured $^{14}$R of $1.39 \cdot 10^{-12}$. With a dilution factor of 13, $^{14}$R would be $1.07 \cdot 10^{-13}$. Taking into account that a typical error for blank samples is 15 %, $^{14}$R could be as low as $9.07 \cdot 10^{-14}$. For a dilution of 1:14, the measured ratios would then approach the blank level of $7 \cdot 10^{-14}$.

### 4.5.6 Conclusions

The main advantage of the GIS-AMS system is the possibility of dilution within the GIS to avoid the contamination of the main setup. The first graphite measurements show the possibility of measuring undiluted graphite, and the successful calculation and measurement of $^{14}$R for diluted samples in case of K3t. When cross talk due to the contamination of the system is reduced in future measurements, the new GIS setup can be used to dilute samples with blank gas. Significant cross talk reduction was already achieved by cleaning and flushing the GIS in between samples. Future studies will transform our efforts into an independent system, eliminating the complex sample preparation currently in use.

First test dilutions of Ox-II samples with the new GIS were successfully executed, and deliver the expected results. Final measurements of the gas dilution system have yet to be performed. A reference mechanical dilution series has already been prepared for this purpose. The material stems from the thermal shielding of the AVR reactor, as well as shielding material of a low-level radiation measuring station in the nuclear chemistry division at the University of Cologne. First preliminary results indicate that we can measure dilutions of down to 1:81 with good precision.

## Declaration of competing interest

The authors declare that they have no known competing financial interests or personal relationships that could have appeared to influence the work reported in this paper.

## Acknowledgment

The research is supported by the German Federal Ministry of Education and Research, funding code: 15S9410B.

## 4.6 Measurement of gas diluted graphite samples

The preliminary results presented in this publication demonstrated that the newly developed EA-GIS-AMS setup is suitable for dilution measurements. Mechanical dilution of graphite samples showed that dilution-corrected $^{14}$R values can be reproduced reliably, while the first gas-dilution experiments with Ox-II standards confirmed that the GIS can be used to dilute $CO_2$ samples and still recover the expected $^{14}$R ratios after correction. These results established the basis for applying the method to activated reactor graphite and for comparing mechanical and gas dilution under realistic sample conditions.

Based on these preparatory studies, the second part of this chapter addresses activated reactor graphite. Mechanically diluted and gas diluted graphite samples are measured and compared in order to assess whether gas dilution provides a reliable method for the determination of $^{14}$C in activated graphite.

This part of the work is based on the measurement of actual reactor graphite material and was published in the GRS report *GRS-709, ISBN 978-3-910548-00-8* [98]. As the report was prepared collaboratively, only those parts that were written and analyzed within the scope of this thesis are included here. The is shown in Chap. 4.6.1 which has been revised and expanded academically for inclusion in this dissertation.

The experimental setup used in this work is identical to that described in Chap. 4.5.

The standards measured in the publication discussed in Chap. 4.5 differ in their definition of the dilution level. It is now defined by the amount of blank gas added relative to the sample mass. For a quantitative description of this dilution, the spiking ratio is introduced. It is defined as

$$\text{spiking ratio} = \frac{\text{blank mass}}{\text{sample mass} + \text{blank mass}}$$

and first established by A. Stolz [51].

### 4.6.1 Gas dilution vs mechanical dilution

In the work presented in Chap. 4.5, the sample preparation procedure for mechanical dilution was tested using sample material $K$, and the setup for gas dilution was established. After successful dilution of the samples with blank gas inside the syringe, a measurement series could be carried out for samples $G$ and $S$ using the gas-dilution and the mechanical dilution method.

The two sample types, $G$ and $S$, were analyzed, each comprising four different dilution factors and one undiluted measurement.

At the beginning and end of each measurement series, Ox-II and blank samples were measured alongside with the graphite samples. Additional Ox-II measurements were performed between the different dilutions to verify that the system had not been contaminated by activated graphite and that no crosstalk occurred between samples. Owing to technical problems with the measurement software at the end of the first $G$ measurement series, the final standards could not be recorded. Ox-II standards measured only after a prolonged interruption no longer provide reliable information for contamination checks because too much time has elapsed.

Table 4.4: Mechanical and gaseous dilution ratio of G and S sample. Table adapted from [98].

| Sample | Dilution Ratio (mechanical) | Spike Ratio (gas) |
|---|---|---|
| G | - | - |
| G3 | 1:3.00(1) | 0.8427(38) |
| G9 | 1:9.07(5) | 0.8953(34) |
| G27 | 1:27.05(17) | 0.96329(20) |
| G81 | 1:81.24(60) | 0.98796(13) |
| S | - | - |
| S3 | 1:2.99(2) | 0.8363(40) |
| S9 | 1:8.96(9) | 0.9375(13) |
| S27 | 1:26.82(34) | 0.96398(95) |
| S81 | 1:80.46(120) | 0.98880(13) |

To compare the gas-diluted samples with the original activated material, the $^{14}$R values of the undiluted *G* samples were used as the reference for both the gas-diluted and mechanically diluted samples. The results for sample *G* are shown in Fig. 4.8 i) and ii).

For the undiluted *G* samples, shown in gray, the mean $^{14}$R value is $2.846 \cdot 10^{-11}$. This value was calculated from three measurements of sample *G*, and the corresponding uncertainty is given by the standard deviation of these three measurements.

Each diluted sample was also measured three times per dilution level. For each dilution, the mean value was determined, and the standard deviation was used as the uncertainty. Using the dilution ratios of the *G* samples listed in Tab. 4.4, the original $^{14}$R values were calculated. After correction for dilution, these values can be compared with the $^{14}$R value of the undiluted *G* sample. These corrected results are also shown for sample *G* in Fig. 4.8 i) and ii).

For the mechanically diluted samples (Fig. 4.8 i)), *G9* and *G27* (where the number in the sample name denotes the dilution factor) agree with the undiluted *G* sample within the uncertainty range after correction for dilution, and their uncertainties remain below 3.0 %. The uncertainty of *G3* is 1.6 %, whereas *G81* shows a substantially larger uncertainty of 8.9 %. In contrast to *G9* and *G27*, *G3* deviates from the undiluted $^{14}$R value of *G* by 12.0 %, while *G81* differs by 17.0 %.

The dilution-corrected gas measurements of the *G* samples are shown in Fig. 4.8 ii). For the days on which these samples were measured, four of the ten Ox-II standards showed elevated $^{14}$R values. The blanks measured immediately afterward did not show increased $^{14}$R values. As no technical explanation for this behavior could be identified and the subsequent blanks remained unaffected, these elevated Ox-II measurements were excluded from the analysis.

The spiking ratios for the gas dilutions are listed in Tab. 4.4. For the gas-diluted *G* samples, the uncertainties are 26.0 % for *G81*, 29.0 % for *G27*, 11.4 % for *G9*, and 18.7 % for *G3*. All values remain within the uncertainty range of the undiluted sample. The deviations from the undiluted values are 23.1 % for the 81-fold dilution, 15.4 % for the 27-fold dilution, 8.5 % for the 9-fold dilution, and 23.1 % for the 3-fold dilution.

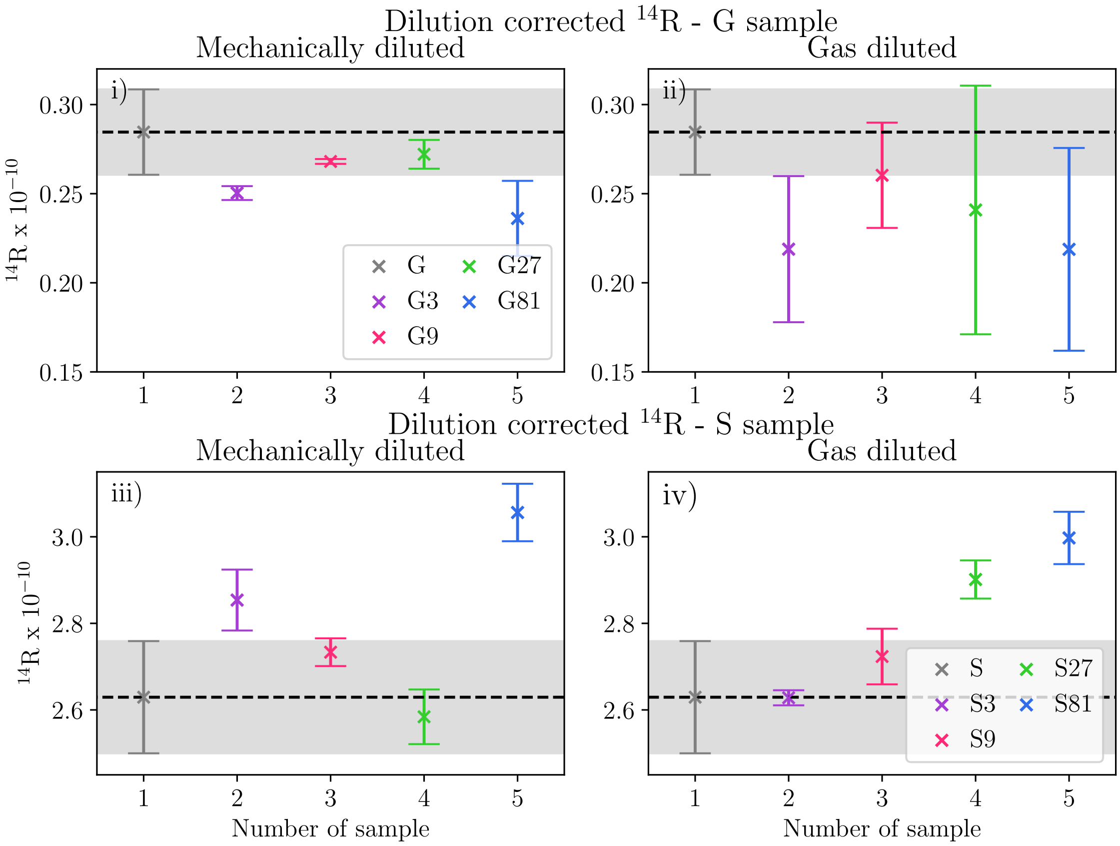

Figure 4.8: The G and S samples in the mechanically diluted samples (i) and (iii) were corrected using their dilution factor. The values represent the mean values of all samples of one type of dilution. The errors are given by the corresponding standard deviations. Graph (ii) and (iv) show the mean values of the gas-diluted samples, which are also corrected for dilution. The black dashed line indicates the measured $^{14}$R ratio of the undiluted sample with its standard deviation in gray. Figure adapted from [98].

The second sample material, *S*, was measured on two consecutive days for the mechanical dilution series. On the first day, only one dilution was measured at a time. After the threefold diluted sample, the Ox-II standard exceeded the expected value by more than a factor of two. To avoid possible crosstalk into the subsequent measurements, the run was stopped. On the following day, the sample order was changed and the cleaning procedure between measurements was modified to minimize possible crosstalk.

The dilution ratios of the mechanically diluted samples are listed in Tab. 4.4. For all mechanically diluted *S* samples, the uncertainties remain below 2.5 %, whereas the uncertainty of the undiluted *S* sample is 4.9 %. The largest deviation from the $^{14}$R value of *S* is observed for *S81*, which is 16.2 %. For *S27* and *S9*, the deviation from *S* remains below 4.0 %.

The gas-diluted *S* samples were also measured on two days. On the second day, two of the five Ox-II standards were excluded from the correction, because these standards showed elevated $^{14}$R values, but the $^{14}$R values of the blanks measured afterward were unaffected. For the gas-diluted *S* samples, the uncertainty remains below 2.50 % for all dilutions. The deviation from the undiluted $^{14}$R value is 14.0 % for *S81*, 10.3 % for *S27*, 3.6 % for *S9*, and 0.1 % for *S3*.

Compared with the *K9t* samples discussed in Chap. 4.5.5, the mechanically diluted samples presented here show an improved overall agreement with the undiluted material. While deviations of up to 25 % were observed for the *K9t* samples, the maximum deviation in the present measurement series is 17.0 % for the mechanically diluted *G* samples at higher dilution. This trend is also supported by the *S* samples, for which the deviations of *S3*, *S9* and *S27* are below 4.0 %. At the higher dilution level of 81, however, the deviations increase for both sample types up to 17.0 %. This maximum deviation is therefore of comparable magnitude for both dilution methods.

The gas-diluted G samples show larger scatter in the $^{14}$R ratio than the mechanically diluted samples. For the mechanically diluted G samples, the uncertainties remain below 3 % for *G3*, *G9*, and *G27*, whereas G81 shows an uncertainty of 8.9 %. In contrast, the gas-diluted *G* samples show uncertainties between 11.4 % and 29.0 %. Large deviations from the undiluted reference value are also observed for the 81-fold mechanically diluted sample and the 81-fold gas-diluted *S* sample.

For the *S* samples, the deviations from the undiluted reference value remain below 16.2 % for the mechanically diluted series and below 14.0 % for the gas-diluted series. The corresponding uncertainties of the diluted samples remain below 2.5 % for both dilution methods.

### 4.6.2 Discussion

The comparison between the mechanical and the gas dilution of the activated reactor graphite shows that the mechanically diluted samples provide more precise results. This is particularly evident for sample *G*, for which the mechanically diluted samples *G9* and *G27* agree with the undiluted material within uncertainty, while the gas-diluted *G* samples exhibit substantially larger scatter and higher relative uncertainties. For the mechanically diluted *G* samples, the uncertainties remain below 3 % for *G3*, *G9*, and *G27*, whereas the gas-diluted *G* samples show uncertainties between 11.4 % and 29.0 %. The mechanically diluted *S* samples remain comparatively close to the undiluted reference, with deviations below 4.0 % for *S3*, *S9*, and *S27*. This indicates that mechanical dilution yields robust results.

A likely explanation for the gas dilution is that the measured $^{14}$R values are influenced not only by the dilution factor, but also by a constant contamination contribution inside the GIS, similar to what is discussed in Chap. 2.4.5. In the gas-dilution approach, dilution with blank gas lowers the $^{14}$R ratio of the sample. As a result, a constant contamination contribution represents a larger fraction of the measured sample. This effect is visible for the gas-diluted *G* samples, which show large relative uncertainties and deviations after dilution correction.

This interpretation is supported by the behavior of the *S* samples. In the present measurements, the gas-diluted *S* samples show smaller uncertainties than the gas-diluted *G* samples. This is because the *S* sample has a higher $^{14}$R ratio. Therefore, the same absolute contamination contribution leads to a smaller relative effect. The comparison between *G* and *S* indicates that the absolute $^{14}$R level of the sample is an important parameter for the achievable precision of the gas-dilution method.

A constant contamination contribution is also expected for the mechanically diluted samples. In this case, however, the contamination is added to a much larger amount of sample material, so that its relative influence remains smaller. This is consistent with the lower uncertainties and smaller deviations observed for the mechanically diluted series. The results therefore suggest that mechanical dilution is less sensitive to constant contamination effects than gas dilution.

The comparison with the *K9t* samples discussed in Chap. 4.5.5 further supports this conclusion. While deviations of up to 25 % were observed for the *K9t* samples, the maximum deviation is the mechanically diluted *G* series with 17.0 %. A similar trend can be shown for the *S* samples, for which the deviations of *S3*, *S9*, and *S27* remain below 4.0 %. At the highest dilution level of 1:81, however, the deviations increase for both sample types and both dilution methods. These high-dilution cases should therefore be interpreted with caution.

With respect to contamination control of the AMS system, the dilution approach can nevertheless be regarded as successful. No clear evidence of crosstalk was observed in the measurements. The elevated Ox-II standards were followed by blank measurements that did not show increased $^{14}$R values, indicating that these effects were not caused by crosstalk from the activated graphite samples. Dilution therefore fulfilled its main purpose of reducing the amount of $^{14}$C introduced into the system and allowing highly activated samples to be measured without measurable contamination of subsequent samples.

From a practical point of view, the AMS-based workflow used here is also comparatively efficient. In the present procedure, the preparation and measurement of one AMS sample require approximately 1 to 1.5 h, while the active labor input is low and is largely limited to mortar grinding and sample handling. By contrast, published LSC workflows for $^{14}$C involve additional preparation steps such as combustion or oxidation, trapping of the released $CO_2$, mixing with scintillation cocktail. Reported LSC sample-preparation times can reach up to 5 h [113, 107]. This would imply that, in the course of a working week, approximately 40 graphite samples could be measured by AMS with relatively little oversight, whereas LSC would allow the measurement of only 10 to 20 samples and would require substantially more labor-intensive handling. Overall, the AMS route used here is therefore less labor-intensive and more convenient for routine analysis than conventional LSC-based approaches.

Using the free-release threshold adopted in this work, $5 \cdot 10^{-12}$, the present AMS measurements are sensitive enough to identify samples that are substantially above this limit. For routine application, one factor must be taken into account. When considering the present data, the measurement uncertainties for diluted graphite samples can reach up to 30 %. To ensure that a sample can be classified as reliably above the free-release limit, the measured $^{14}$R value should therefore lie at least two standard deviations above the threshold. This corresponds to a margin of 60 % above the free-release limit, resulting in a $^{14}$R value of $8.32 \cdot 10^{-12}$. For additional conservatism, this value can be rounded up to $9 \cdot 10^{-12}$. Consequently, when measuring diluted graphite, the resulting $^{14}$R value should lie above $9 \cdot 10^{-12}$. If this condition is not fulfilled, the dilution factor should be reduced. This process could be implemented in an automated GIS routine: a sample would first be measured at high dilution, and if the resulting $^{14}$R value does not exceed $9 \cdot 10^{-12}$ after a short measurement time, the dilution factor would be reduced for a second measurement.

Overall, the present results show that AMS measurement of diluted $CO_2$ is a practical method for the analysis of activated graphite and offers clear advantages in terms of automation, sample throughput, and protection of the AMS system from contamination. At the same time, comparison of the two dilution methods shows that mechanical dilution currently provides the more robust analytical performance. However, gas dilution could become the more efficient approach if the GIS were automated to optimize the dilution factor and thereby improve the measurable $^{14}$R range.

## 4.7 Summary

This work investigates the usage of AMS for the determination of $^{14}$C concentrations in reactor graphite within the framework of nuclear waste management. The main objective was to evaluate whether AMS combined with gas dilution techniques could provide a reliable and efficient alternative to the currently used LSC.

To achieve this goal, a GIS coupled to an EA and the 6 MV AMS system at the University of Cologne was used. The system allows the direct measurement of $^{14}CO_2$ gas extracted from combusted graphite samples without the need for laborious sample preparation. An additional mixing procedure was implemented in the GIS to enable controlled dilution of highly activated samples with blank $CO_2$ gas, thereby preventing contamination of the AMS setup.

Initial experiments focused on the validation of the dilution concept using neutron activated graphite and standard materials. Mechanical dilution experiments with activated graphite (sample *K*) demonstrated that consistent $^{14}$R ratios can be obtained for diluted samples. The dilution-corrected results of the *K3t* samples showed good agreement with the undiluted graphite reference, confirming the feasibility of dilution of $^{14}$C concentrations with dead material. However, deviations were observed for the highest dilution (*K9t*), likely caused by sample losses during the mechanical preparation process.

To test the gas dilution capabilities of the new GIS system, Ox-II standard material was combusted and diluted with blank gas. The dilution-corrected $^{14}$R ratios agreed well with the expected values, demonstrating that controlled dilution inside the GIS is technically feasible. The results also showed that increasing dilution factors lead to larger statistical uncertainties due to decreasing $^{14}$C count rates. Based on these measurements, reliable Ox-II dilution measurements appear feasible up to a dilution factor of 1:81 under the tested conditions.

Subsequent measurements were performed on graphite materials (samples labeled *G* and *S*) using both mechanical and gas dilution. The mechanically diluted samples generally showed small deviations from the undiluted reference values, typically below a few percent for moderate dilution levels. Gas-diluted samples produced comparable mean values but exhibited larger statistical uncertainties, especially for high dilution factors. At the highest dilution levels (approximately 1:81), both dilution methods showed increased deviations due to the small amount of original sample material remaining in the diluted gas mixture.

Overall, the experiments demonstrated that AMS combined with gas dilution can be used to determine $^{14}$C concentrations in reactor graphite. The results further indicate that gas dilution measurements can achieve an accuracy comparable to mechanical dilution while significantly simplifying the sample preparation process compared to LSC.

In the future, the presented approach could significantly simplify and accelerate the determination of $^{14}$C in reactor graphite. Such a system could be particularly beneficial in the context of the decommissioning of nuclear facilities, where large amounts of irradiated graphite are expected to arise. Reliable and rapid AMS measurements of $^{14}$C would help to characterize the radiological inventory of these materials with high sensitivity and could support decisions regarding storage, clearance, or disposal.

The developed approach also demonstrates that AMS measurements can be performed reliably when combined with automated gas dilution through the GIS. In practice, measurements can initially be performed at high dilution factors to avoid potential contamination of the AMS system when analyzing samples with unknown activation levels. The dilution can then be gradually reduced until a suitable measurement range is reached where sufficient $^{14}$C atoms can be measured. This approach helps prevent contamination while still allowing accurate measurements.

Overall, the results indicate that AMS combined with EA and GIS has strong potential as an efficient analytical tool for the characterization of irradiated graphite. In the long term, this could reduce the analytical effort required for large graphite inventories and improve the management and storage strategies for such materials during reactor decommissioning.

# Chapter 5

# Conclusion and outlook

In conclusion, the results of this thesis demonstrate that direct AMS measurement of $CO_2$ is well suited for samples for which material is limited or preparation must be efficient.

The studies presented here show that $CO_2$-based AMS can provide reliable results across very different applications, ranging from dendrochronological samples to activated reactor graphite. For tree-ring material, direct $CO_2$ measurement enables radiocarbon analysis with very small sample masses. For reactor graphite, the direct measurement of $CO_2$ offers a promising alternative to more labor-intensive conventional methods and may simplify future characterization workflows in nuclear waste management.

An important addition is the possibility of quasi-simultaneous measurements of stable isotopes alongside the unstable $^{14}C$ isotope. The COMORI setup allows the determination of $\delta^{13}C$ by IRMS and $^{14}C$ by AMS from the same sample. This setup could now be used for a broad range of archaeological applications where both stable-isotope information and radiocarbon ages are required from limited sample material. Materials such as tiny charcoal fragments [114], botanical remains [115] or organic residues [116] may become increasingly accessible to radiocarbon analysis without the need for graphitization.

For dendrochronological applications, the outlook is also promising. In the future, ring-by-ring AMS measurements could be done for the trees found in Paderborn. Such a high-resolution dataset would be valuable for creating short floating chronologies. The present study has shown that the site contains a valuable archive of Late Glacial pine, even though the available ring sequences are still too short for secure cross-dating. Future work should therefore focus on expanding the dataset. This would improve the chronology of the assemblage and may clarify whether some of the dendrochronological groups overlap in time. At the same time, more detailed radiocarbon measurements could help to test competing depositional scenarios, including repeated fluvial transport, temporary upstream storage, and later remobilization of older wood. In this way, AMS measurements may contribute not only to chronology building, but also to the reconstruction of Late Glacial sedimentary and landscape dynamics.

In the field of nuclear waste management, the outlook is equally significant. The experiments with activated graphite show that AMS combined with direct $CO_2$ measurement and automated gas dilution can provide a sensitive and comparatively efficient route for determining $^{14}$C concentrations. Further technical development should aim at making this approach more robust for routine operation on materials with highly variable or initially unknown activity levels. AMS could become an attractive alternative to LSC, especially where large numbers of samples have to be processed during reactor decommissioning.

Finally, the long-term importance of this work lies in its flexibility. Direct $CO_2$ measurement is not only a substitute for graphite preparation. Graphite targets will remain advantageous where the highest precision is required and sufficient sample material is available. Direct $CO_2$ AMS, however, offers clear advantages wherever sample mass is limited, measurement throughput is important, or sample preparation should be minimized.

Overall, the results of this thesis indicate that direct $CO_2$ AMS is a powerful and broadly applicable technique.

# Bibliography

[1] F.N.D Kurie. *Phys. Rev.*, 45:904, 1934.

[2] W.E. Burcham and M. Goldhaber. The disintegration of nitrogen by slow neutrons. *Proc. Camb. Phil. Soc.*, 32:632, 1936.

[3] M. D. Kamen. Early History of Carbon-14. *Science*, 140(3567):584–590, 1963.

[4] S. A.Korff. On the contribution to the ionization at sea-level produced by the neutrons in the cosmic radiation. *Terrestrial Magnetism and Atmospheric Electricity*, 45(2):133–134, 1940.

[5] W. F. Libby. Atmospheric Helium Three and Radiocarbon from Cosmic Radiation. *Phys. Rev.*, 69:671–672, 1946.

[6] A. G. Engelkemeir, W. H. Hamill, M. G. Inghram, and W. F. Libby. The Half-Life of Radiocarbon ($C^{14}$). *Phys. Rev.*, 75:1825–1833, 1949.

[7] E. C. Anderson and W. F. Libby. World-wide distribution of natural radiocarbon. *Physical Review*, 81:64–69, 1951.

[8] H. Godwin. Radiocarbon Dating - Fifth international conference. *Nature*, 195:943–945, 1962.

[9] J. R. Arnold and W. F. Libby. Age Determinations by Radiocarbon Content: Checks with Samples of Known Age. *Science*, 110(2869):678–680, 1949.

[10] C. L. Bennett, R. P. Beukens, M. R. Clover, D. Elmore, H. E. Gove, L. Kilius, A. E. Litherland, and K. H. Purser. Radiocarbon Dating with Electrostatic Accelerators: Dating of Milligram Samples. *Science*, 201(4353):345–347, 1978.

[11] M. Paul, W. Henning, W. Kutschera, E.J. Stephenson, and J.L. Yntema. Measurement of the 26Mg(p, n)26 Alg (7.2 × 105) yr cross section via accelerator mass spectrometry. *Physics Letters B*, 94(3):303–306, 1980.

[12] K. Nishiizumi, E. L. Winterer, C. P. Kohl, J. Klein, R. Middleton, D. Lal, and K. R. Arnold. Cosmic ray production rates of 10Be and 26Al in quartz from glacially polished rocks. *Journal of Geophysical Research: Solid Earth*, 94(B12):17907–17915, 1989.

[13] J. O. Melchert. AMS Radiocarbon analysis of Greenhouse gases: Method development and application. *PhD thesis, University of Cologne*, 2022.

[14] A. Stolz, A. Dewald, R. Altenkirch, S. Herb, S. Heinze, M. Schiffer, and T. Dunai. Radiocarbon measurements of small gaseous samples at CologneAMS. *Nucl. Instrum. Methods Phys. Res. B*, 406:283–286, 2017.

[15] H. A. Synal, M. Stocker, and M. Suter. MICADAS: A new compact radiocarbon AMS system. *Nuclear Instruments and Methods in Physics Research, Section B: Beam Interactions with Materials and Atoms*, 259:7–13, 2007.

[16] M. Gwozdz. Integration of the EA-IRMS system to the Cologne AMS facility. *Master thesis - University of Cologne*, 2021.

[17] J. S. Vogel and A. M. Stolz. Ion-pair Ionization in CO2-fed Cesium Sputter Sources. *Radiocarbon*, 61(6):1805–1812, 2019.

[18] R. Middleton. A Negative-Ion Cookbook. 1989. https://www.pelletron.com/cookbook.pdf.

[19] R. Middleton. A versatile high intensity negative ion source. *Nuclear Instruments and Methods in Physics Research*, 214(2):139–150, 1983.

[20] J. S. Vogel. Anion formation by neutral resonant ionization. *Nuclear Instruments and Methods in Physics Research Section B: Beam Interactions with Materials and Atoms*, 361:156–162, 2015.

[21] J. S. Vogel and J. A. Giacomo. Increased 14C AMS Efficiency from Reduced Competitive Ionization. *Radiocarbon*, 59(3):957–965, 2017.

[22] R.O. Sayer. Semi-empirical formulas for heavy-ion stripping data. *Rev. Phys. Appl.*, 12(10):1543–1546, 1977.

[23] M. Suter, S. Maxeiner, H. A. Synal, and C. Vockenhuber. Charge-state distributions and charge-changing cross sections and their impact on the performance of AMS facilities. *Nuclear Instruments and Methods in Physics Research Section B: Beam Interactions with Materials and Atoms*, 437:116–122, 2018.

[24] F. Hinterberger. Physik der Teilchenbeschleuniger und Ionenoptik. page 202. Springer Berlin, Heidelberg, ISBN 978-3-540-75282-0, second edition edition, 2008.

[25] G. Eigen. *Detectors in High-Energy Physics Experiments.* Springer, ISBN 978-3-031-67335-1, 2025.

[26] Harry Friedmann. *Einführung in die Kernphysik.* Wiley-VCH, ISBN 978-3-527-41248-8, 2014.

[27] G. A. Kovaltsov, A. Mishev, and I. G. Usoskin. A new model of cosmogenic production of radiocarbon 14C in the atmosphere. *Earth and Planetary Science Letters*, 337-338:114–120, 2012.

[28] M. Pandow, C. Mackay, and R. Wolfgang. The reaction of atomic carbon with oxygen:significance for the natural radio-carbon cycle. *Journal of Inorganic and Nuclear Chemistrys*, 14:153–158, 1960.

[29] P. Jöckel, M. G. Lawrence, and C. A. M. Brenninkmeijer. Simulations of cosmogenic 14CO using the three-dimensional atmospheric model MATCH: Effects of 14C production distribution and the solar cycle. *Journal of Geophysical Research: Atmospheres*, 104(D9):11733–11743, 1999.

[30] P. Damone and R. Sternberg. Global production and decay of radiocarbon. *Radiocarbon*, 31(3):697–703, 1989.

[31] H. Wanner, J. Beer, J. Bütikofer, T. J. Crowley, U. Cubasch, J. Flückiger, H. Goosse, M. Grosjean, F. Joos, J. O. Kaplan, M. Küttel, S. A. Müller, I. C. Prentice, O. Solomina, T. F. Stocker, P. Tarasov, M. Wagner, and M. Widmann. Mid- to Late Holocene climate change: an overview. *Quaternary Science Reviews*, 27(19):1791–1828, 2008.

[32] S. Rout, S.Yadav, V. Pulhani, and A. V. Kumar. A critical review of radiocarbon in environment. *Discover Environment*, 2(138), 2024.

[33] F. Miyake, K. Nagaya, K. Masuda, and T. Nakamura. A signature of cosmic-ray increase in ad 774–775 from tree rings in Japan. *Nature*, 486, 2012.

[34] F. Miyake, K. Masuda, and T. Nakamura. Another rapid event in the carbon-14 content of tree rings. *Nat. Commun.*, 4(1748), 2013.

[35] V.A. Dergachev and S.S. Vasiliev. Long-term changes in the concentration of radiocarbon and the nature of the Hallstatt cycle. *Journal of Atmospheric and Solar-Terrestrial Physics*, 182:10–24, 2019.

[36] Hans E. Suess. Radiocarbon Concentration in Modern Wood. *Science*, 122(3166):415–417, 1955.

[37] P. P. Tans, A. F. M. de Jong, and W. G. Mook. Natural atmospheric $^{14}$C variation and the suess effect. *Nature*, 280(5725):826–828, 1979.

[38] T. A. Rafter and G. J. Ferguson. Atom bomb effect. *Science*, 126:557–558, 1957.

[39] H. De Vries. Atomic bomb effect: variation of radiocarbon in plants, shells, and snails in the past 4 years. *Science*, 128:250–251, 1958.

[40] P. Ciais, C. Sabine, G. Bala, L. Bopp, V. Brovkin, and J. I. House. *Carbon and Other Biogeochemical Cycles.* Cambridge University Press, 2014.

[41] P. J. Reimer, W. E. N. Austin, E. Bard, A. Bayliss, P. G. Blackwell, C. Bronk Ramsey, M. Butzin, H. Cheng, R. Edwards F. Lawrence, and M. Friedrich et al. The IntCal20 Northern Hemisphere Radiocarbon Age Calibration Curve (0–55 cal kBP). *Radiocarbon*, 62(4):725–757, 2020.

[42] C. Bronk Ramsey, J. van der Plicht, and B. Weninger. 'Wiggle Matching' Radiocarbon Dates. *Radiocarbon*, 43(2A):381–389, 2001.

[43] K. F. Kaiser, M. Friedrich, C. Miramont, B. Kromer, M. Sgier, M. Schaub, I. Boeren, S. Remmele, S. Talamo, F. Guibal, and O. Sivan. Challenging process to make the Lateglacial tree-ring chronologies from Europe absolute – an inventory. *Quaternary Science Reviews*, 36:78–90, 2012.

[44] T. J. Heaton, M. Blaauw, P. G. Blackwell, C. Bronk Ramsey, P. J. Reimer, and E. M. Scott. The IntCal20 Approach to Radiocarbon Calibration Curve Construction: A New Methodology Using Bayesian Splines and Errors-in-Variables. *Radiocarbon*, 62(4):821—-863, 2020.

[45] K.Eriksson Stenstroem and G. Skog and E. Georgiadou and J. Genberg and A. Johansson. A guide to radiocarbon units and calculations, Lund University, Department of Physics, Division of Nuclear Physics Internal Report LUNFD6(NFFR-3111)/1-17/. 2011.

[46] L. Wacker, M. Christl, and H.-A. Synal. A new tool for AMS data reduction. *Nucl. Instrum. Methods Phys. Res. B*, 268:976–979, 2010.

[47] S. M. Fahrnia, J. R. Southona, G. M. Santosa, S. W.L. Palstrab, H. A.J. Meijerb, and X. Xu. Reassessment of the 13C/12C and 14C/12C isotopic fractionation ratio and its impact on high-precision radiocarbon dating. *Geochimica et Cosmochimica Acta*, 213:330–345, 2017.

[48] H. Craig. Isotopic standards for carbon and oxygen and correction factors for mass-spectrometric analysis of carbon dioxide. *Geochimica et Cosmochimica Acta*, 12(1):133–149, 1957.

[49] I. Friedman, J. O'NEIL, and G. Cebula. Two New Carbonate Stable-Isotope Standards. *Geostandards Newsletter*, 6(1):11–12, 1982.

[50] W. Stichler, R. Gonfiantini, and K. Rozanski. Reference and intercomparison materials for stable isotopes of light elements. *IAEA TECDOC*, 825, 1995.

[51] A. Stolz. Einrichtung und Weiterentwicklung eines $^{14}CO_2$-Systems am 6 MV TANDETRON Beschleuniger des CologneAMS. *PhD thesis, University of Cologne*, 2020.

[52] M. Zech and C. Bimüller and A. Hemp and C. Samimi and C. Broesike and C. Hörold and W. Zech. Human and climate impact on 15N natural abundance of plantsand soils in highmountain ecosystems: a short review and two examples from the Eastern Pamirs and Mt. Kilimanjaro. *Isotopes in Environmental and Health Studies*, 47(3):286–296, 2011.

[53] N. V. Grassineau. High-precision EA-IRMS analysis of S and C isotopes in geological materials. *Applied Geochemistry*, 21:756–765, 2006.

[54] R. Agnihotri, R. Kumar, M. V. S. N. Prasad, C. Sharma, S. K. Bhatia, and B. C. Arya. Experimental Setup and Standardization of a Continuous Flow Stable Isotope Mass Spectrometer for Measuring Stable Isotopes of Carbon, Nitrogen and Sulfur in Environmental Samples. *MAPAN–Journal of Metrology Society of India*, 29(3):195–205, 2014.

[55] A. Stolz, A. Dewald, S. Heinze, R. Altenkirch, G. Hackenberg, S. Herb, C. Mueller-Gatermann, M. Schiffer, G. Zitzer, A. Wotte, J. Rethemeyer, and T. J. Dunai. Improvements in the measurement of small 14CO2 samples at CologneAMS. *Nucl. Instrum. Methods Phys. Res. B*, 439:70–75, 2019.

[56] G.V. Ravi Prasad, Randy Culp, and Alexander Cherkinsky. $\delta^{13}$C correction to AMS data: Values derived from AMS vs IRMS values. *Nuclear Instruments and Methods in Physics Research Section B: Beam Interactions with Materials and Atoms*, 455:244–249, 2019.

[57] J. O. Melchert, A. Stolz, A. Dewald, M. Gierga, P. Wischhöfer, and J. Rethemeyer. Exploring sample size limits of AMS gas Ion Source 14$C$ analysis at CologneAMS. *Radiocarbon*, 00(00):1–9, 2019.

[58] L. Wacker, S. M. Fahrni, I. Hajdas, M. Molnar, H. A. Synal, S. Szidat, and Y. L. Zhang. A versatile gas interface for routine radiocarbon analysis with a gas ion source. *Nucl. Instrum. Methods Phys. Res. B*, 249:315–319, 2013.

[59] F. Brock, T. Higham, P. Ditchfield, and C. Ramsey. Current Pretreatment Methods for AMS Radiocarbon Dating at the Oxford Radiocarbon Accelerator Unit (Orau). *Radiocarbon*, 52:103–112, 03 2010.

[60] University of Waikato. Waikato Radiocarbon Dating Laboratory AMS Processing Technical Report. 2017.

[61] L. Tassoni, B. Kromer, R. Friedrich, L. Wacker, M. Cattani, M. Friedrich, D. Paleček, E. Pelloni, K. Peng, M. E. Thomas, and et al. Safe preparation and delivery of graphite targets for $^{14}$c analysis: procedures of bravho lab at Bologna university. *Radiocarbon*, 66(5):1368—-1378, 2024.

[62] J. Liebl, P. Steier, R. Golser, W. Kutschera, K. Mair, A. Priller, I. Vonderhaid, and E. M. Wild. Carbon background and ionization yield of an AMS system during 14C measurements of microgram-size graphite samples. *Nuclear Instruments and Methods in Physics Research Section B: Beam Interactions with Materials and Atoms*, 294:335–339, 2013.

[63] J. Rethemeyer, A. Dewald, R. Fülöp, I. Hajdas, S. Höfle, U. Patt, B. Stapper, and L. Wacker. Status report on sample preparation facilities for 14C analysis at the new CologneAMS centre. *Nucl. Instrum. Methods Phys. Res. B*, 294:168–172, 2013.

[64] Reference Sheet for Quality Control Material. 2014. `https://nucleus.iaea.org/sites/ReferenceMaterials/Shared`.

[65] C. Alderliesten and K. van der Borg and A. F. M. de Jong. Contamination and fractionation effects in ams-measured $^{14}c/^{12}c$ and $^{13}c/^{12}c$ ratios of small samples. *Radiocarbon*, 40(1):215–221, 1997.

[66] W.E. Kieser, R.P. Beukens, L.R. Kilius, A.E. Litherland, M.J. Nadeau, and J.C. Rucklidge. Accelerator mass spectrometry at Toronto. *Nuclear Instruments and Methods in Physics Research Section B: Beam Interactions with Materials and Atoms*, 24-25:667–671, 1987.

[67] X. Xu, S. E. Trumbore, S. Zheng, J. Southon, K. E. McDuffee, M. Luttgen, and J. C. Liu. Modifying a sealed tube zinc reduction method for preparation of AMS graphite targets: Reducing background and attaining high precision. *Nuclear Instruments and Methods in Physics Research Section B: Beam Interactions with Materials and Atoms*, 259(1):320–329, 2007.

[68] Q. Hua, G. E. Jacobsen, U. Zoppi, E. M. Lawson, A. A. Williams, A. M. Smith, and M. J. McGann. Progress in Radiocarbon Target Preparation at the Antares AMS Centre. *Radiocarbon*, 43(2A):275—-282, 2001.

[69] H. Hofmann, G. Bonani, E. Morenzoni, M. Nessi, M. Suter, and W. Wölfli. Charge state distributions and resulting isotopic fractionation effects of carbon and chlorine in the 1–7 MeV energy range. *Nuclear Instruments and Methods in Physics Research Section B: Beam Interactions with Materials and Atoms*, 5(2):254–258, 1984.

[70] S. Fowler, R. Roush, and J. Wise. Concepts of Biology. In *Handbook of Radioactivity Analysis (Fourth Edition)*. OpenStax, 2013. https://openstax.org/books/concepts-biology/pages/1-introduction.

[71] J. C. Barescut, J. C. Gariel, J. M. Péres, and C. Tamponnet. Modelling Tritium and Carbon 14 in the Environment: A Biomass-Oriented Approach. *Radioprotection*, 40(S1):S713–S719, 2005.

[72] K. Keskitalo, T. Tesi, L. Bröder, A. Andersson, C. Pearce, M. Sköld, I. P. Semiletov, O. V. Dudarev, and Ö. Gustafsson. Sources and characteristics of terrestrial carbon in Holocene-scale sediments of the East Siberian Sea. *Clim. Past*, 13:1213—1226, 2017.

[73] M. J. Kohn. Carbon isotope compositions of terrestrial C3 plants as indicators of (paleo)ecology and (paleo)climate. *Proceedings of the National Academy of Sciences*, 107(46):19691–19695, 2010.

[74] C. Mcintyre, L. Wacker, N. Haghipour, T. Blattmann, S. Fahrni, M. Usman, T. Eglinton, and H. A. Synal. Online 13C and 14C Gas Measurements by EA-IRMS–AMS at ETH Zürich. *Radiocarbon*, 59:1–11, 10 2016.

[75] K. Hippe, F. Kober, L. Wacker, S.M. Fahrni, S. Ivy-Ochs, N. Akçar, C. Schlüchter, and R. Wieler. An update on in situ cosmogenic 14C analysis at ETH Zürich. *Nuclear Instruments and Methods in Physics Research Section B: Beam Interactions with Materials and Atoms*, 294:81–86, 2013.

[76] M.-J Nadeau, A.E Litherland, A Rieck, and P.M Grootes. Isotopic fractionation in recombinator based 14C AMS measurements: how can we live with it? *Nuclear Instruments and Methods in Physics Research Section B: Beam Interactions with Materials and Atoms*, 223-224:346–352, 2004.

[77] H.J. Hofmann, G. Bonani, M. Suter, and W. Wölfli. Charge state distributions and isotopic fractionation. *Nuclear Instruments and Methods in Physics Research Section B: Beam Interactions with Materials and Atoms*, 29(1):100–104, 1987.

[78] R. Burleigh, K. Matthews, and M. Leese. Consensus $\delta^{13}$c values. *Radiocarbon*, 26(1):46–53, 1984.

[79] N. R. Lobanov, T. Tunningley, P. Linardakis, and E. G. Vvedenskaia. Insights into the effect of hollow cathode with external injection of fast ions in a sputter-type negative ion source. *Nucl. Instrum. Methods Phys. Res. A*, 1048, 2023.

[80] Penn State Department of Statistics. Stat 462: Poisson regression, 2026. Online statistics notes, accessed 2026-04-13.

[81] U. M. Hanke, L. Wacker, N. Haghipour, M. W. I. Schmidt, T. I. Eglinton, and C. P. McIntyre. Comprehensive radiocarbon analysis of benzene polycarboxylic acids (BPCAs) derived from pyrogenic carbon in environmental samples. *Radiocarbon*, 59:1103–1116, 2017.

[82] Haghipour N., Ausin B., Usman MO., Ishikawa N., Wacker L., Welte C., Ueda K., and Eglinton TI. Compound-specific radiocarbon analysis by elemental analyzer-accelerator mass spectrometry:Precision and limitations. *Anal. Chem.*, 91:2024–2049, 2019.

[83] M. Wertnik, L. Wacker, S. M. Bernasconi, N. Haghipour, T. I. Eglinton, and C. Welte. A universal gas interface for simultaneous $^{14}$C and $\delta^{13}$C measurements. *Radiocarbon*, 66(5):1406–2426, 2024.

[84] H. A. J. Meijer, M. H. Pertuisot, and J. van der Plicht. High-accuracy 14c measurements for atmospheric co2 samples by AMS. *Radiocarbon*, 48(3):355–372, 2006.

[85] M.G.L. Baillie. *Tree-ring Dating and Archaeology.* Routledge, 1982.

[86] D. McCarroll and N. J. Loader. Stable isotopes in tree rings. *Quaternary Science Reviews*, 23(7):771–801, 2004. Isotopes in Quaternary Paleoenvironmental reconstruction.

[87] T. Westphal and K.-U. Heussner. *Kleiner Leitfaden für den Umgang mit Holz für dendrochronologische Altersbestimmungen.* Verlag Dr. Friedrich Pfeil, ISBN 978-3-899-37-212-0, 2016.

[88] K. Haneca, K. Cufar, and H. Beeckman. Oaks, tree-rings and wooden cultural heritage: A review of the main characteristics and applications of oak dendrochronology in Europe. *Journal of Archaeological Science*, pages 1–11, 2009.

[89] K. Haneca, K. Cufar, and H. Beeckman. Oaks, tree-rings and wooden cultural heritage: a review of the main characteristics and applications of oak dendrochronology in Europe. *Journal of Archaeological Science*, 36:1–11, 2009.

[90] *Reading the Soil Archives.* Candice Janco, ISBN 978-0-444-64108-3, 2019.

[91] S. Veski, L. Amon, A. Heinsalu, T. Reitalu, L. Saarse, N. Stivrins, and J. Vassiljev. Lateglacial vegetation dynamics in the eastern Baltic region between 14,500 and 11,400calyrBP: A complete record since the Bølling (GI-1e) to the Holocene. *Quaternary Science Reviews*, 40:39–53, 2012.

[92] F. Reinig, D. Nievergelt, J. Esper, M. Friedrich, G. Helle, L. Hellmann, B. Kromer, S. Morganti, M. Pauly, A. Sookdeo, W. Tegel, K. Treydte, A. Verstege, L. Wacker, and U. Büntgen. New tree-ring evidence for the Late Glacial period from the northern pre-Alps in eastern Switzerland. *Quaternary Science Reviews*, 186:215–224, 2018.

[93] M. Friedrich, M. Knipping, P. von der Kroft, A. Renno, O. Ullrich, and J. Vollbrecht. Ein Wald am Ende der letzten Eiszeit. Untersuchungen zur Besiedelungs-, Landschaftsund Vegetationsentwicklung an einem verlandeten See im Tagebau Reichwalde, Niederschlesischer Oberlausitzkreis. *Arbeits- und Forschungsberichte zur sächsischen Bodendenkmalpflege*, 43:21–49, 2001.

[94] S. Gai, T. Lodemann, and T. Westphal. Eiszeitliche Kiefern in Paderborn-Schloss Neuhaus. *Archäologie in Westfalen-Lippe 2022*, pages 41–43, 2023.

[95] M. W. Dee, S. W. L. Palstra, A. Th. Aerts-Bijma, M. O. Bleeker, S. de Bruijn, F. Ghebru, H. G. Jansen, M. Kuitems, D. Paul, R. R. Richie, J. J. Spriensma, A. Scifo, D. van Zonneveld, B. M. A. A. Verstappen-Dumoulin, P. Wietzes-Land, and H. A. J. Meijer. Radiocarbon Dating at Groningen: New and Updated Chemical Pretreatment Procedures. *Radiocarbon*, 62(1):63–74, 2020.

[96] M. Krąpiec, E. Szychowska-Krąpiec, J. Barniak, T. Goslar, P. Kittel, D. J. Michczyńska, A. Michczyński, N. Piotrowska, A. Rakowski, and D. Wiktorowski. A Tree-Ring chronology from Allerød–YD transition from Koźmin (Central Poland). *Geochronometria*, 47(1):101–111, 2020.

[97] International Atomic Energy Agency. Progress in radioactive graphite waste management. Technical report, IAEA, Vienna, 2010.

[98] M. Dewald, M. Gwozdz, R. Margreiter, E. Strub, T. Braunroth, B. A. Dittmann-Schnabel, and R. Spanier. Charakterisierung und Quantifizierung von $^{14}$C in Reaktorgrafit mittels Beschleuniger-Massenspektrometrie. *GRS–709*, 2023.

[99] Michael F. L'Annunziata, Alex Tarancón, Héctor Bagán, and José F. García. Chapter 6 - Liquid scintillation analysis: principles and practice. In M. F. L'Annunziata, editor, *Handbook of Radioactivity Analysis (Fourth Edition)*, pages 575–801. Academic Press, fourth edition edition, 2020.

[100] Å. Magnusson. 14C Produced by Nuclear Power Reactors–Generation and Characterization of Gaseous, Liquid and Solid Waste. *PhD thesis, Lund University*, 2007.

[101] A. C.Kadak. A future for nuclear energy: pebble bed reactors. *International Journal of Critical Infrastructures*, 1(4):330–345, 2005.

[102] P. A. Demkowicza, B. Liub, and J. D. Hunn. Coatedparticlefuel:Historicalperspectivesandcurrentprogress. *Journal of Nuclear Materials*, 515:434–450, 2019.

[103] International Atomic Energy Agency. Advances in high temperature gas cooled reactor fuel technology. IAEA-TECDOC 1674, International Atomic Energy Agency, Vienna, 2012.

[104] R. V. A. Marques, C.E. Velasquez, and C. Pereira. Doppler Effect Analysis of a Fast Neutron Reactor for a Fusion-Fission System. *First International Nuclear Atlantic Conference*, 2021.

[105] M. Gwozdz and R. Margreiter and T.-F. Pabst and G. Hackenberg and K. Eberhardt and S. Heinze and S. Herb and M. Schiffer and A. Stolz and E. Strub and D. Mücher and A. Dewald. $^{14}$C AMS measurement of gas diluted reactor graphite using a Gas Injection System. *Nuclear Instruments and Methods in Physics Research B*, 533:76–80, 2022.

[106] D. Vulpius, K. Baginski, B. Kraus, and B. Thomauske. Thermal treatment of neutron-irradiated nuclear graphite. *Nuclear Engineering and Design*, 265:294–309, 2020.

[107] X. Hou. Rapid analysis of $^{14}$C and $^{3}$H in graphite and concrete for decommissioning of nuclear reactor. *Applied Radiation and Isotopes*, 62(6):871–882, 2005.

[108] German radiation protection ordinance (Strahlenschutzverordnung from 29.11.2018, BGBl. I S. 2034, 2036), amended by article 1 of the regulation from 27.03.2020 (BGBl. I S. 748).

[109] M. Enachescu, C. Stan-Sion, A. Razvan Petre, C. Postolache, and V. Fugarua. $^{3}$H and $^{14}$C measurements in the irradiated graphite from the decommissioned VVR-S reactor in NIPNE Bucharest. *J. Anal. Atomic Spectrom.*, 33(3):431–436, 2018.

[110] D. Hampe, B. Gleisberg, S. Akhmadaliev, G. Rugel, and S. Merchel. Determination of $^{41}$Ca with LSC and AMS: method development, modifications and applications. *J. Radioanal. Nucl. Chem.*, 296(2):617–624, 2013.

[111] M. Schiffer, O. Machhart, A. Priller, S. Herb, G. Hackenberg, S. Heinze, M. Martschini, E. Strub, T. Dunai, R. Golser, and A. Dewald. An advanced radio-frequency quadrupole ion cooler for accelerator mass spectrometry. *Nuclear Instruments and Methods in Physics Research Section B: Beam Interactions with Materials and Atoms*, 528:27–33, 2022.

[112] M.G. Klein, A. Dewald, A. Gottdang, S. Heinze, and D.J.W. Mous. A new HVE 6 MV AMS system at the University of Cologne. *Nucl. Instrum. Methods Phys. Res. B*, 269(24):3167–3170, 2011.

[113] V. Remeikis, E. Lagzdina, A. Garbaras, A. Gudelis, J. Garankin, J. Rita R. Plukien, L. Juodis, G. Duškesas, D. Lingis, and V. Abdulajev. Rapid analysis method for the determination of $^{14}$C specific activity in irradiated graphite. *PLoS ONE*, 13(1), 2018.

[114] R. Wood, F. King, R. Esmay, Q. Chen, L. Schneider, E. Dotte-Sarout, S. Fallon, K. Fryirs, R. Gillespie, and R. Blong. The Size Inherited Age Effect on Radiocarbon Dates of Alluvial Deposits: Redating Charcoal Fragments in a Sand-Bed Stream, Macdonald River, NSW, Australia. *Radiocarbon*, 66(5):1006–1019, 2024.

[115] D. Filipović, J. Meadows, M. Dal Corso, W. Kirleis, A. Alsleben, Ö. Akeret, F. Bittmann, G. Bosi, B.-E. Ciută, D. Dreslerová, H. Effenberger, F. Gyulai, A. G. Heiss, M. Hellmund, S. Jahns, T. Jakobitsch, M. Kapcia, S. Klooß, M. Kohler-Schneider, H. Kroll, P. Makarowicz, E. Marinova, T. Märkle, A. Medović, A. M. Mercuri, A. Mueller-Bieniek, R. Nisbet, G. Pashkevych, R. Perego, P. Pokorný, Ł. Pospieszny, M. Przybyła, K. Reed, J. Rennwanz, H.-P. Stika, A. Stobbe, T. Tolar, K. Wasylikowa, J. Wiethold, and T. Zerl. New ams $^{14}$C dates track the arrival and spread of broomcorn millet cultivation and agricultural change in prehistoric europe. *Scientific Reports*, 10(1):13698, 2020.

[116] D. Teetaert, M. Boudin, S. Saverwyns, and P. Crombé. Food and Soot: Organic Residues On Outer Pottery Surfaces. *Radiocarbon*, 59(5):1609–1621, 2017.

# Danksagung

Ich möchte mich bedanken...

... bei Prof. Dr. Dennis Mücher für seine jahrelange Unterstützung, die vielen guten Ideen und seine motivierende Begleitung, insbesondere in den Phasen, in denen Experimente und Geräte nicht wie geplant funktionierten.

... bei Prof. Dr. Andreas Maier für das Lesen und Bewerten meiner Arbeit.

... bei Prof. Dr. Tibor Dunai für den Vorsitz meiner Prüfungskommission.

... bei der Arbeitsgruppe, insbesondere Derin, Markus, Stefan, Timm und Tom. Ihr wart jederzeit ansprechbar für fachliche wie auch private Fragen und habt mit eurer Unterstützung wesentlich dazu beigetragen, dass ich auch die schwierigeren Phasen dieser Arbeit besser bewältigen konnte. Die gemeinsame Zeit im Büro und die langen Schichten am Beschleuniger werden mir immer in Erinnerung bleiben.

... bei den Bachelor- und Masterstudierenden Tom, Nora und Raphael, die ich betreuen durfte und von denen ich zugleich viel gelernt habe.

... bei den Operateuren und bei Stefan Thiel, die sich bei allen Fragen, von Elektronik bis zu Werkstattarbeiten, immer viel Zeit genommen haben.

... bei Prof. Dr. Janet Rethemeyer, PD Dr. Erik Strub und Thorsten Westphal für die vielfältige Unterstützung in den einzelnen Projekten.

... bei den Frauen in meiner Familie und darüber hinaus, die Wege eröffnet, Grenzen verschoben und Möglichkeiten geschaffen haben. Die auf Bildung oder berufliche Chancen verzichten mussten oder sich gegen Hürden behauptet haben, die nichts mit ihrer Leistung zu tun hatten. Dass ich heute meinen Weg unter anderen Bedingungen gehen darf, verdanke ich auch eurer Stärke und eurer Ausdauer. *Lock up your libraries if you like; but there is no gate, no lock, no bolt, that you can set upon the freedom of my mind.* **Virginia Woolf**

... bei meinen Freunden: Annika, Caro, Ines, Jörg, Lasse, Luca, Marie B., Marie Z., Max, Nico, Pau und Paulina. Ihr wart immer da — zum Zuhören, zum Ablenken, zum Mitfreuen oder einfach, um mich daran zu erinnern, was wirklich wichtig ist. Bei euch konnte ich mich über alles und jeden aufregen, euch jederzeit schreiben, und ich wusste immer, dass ich nicht allein bin. Eure Unterstützung, eure Geduld

und eure Freundschaft haben diese Zeit nicht nur erträglicher, sondern auch schöner gemacht.

... bei Kati und Elle für eure Freundschaft seit über 20 Jahren. Ohne euch wäre ich nicht die Frau, die ich heute sein darf. Wenn mich jemand auffängt, dann ihr. Eure Liebe und eure Unterstützung in wirklich allen Bereichen des Lebens zeigen mir immer wieder, wie gut die Welt sein kann.

... bei meinen Eltern, meinem Bruder, meinen Großeltern, meinem Onkel und meinem Patenkind Lena für eure Unterstützung, euren Rückhalt und die Werte, die ihr mir mitgegeben habt und die mich auf meinem Weg immer begleitet und geprägt haben.

... bei meinem Partner Chris Heinen, der mich über fast die gesamte Zeit meiner Dissertation begleitet und angefeuert hat. Danke für die vielen gemeinsamen Erlebnisse, die unzähligen Gespräche, die *very well traveled* Reisen, für die Selbstverständlichkeit, mit der du mir Raum gegeben hast, mich so zu entfalten, wie ich es brauchte, für die vielen Anrufe während meinen Reisen zu Konferenzen und für deine Unterstützung in all den Phasen, in denen diese Arbeit besonders viel Raum eingenommen hat. Dass du in diesen Zeiten so vieles mitgetragen und aufrechterhalten hast (vor allem mich) bedeutet mir sehr viel.